Ministry of Higher Education and Scientific Research

Monastir University

THESIS

Presented to fulfill the Doctor Degree requirements from the

National Engineering School of Monastir

In **Energy Engineering**

By **Sahar SLIMENE**

Numerical investigation of a standing-wave thermoacoustic engine

Publicly defended on June 25, 2022

Jury Members

Mr. Abdallah MHIMID	Professor	ENIM, Monastir	Chair
Mr. Walid HASSEN	Associate-Professor	ENIM, Monastir	Reviewer
Mr. Mohamed Hichem GAZZAH	Associate-Professor	FSM, Monastir	Reviewer
Mr. Hassane NAJI	Professor	UNIV. ARTOIS, France	Examiner
Mr. Hacen DHAHRI	Professor	ENIM, Monastir	Thesis supervisor

Laboratory of Thermal and Energy studies (LESTE)-ENIM, MONASTIR

Acknowledgement

*Researches provided in this thesis was carried out the Laboratory of Thermal and Energy Systems Studies **(LESTE)** at the National Engineering School of Monastir **(ENIM).***

First and foremost, I would like to express my gratitude to my supervisor ***Dr Dhahri Hacen*** *professor and head of energy department at the National Engineering School of Monastir for imparting his knowledge and expertise. His guidance helped me in all the time of research and writing of this thesis.*

I would like to express my deepest gratitude and thanks to ***Dr Naji Hassan*** *professor at the University of Artois for his successful co-operation, valuable help, understanding and encouragement which were the sustaining factors to compete my thesis study.*

Besides my advisor, I would like to thank the rest of my thesis committee:

My sincere thanks goes to ***Dr Mhimid Abdallah,*** *professor at ENIM, for accepting to be the president of the committee and evaluating my thesis work.*

I thank profusely my committee members ***Dr Hassen Walid*** *Associate-Professor at ENIM and* ***Dr Gazzeh Mohamed Hichem*** *Associate-Professor at the faculty of sciences of Monastir for agreeing to read the thesis report. Their valuable reviews helped to improve the quality of my work.*

I offer my special thanks to all of my family members for their positive encouragement and for providing warm spirit to finish this thesis. It would not be possible to write this thesis without the support from them. I would like to thank my dearest father ***Mohamed Slimene****, my mother* ***Habiba****, my sisters and brothers and my nephews and nieces.*

Furthermore, I would also like to thank all my beloved friends who were with me and support me through thick and thin.

May God shower the above cited personalities with success and honor in their life.

Table of Contents

List of Tables

List of Figures

Nomenclature

List of symbols

Be	Bejan number
c	Lattices speed (ms^{-1})
c_s	Sound speed (ms^{-1})
c_i	Lattice velocity in direction i
C_p	Specific heat capacity at constant pressure $(J.Kg^{-1}.K^{-1})$
Da	Darcy number $(= K/\varepsilon H^2)$
d_p	Mean pore diameter (m)
$\bar{\bar{d}}, \bar{\bar{D}}$	Strain-rate tensors
E_c	Eckert number $(= U_{ref}^2/C_f \Delta T_{ref})$
f_i, g_i	Distribution functions in direction i
f_i^{eq}, g_i^{eq}	Equilibrium distribution functions
F_ε	Forchheimer form coefficient
F	Total body force by unit mass $(N.kg^{-1})$
g	Gravity acceleration $(m.s^{-1})$
G	Buoyancy force
H, L	Characteristic height and length (m)
K	Porous medium permeability (m^2)
k	Thermal conductivity $(W.m^{-1})K^{-1})$
Ns	Entropy generation
Nu	Local Nusselt number
Nu_{av}	Average Nusselt number
P	Pressure (Pa)
p	Dimensionless pressure
Pr	Prandtl number $(= \mu C_{p,f}/k_f)$
r	Reflection coefficient
Ra	Rayleigh number$(= g\beta(T_H - T_C)H^3/\nu\alpha)$
Rc, Rk	Ratios of heat capacities and thermal conductivities
Re	Reynolds number $(= U_{Ref}H/\nu)$
$t, \tilde{t}$	Real time and CPU time

T	Temperature (K)
$\tilde{U}(U,V)$	Velocity $(m.s^{-1})$
$\tilde{u}(u,v)$	Dimensionless velocity
X,Y	Cartesian coordinates (m)
x,y	Dimensionless coordinates
Q,W	Heat power (W), acoustic power (W)

Greek symbols

α	Thermal diffusivity
β	Thermal expansion coefficient (K^{-1})
ε	Porosity
η	Thermal efficiency $(\%)$
μ	Dynamic viscosity $Pa.s$
ν	Kinematic viscosity $(m^2.s^{-1})$
Φ	Viscous dissipation
ϕ	Dimensionless viscous dissipation
ϑ	binary number
ψ	Acoustic wave's phase
ρ	Density
τ	Dimensionless relaxation time
$\bar{\bar{\tau}}$	Newtonian shear stress tensor
θ	Dimensionless temperature

Mathematical operators

$\nabla()$	Gradient operator
$\nabla.()$	Divergence operator
$\nabla^2()$	Laplacian operator
$\Delta()$	Difference operator

Superscripts/subscripts

H, C, a	Hot, cold and ambient
f, s, e	Fluid, solid, effective
I	Initial state
PM	Porous medium
Ref	Reference
w	wall

Acronyms

BCs	Boundary conditions
BGK	Bhatnagar-Gross-Krook
BFD	Brinkman-Forchheimer-Darcy
CFD	Computational fluid dynamics
LBE	Lattice Boltzmann equation
LBM	Lattice Boltzmann method
LTE	Local thermal equilibrium
SRT	Single relaxation time
$SWTAE$	Standing-wave thermoacoustic engine
$TWTAE$	Traveling-wave thermoacoustic engine

Introduction

During the past 20 years, the global demand of energy accelerates faster by about 41% than the world population progression which count 27% between 2000 and 2020 (Figure 1). In fact, most of energy demand was for economic and industrial activities [1].

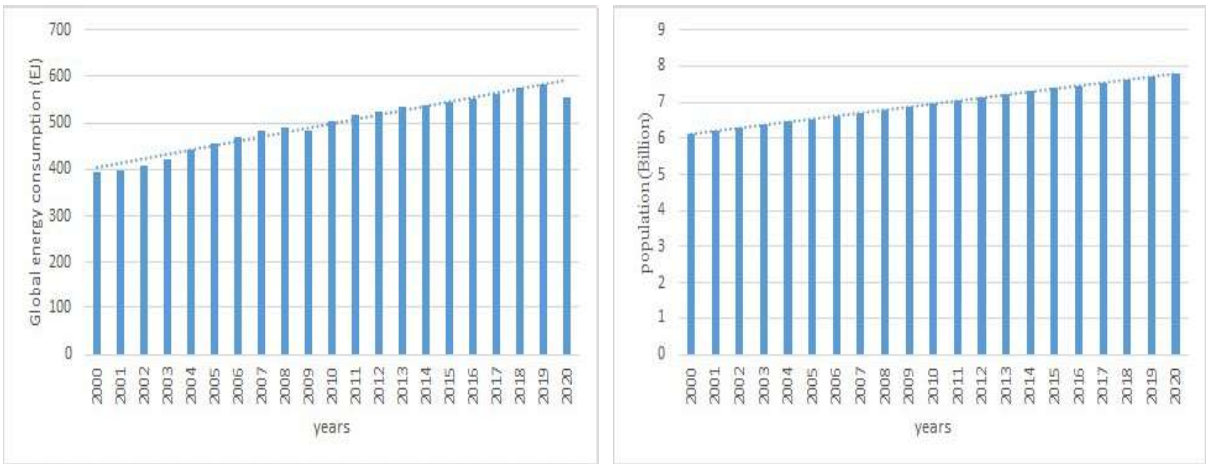

(a) (b)

Figure 1: Evolution of (a) the global energy consumption [2] and (b) world population [3] between 2000 and 2020

In 2020, more than 80% of the global energy consumption was derived from fossil fuel such as coal, crude oil, and natural gas [4]. In effect, actual economic and environment defiance are appeared as a result of the continued dependency on fossil energy as primary source of power. Besides, it can be observed that through the last 10 years (Figure 2), the investment in renewable sources increases gradually. Alternatively, many efforts are carried towards the energy harvesting of industrial and domestic waste such as heat waste recovery.

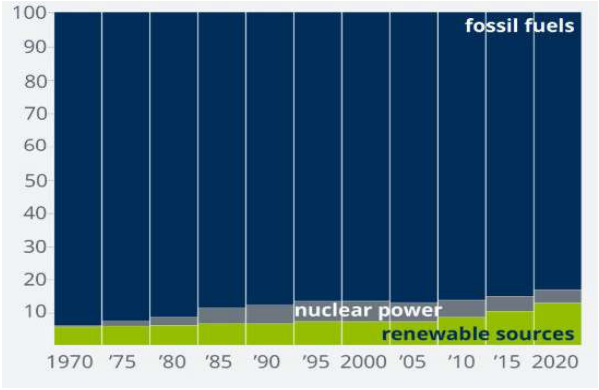

Figure 2: Global energy consumption by source of energy between 1970 and 2020 [4]

The implementation of a heat recovery mechanism leads to significant gain in fossil fuel consumption and cost. In 2016, 2.8% of the primary energy consumption comes from the recovery of low-grade industrial waste heat ($T < 100$ °C). The recovery of discharged low-grade heat is feebly viable by the useful technologies. Fortunately, further to the effectiveness of thermal to acoustic conversion at weak temperature gradient at lower than 10 °C [5], thermoacoustic technology is considered as a serious competitive technique in low-grade heat waste recovery. Appropriately, the increasing interest in thermoacoustic technology is due to the outstanding features which make them very reliable for several sorts of energy production such electric generation and heat pumping.

Furthermore, the thermoacoustic technology has a potential interest in green energy manufacturing and industrial waste recovery. Moreover, serious consideration has been offered to thermoacoustic engine development further to the economical and ecological solution given in the regeneration of industrial heat waste. Such recover technology is technically for electricity generation. However, thermoacoustic technology worth to be considered as a the key merit for low-grade heat recovery. Exploiting friendly gases and non toxic materials with the low cost construction make those sort of devices very accurate in the industrial heat waste recovery.

The aim of this thesis is to numerically optimize the efficiency of a standing wave thermoacoustic engine by minimizing the undesirable nonlinear instabilities. Allowing the variation of the emerging parameters, the thermal lattice Boltzmann model (TLBM) is actually elaborated to find the performed structure and constructive material of the core of the thermoacoustic device. This thesis attempts to follow the next structure:

Chapter 1 Thermoacoustics: A general overview about the thermoacoustic technology is given in this chapter. At first, a brief history about the critical evolution of the thermoacoustic field is presented. In the second part, general aspect of thermoacoustic theory and applications are expected. Then, the conversion principle within the different types of thermoacoustic devices is revealed. The last part presents a bibliographical synthesis about the general structure and main particularities of standing wave thermoacoustic devices.

Chapter 2 lattice Boltzmann method: The numerical model used for the simulation of the fluid flow and heat transfer within a standing wave thermoacoustic engine is presented in

this chapter. The kinetic theory of the fluid dynamic is depicted for the discretization of the lattice Boltzmann method. Then, details of the discretized model within the different parts of the thermoacoustic engine is described. Particularly, the extended lattice Boltzmann model for the simulation of complex area as the thermoacoustic porous core is detailed. Standing wave thermoacoustic engine boundary condition at the external walls and core limits are therefore clearly developed.

Chapter 3 Optimization of a standing wave thermoacoustic engine performance by entropy generation minimization using lattice Boltzmann method: This part focus on the investigation of heat transfer and entropy generation within a simple standing-wave thermoacoustic engine using thermal lattice Boltzmann method (TLBM). Based on Darcy–Brinkmann–Forchheimer model, the heat transfer and dynamic fields within the thermoacoustic device are examined. The influence of the various thermo-physical factors which serves on the selection of the ideal material and leads to an optimum engine work with minimum entropy generation are therefore tested. It is found that great acoustic and thermal losses are provided at the TAC limits due to the existence of non-linear thermo-viscous interaction between the working gas particles and the pores surfaces.

Chapter 4 Simulating Rayleigh streaming and heat transfer in a standing wave thermoacoustic engine via a thermal lattice Boltzmann method: In this chapter, the streaming flow and convective heat transfer in a standing wave thermoacoustic engine (SWTAE) filled with helium gas were numerically handled. The mathematical model depicting the flow and heat transfer occurring consists of the extended Brinkman-Forchheimer Darcy equations under Boussinesq approximation. The numerical resolution was performed using a thermal lattice Boltzmann method (TLBM) based on the approximation of Bhatnagar-Gross-Krook (BGK). The effect of thermal gradient between the thermoacoustic core boundaries on the acoustic excitation and on Rayleigh streaming has been well inspected. It turned out that the convection effect on the acoustic velocity is mainly observed on the engine core hot side while it is negligible on the cold side. Moreover, it can be detected that the Rayleigh streaming is particularly detected at low thermal gradient and that the minimization Rayleigh effect improves the thermoacoustic conversion at large thermal gradient.

[1] Alarenan, Shahad, Anwar A. Gasim, and Lester C. Hunt. ”Modelling industrial energy demand in Saudi Arabia.” Energy Economics 85 (2020): 104554.

[2] url: www.statista.com/statistics/280704/world-power-consumption/

[3] url: www.worldometers.info/world-population/world-population-by-year/

[4] url: www.dw.com/en/net-zero-by-2050-9-charts-showing-the-worlds-progress/a-59684637

[5] Van Sciver, Steven W., K. D. Timmerhaus, and Alan F. Clark. Helium cryogenics. Vol. 470. New York: Springer, 2012.

Chapter 1

Thermoacoustics

1.1 Introducion

Nowadays, the thermoacoustic field is still in the phase of technical and operational improvement. Most of current researches focus intensively on the application of such technology in clean energy production for the reduction of global warming emissions. This orientation comes further to the employment of environmental working gases for electricity production. Additionally, the low maintenance requirement quality make those sorts of devices very reliable and cost saving.

The first part of this chapter gives a brief history about the major reviews and thermoacoustic technology development. The second part provides an overview about the thermoacoustic theory. Then, the various thermoacoustic devices and their applications are exhibited1. Thereafter, a theoretical description of the appropriate conversion principal is introduced. The last section reveals the geometrical configuration and operating mode of a standing wave thermoacoustic engine.

1.2 Brief history

In the past three centuries, the thermoacoustic technology pursuit an intensive development in many laboratories. The thermoacoustic effect has been discovered for the first time in 1777 by Byron Higgins [1]. When heating a semi-open tube filled with hydrogen at different positions, acoustic standing waves are produced forming the so called ”singing flame”. Meanwhile, for centuries, glassblowers has observed the thermoacoustic phenomena by hearing sound when the glass bulb are blowing at the cold narrow.

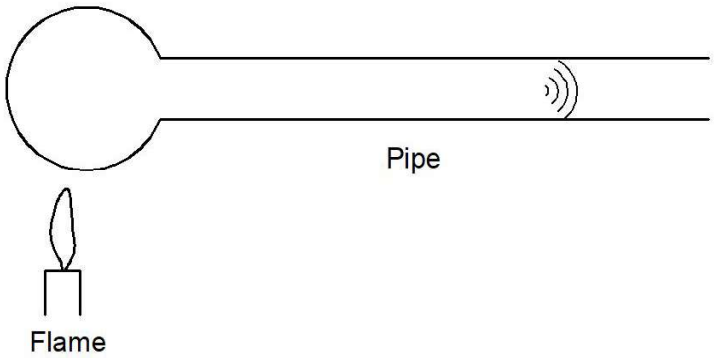

Figure 1.1: Schematic of Sondhaus’s tube

According to Feldman [2], the first description of the observed phenomena was given by Carl Sondhauss in 1850. He experimentally proved that by applying a heat gradient to a semi-closed pipe, spontaneous sound waves appears at the open end (Figure 1.1). In his investigation, Sondhauss has found great dependency between the produced standing waves frequency and the length of the tube. Later, in 1859, Rijke [3] re-experimented the Higgins configuration and replaced the hydrogen flame by a heated gauze (wire mesh) to produce stronger acoustic oscillations as seen in Figure 1.2. He pointed out that maximum acoustic oscillations are generated when placing the wire mesh at the one-fourth length distance from the lower end. Therefore, in 1869, Kirchhoff [4] gives the first quantitative analysis of the physics of thermoacoustic. He determines the equations describing the thermal attenuation of sound based on the Navier-stockes equations and the Fourier's law of thermal conduction.

Figure 1.2: Structure of Rijke tube

In 1896 , Lord Rayleigh [5] gives an explanation of the phenomenon occurred within the Sondhauss tube. The Rayleigh criteria has been announced as follow:" *If heat be given to the air at the moment of greatest condensation or taken from it at the moment of greatest rarefaction, the vibration is encouraged*". Indeed, it has been admitted that the birth of thermoacoustic oscillations is linked to the variation of density with heat. By the same token, based on the existence of temperature gradient within a semi-closed tube, Kramers [6] developed a mathematical description of the kirchhoff theory to the case of attenuation of the sound waves.
In the 1950s, advanced efforts are made within the Bell Telephone laboratories [7, 8] to produce electricity by the exploitation of thermoacoustic engines. Acoustic pressure are produced further to the existence of thermal gradient within the standing-wave engine converted therefore to electricity via an electromagnetic converter. Thereafter, Carter et al. [9] experimentally improved the Sondhauss tube by inserting a stack plates with a cold and hot exchangers at both sides. Further to the efficient heat transfer within the stack, strengther acoustic oscillations are produced.

The inverse conversion process has been subsequently discovered by Merkli et al. [10] in 1975. A piston was placed at one side of a resonator tube while the opposite side was closed. Delivering a periodic sinusoidal pressure waves, the working fluid was driven to accomplish a thermodynamic cooling cycle. Eventually, previous founding has been followed by several experimentations in the Los Alamos National Laboratory (LANL) during the 1980s. Among investigations discussed the dependence of cooling effect on the velocity dissipation and the heating nearby the velocity node region. Meanwhile, further successful attempts in LANL has been made with Swift [11] in building standing wave thermoacoustic engine in a large scale. The system was filled with a pressurized helium as working gas and achieved 9% thermal efficiency with 7 kW input heat.

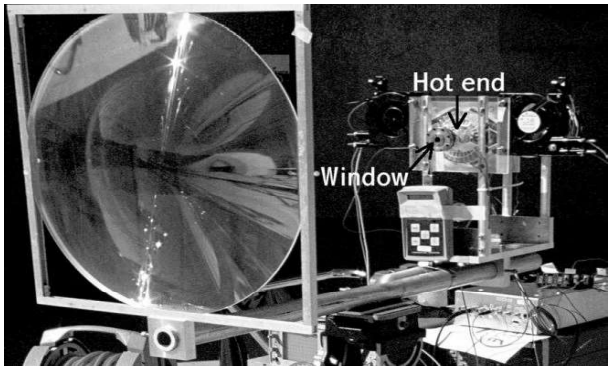

Figure 1.3: Solar powered thermoacoustically driven thermoacoustic refrigerator built by Adeff

The earliest thermoacoustic refrigerator has been built by Hofler in 1986 [12]. It consisted of a resonance tube with reduced section at the buffer tube to minimize the thermo-viscous losses. 12% coefficient of performance (COP) was achieved with 0.66 ratio of the cold temperature to the ambient temperature. The integration of renewable energies within the thermoacoustic technology, such as the solar energy, has been firstly evaluated and developed by Adeff and al. [13]. A solar powered thermoacoustic refrigerator has been build and investigated (Figure 1.3) demonstrating the merit of sch technology to be further improved.
In 1998, the first travelling wave thermoacoustic engine (TWTAE) has been designed and built by Yzaki et al [14]. Suffering from important thermal and viscous losses at the regenerator, the designed device has low conversion efficiency. Besides, the effectuated experimentation prove the better performance of travelling wave devices than the standing-wave devices at similar working conditions as the frequency and the wavelength. Later, in 1999, Backhaus and

Swift [15, 16] had built a TWTAE achieving 30% thermal efficiency (Figure 1.4). The designed system is based on traveling-wave phasing and a Stirling like thermodynamic cycle. This engine is mainly composed of a one-fourth wavelength resonator tube filled with helium as working gas. Heat exchangers are placed at a torus-shaped section with a regenerator to force the working fluid to execute the Stirling cycle. So far, that system is still considered as a model for the development of travelling wave systems.

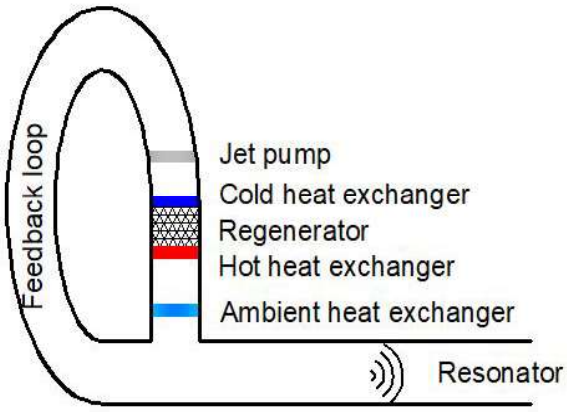

Figure 1.4: Backhaus and Swift engine

In 2004, Symko et al. [17] experimented a thermoacoustically driven thermoacoustic cooler at high-frequency driven by a thermoacoustic engine operating with heat from microelectronic components to pump heat. Further investigations has been conducted by De Block and Kees [18] who developed a multi-stage low temperature powered thermoacoustic system. The designed system utilised low thermal gradient, in the range of 70 °C- 200 °C, from solar resources or waste heat. In order to optimize the thermoacoustic system power, the viscous dissipation effect has been limited by enlarging the cross-section of the regenerator. Nowadays, the interest in thermoacoustics had extended worldwide.

1.3 Thermoacoustic theory

The thermoacoustic effect is defined as the heat transfer between a fluid and solid material in the presence of an acoustic wave. A progress towards the theoretical description of the named behavior has been mainly restricted to the linear theory. Besides, the thermoacoustic field still in the technical improvement stage where it is actually encompassed into the fields of ther-

modynamics and acoustics. A theoretical understanding of the phenomenon has been firstly developed by Rott [19] and Swift [20] along with standard prototype devices based on this technology. Further to its capability of reducing the cost effective way, it has been employed to produce electricity in a reliable way followed by their utilization in refrigeration and cryogenic cooling. The generated work from heat it therefore transmitted via a moving a piston or turning a turbine to be converted therefore to electric power via electromagnetic converter as a linear alternators, piezoelectric transducers, magnetohydrodynamic generators or a bidirectional turbines. Linear alternators are generally used in thermoacoustic engines to convert the acoustic energy and employ it for electricity production.

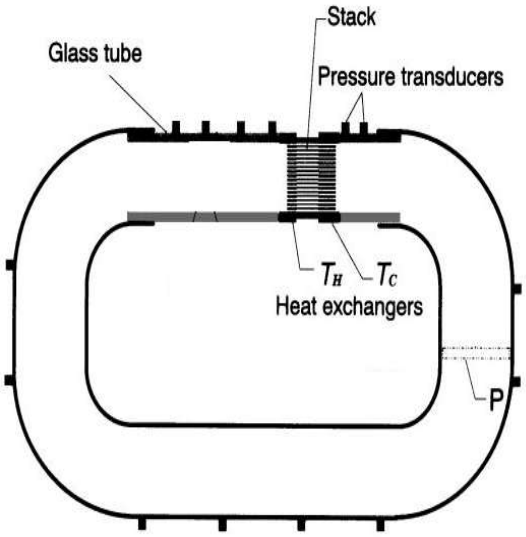

Figure 1.5: Schematic drawing of Yazaki's experimental device

At first, engines were mainly based on standing wave phasing. In effect, that type of energy converters has been fast developed and contributes to the global trend towards the use of green energies. The supplying thermal energy leads to a spontaneous production of an acoustic wave along the longitudinal direction of the temperature gradient as tell Rayleigh's criteria. Thereafter, the concept of a travelling wave thermoacoustic engine (Figure 1.5) has been practically demonstrated by Yazaki et al [14] : the first stage contain a standing wave thermoacoustic engine where the acoustic power is generated by the core. This power is therefore transferred into the neighboring travelling wave stage to amplify the generated acoustic power. The thermoacoustic core is placed at the one wavelength of the looped-tube. A quatity of the acoustic power leaves from the core hot side and therefore transported-back to the ambient side travers-

ing looped tube. A feeble efficiency is reported caused by the existence of a slight acoustic impedance within the regenerator that leads to important visco-thermal losses that reduce the amplitude of the acoustic velocity in the regenerator. In effect, the high impedance gives rise to the pressure dissipation throughout the piston of the used alternator.

The maximum thermal-to-acoustic efficiency is about 20% in thermoacoustic field which is not nearly as high as the 70% accrued achieved in other fields [21] as combustor engines. The highest thermal efficiency, being the acoustic power generated by a stack subject to a thermal gradient [22], is reported to be just 18% [23]. It can be understanding that the upper thermal efficiency can be achieve by a standing-wave engines is understood to have an upper limit of around 20% [16], due to the existence of important irreversible thermodynamic cycle.

1.4 Thermoacoustic devices applications

The conversion of thermal energy to acoustic energy and reversibly specifies the thermoacoustic field as a potential technology for heat engines and heat pumps refrigerators. Following the direction of the energy conversion, the thermoacoustic effect is mainly used in two principal applications: the first concerns the production and the amplification of an acoustic wave in a resonator tube by the mean of a temperature gradient between the porous core limits. The second application concerns the pumping of heat from a cold reservoir, such as heat exchanger placed at one side of the core powered by the excitation of acoustic wave into the resonator. Further to its potential in the exploitation of clean energy, thermoacoustic technology has a growing interest in industrial application.

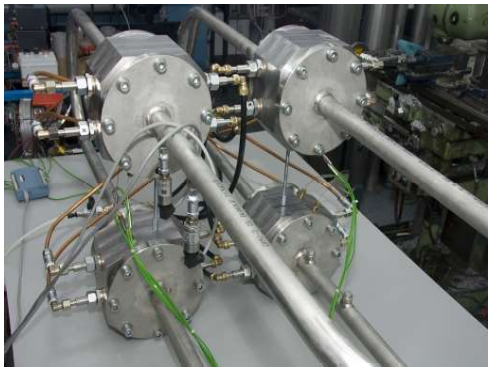

Figure 1.6: Setup of the four stage travelling wave engine built by THATEA

The first thermoacoustic project on the European level was the THATEA (THermoAcoustic Technology for Energy Applications) [24]. In 2011, Aster and Hekyom enterprises, (ECN and NRG) research institute with the partnership of the three academic groups (CNRS, UNIMAN and UNIME) has developed a thermoacoustic engine achieving 40% heat to acoustic theoretical efficiency. Meanwhile, the aster-thermoacoustics research company, leader in the development and commercialization of the thermoacoustic energy conversion, was involved within many projects. To name a few, a multistage thermoacoustic engine (Figure 1.6) has been designed and build in 2010 to operate at low input temperature. They recorded an onset temperature difference of 31 °C. Therefore, to achieve an improved thermoacoustic power at low temperature operation, a feedback circuit is connected to allow the insertion an arbitrary number of regenerators at each stage.

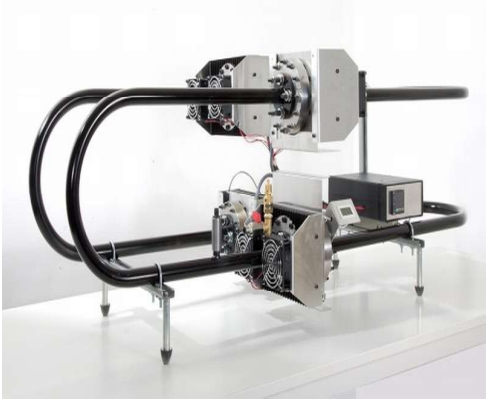

Figure 1.7: Schematic drawing of solar powered thermoacoustic cooler developed in the aster-thermoacoustics company

Later, in 2012, a solar powered thermoacoustic cooler (Figure 1.7) was built to be the first commercial application of thermoacoustic systems. A special perception were carried to that technology owing to the lack of negative effects on the environment and the linear dependence between cooling and solar power. The hot heat exchanger was maintained at 160 °C by an external cartridge heaters. The cold heat exchanger kept cool by forced convection about around 40 ℃. The developed system produced ice at -3.2 ℃ at the cold exchanger side.
In 2020, within THATEA project framework, a thermoacoustic cooler (Figure 1.8) was installed at the roof of schools and public buildings to increase safety. Using photovoltaïc solar energy the device heat exchangers are supplied by electricity which avoid the use of hot fluids as hot water and oil.

Figure 1.8: Installation of the roof top thermoacoustic chiller

At the Netherlands Organisation (TNO) working in the TASTE project developed an industrial thermo-acoustic heat pump (Figure 1.9) able to upgrade residual heat of 120 ºC.In February 2020, the MDO Lab in collaboration with the NASA Glenn Research Center and Jet Propulsion Laboratory developed a new hybrid electric transport aircraft technology (Figure 1.10).

Figure 1.9: Thermo-acoustic heat pump developed by the TASTE project

Further to its effectiveness and simplicity, the thermoacoustic engine is employed successfully to supplies acoustic waves to cool the diverse components of the aircraft such as batteries and electric motors. In the objective to be integrated within a full-scale powertrain, the MDO Lab scientist researchers aims to improve a thermoacoustic thermal management system and prove its effectiveness for an optimized hybrid electric aircraft.

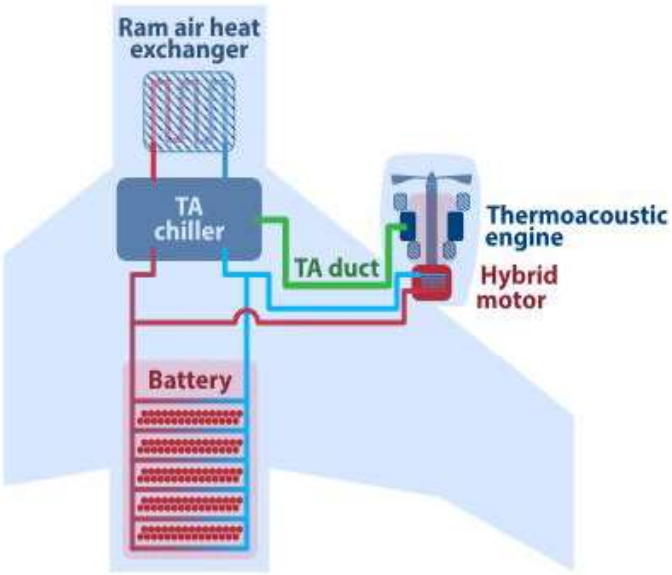

Figure 1.10: Schematic drawing of the hybrid electric commercial transport aircraft developed by the MDO Lab

1.5 Thermoacoustic devices configuration

In the past decades, significant efforts have been made to develop the configuration of the various thermoacoustic systems in order to convert thermal energy to acoustic power referring to the thermoacoustic effect. Nowadays, the named systems are gaining an evolution of research interest because of their performance in applications for heat pumping and electricity production. Compared to the conventional ones, thermoacoustic devices have many advantages further to the use of friendly environment working gases and requirement of low maintenance due to the absence of moving machinery. Those outstanding features make such system potential for high reliability, simplicity of design and low maintenance which is translated therefore into the low cost making thermoacoustic devices very competitive compared to conventional existing technologies [25].

The heat transfer between the solid surface and the gas flow provides a time delay between temperature and pressure oscillations. The reasonable thermal contact area between the working fluid parcel and the thermoacoustic core walls improves the appropriate phasing between the pressure oscillations and heat transfer. The correct phasing of oscillations between the working parcel and the solid stack surface drives the gas parcels to complete the appropriate thermodynamic cycle. Depending on the thermoacoustic device type, the adequate thermal contact should be perfectly achieved.

1.5.1 Standing wave thermoacoustic devices

Standing wave thermoacoustic devices (Figure 1.11) have the simplest configuration to build and operate. These sorts of devices are composed of a straight resonator tube filled in part with a thermoacoustic core (TAC). The core is generally made of a stacked plates or a porous medium placed between two heat exchangers. The resonator tube is of quarter wavelength acoustic oscillation. In effect, the resonator length depends on the acoustic pressure wavelength where the pressure oscillation is maximal (antinode) at the closed boundary and no pressure oscillation (node) is noticed at the open boundary. The inner core (stack) is the main element in which the thermoacoustic conversion takes place either to produce or to consume acoustic work subject to a temperature gradient. It is generally situated near the pressure antinode (closed end) and maintained under a temperature gradient by the mean of two heat exchangers at each boundary. Moreover, the velocity vibration is shifted by 90 degree from the pressure oscillation.

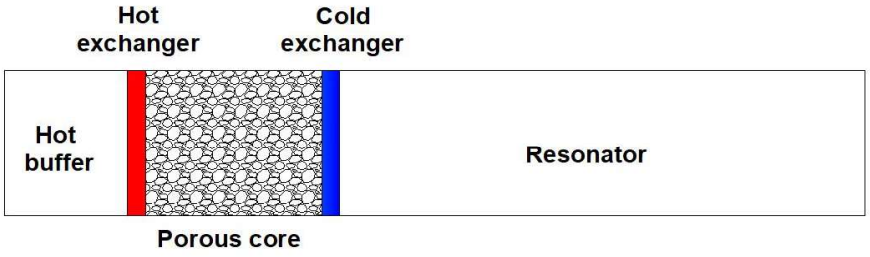

Figure 1.11: Standing wave thermoacoustic device design

1.5.2 Traveling wave thermoacoustic devices

The travelling wave devices design is more complicated then standing wave ones. It employs a looped compliance as proposed Ceperley [26] or a feedback inertance following De Blok's design [18]. Herein, the stack is replaced by a porous medium called a regenerator. Contrarily to the irreversible criterion of the standing wave devices operation, travelling wave ones underlies a reversible Stirling thermodynamic cycle and the imperfect thermal contact at the porous structure is no longer required. Such systems are designed to work with pressure and velocity oscillations in phase which allow a maximum rate of compression-expansion at the peak left or right most displacement. Such criterion eliminates the requirement of adiabatic motion of gas particles which explain the changing the operation of the stack to that of the regenerator. Accordingly, De Blok [27] designed a travelling wave thermoacoustic engine with a feedback

pipe which could start at an onset temperature difference of only 65 K. Later, a multi-stage engine of this type has been developed. It was able to operate at an onset temperature difference of just 40 K at each engine stage.

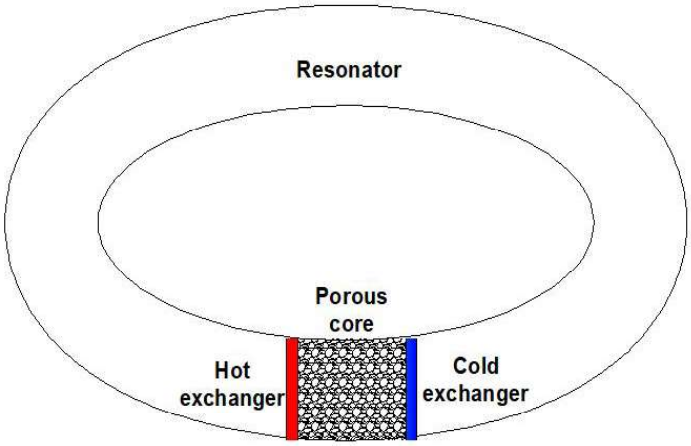

Figure 1.12: Travelling wave thermoacoustic device design

1.5.3 Thermoacoustically driven thermoacoustic cooler

The hybrid thermoacoustic system is composed of closed resonator containing two thermoacoustic cores. It consists a coupled thermoacoustic engine and thermoacoustic cooler. Two cores are placed in the same resonator tube where the first serves in the production of acoustic waves which drive the second core to produce heat pumping.

The first part of the system acts as a standing wave thermoacoustic engine. The core is placed nearby the west closed end. It is composed of a porous medium and two heat exchangers. The external walls of the system are exposed to ambient temperature while a hot and cold exchangers are positioned at the porous core extremities to provide a temperature gradient. Crossing the hot exchanger, the temperature of the working fluid is partly converted into acoustic work and spontaneously oscillates until it falls the cold exchanger.

The produced acoustic power propagates within the second part of the system. Between the cooler stack limits, the temperature of the working gas fluctuates adiabatically by the effect of pressure oscillations. The temperature is cooled as the gas particle are expanded. Then, the heat is pumped by the exchanger placed at east side of the stack.

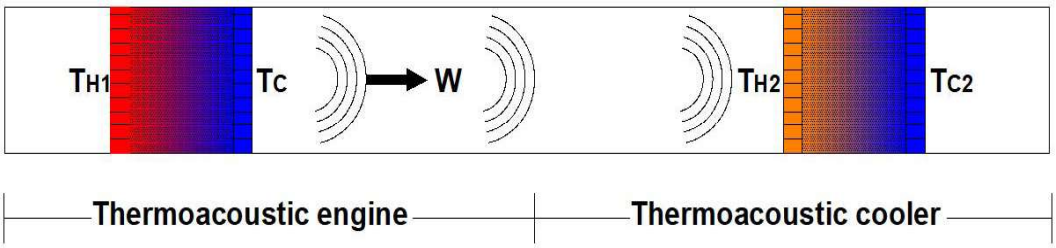

Figure 1.13: Schematic drawing of thermoacoustically driven thermoacoustic cooler

1.6 Thermoacoustic principle

The thermoacoustic effect is closely dependent on the interaction between heat transfer and fluid flow within the thermoacoustic device core. Principally, the inetrmolecular collision under temperature gradient provides spontaneous compression and expansion and cause the nascence of the thermoacoustic effect namely ”acoustic vibration” or ”heat pumping”. According to Lord Rayleigh criteria the thermoacoustic oscillations are closely linked to the thermal variation and pressure fluctuations. The conversion process occurs principally near the solid walls of the porous core which is called stack when the device generate standing waves and regenerator when travelling waves are produced.

1.6.1 Thermoacoustic engine thermodynamic cycle

The acoustic wave generation are briefly explained as a vibration caused by the compression and expansion of the heat transfer fluid. The following cycle is experienced by the working gas:

(a). In this first step, The cycle begins with the gas parcels situated near the hot exchanger absorb heat and being slightly compressed at constant temperature T_C,

(b). In the second step, the gas parcels moves toward the cold side of the stack. The adiabatic expansion of the particles encourages the vibration and generate an acoustic power W as its temperature drops from T_C to T_H,

(c). Since this part of the cycle, particles situated near the cold exchanger eject heat and expand slightly at constant temperature T_H,

(d). As the fluid parcels moves toward the hot exchanger, the temperature increases from T_C to T_H and being compressed adiabatically. The gas being at its initial state, it goes to complete an acoustic cycle,

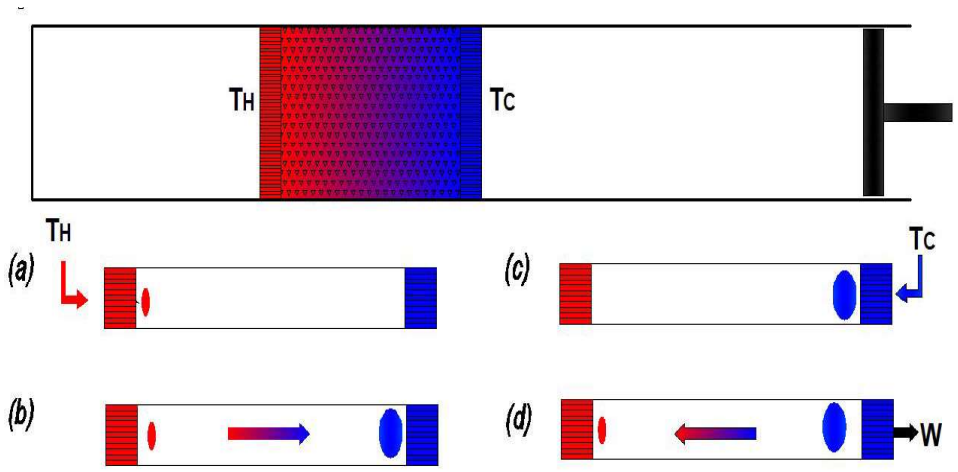

Figure 1.14: Thermodynamic cycle within the thermoacoustic engine core

1.6.2 Thermoacoustic cooler thermodynamic cycle

The working gas parcels within the cooler stack's boundaries undergo the following thermodynamic cycle:

(a). Moving towards the hot side of the stack, the working fluid particles experiences a nearly adiabatic compression. At this step of the thermodynamic cycle, the temperature increases from T_C to T_H as the time it takes for the gas to proceed and the volume slighly decreased,

(b). In the following step of cycle, the fluid particles are heated at the hot side of stack. At that level, the gas particles absorbs heat and undergo an isothermal compression,

(c). The working gas particles expands from higher pressure nearby the hot exchanger dropping as it moves toward the cold heat exchanger. The temperature of the gas parcel cools down gradually from T_H to T_C. This step is proceeding adiabatically,

(d). Reaching the cold exchanger twice, the gas particle goes one full acoustic cycle. The gas arrives at the cold heat exchanger, the working fluid reject the heat to the cold reservoir completing the cycle,

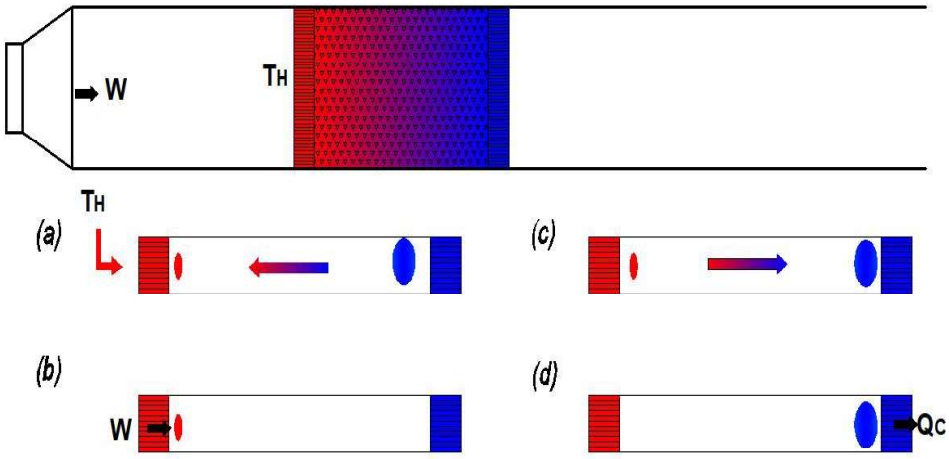

Figure 1.15: Thermodynamic cycle within the thermoacoustic cooler core

1.7 Standing wave thermoacoustic engines

Standing wave thermoacoustic devices are specified by their often simple configuration. The main components of a thermoacoustic device are a straight tube called resonator and a thermoacoustic core (TAC). The TAC is principally composed of a porous medium or a stack plate placed between a hot exchanger and cold exchanger respectively at the west and east sides. The produced acoustic waves are remained fixed in space. The amplitude of the acoustic oscillation at every position of the engine does not change with time. More precisely, the acoustic pressure of each particle is noticed to have varied values with the time, but at every position, the maximum remains constant.

1.7.1 Resonator

The resonator tube is the equipment chargeable with the working fluid and contain the stack, the hot and the cold heat exchangers. The length of the resonator is about quarter wave-length $\frac{\lambda}{4}$ of the acoustic oscillation. The wave length λ is the spacing between two successive positions throughout the propagation of the acoustic wave where the pressure amplitude values are the

same. One-half length thermoacoustic resonator is presented in Figure 1.16 (a). As showed in Figure 1.16 (b), the quarter wavelength Hofler resonator is composed of a large diameter tube, a small diameter tube and buffer volume at end in series.

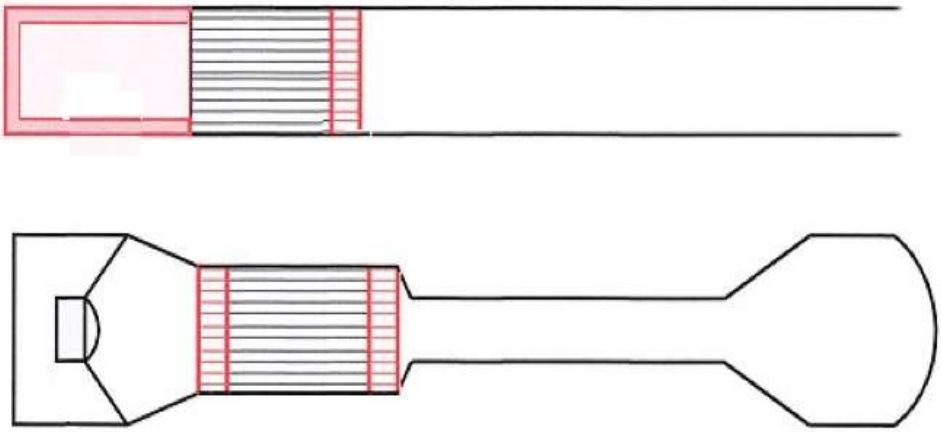

Figure 1.16: Common shapes of the resonator tube

1.7.2 Thermoacoustic core

A standing wave thermoacoustic engine has a principal thermoacoustic element called core (TAC). The TAC is composed of a hot exchanger, inner core and a cold exchanger. Generally, the inner core is constructed of a solid material with permeable pores that allow the working gas to experience a thermodynamic cycle when it is in contact with the solid walls. Previous studies found out that maximum acoustic production is generated when the TAC is placed nearby the pressure antinode. An imperfection of thermal contact between the working fluid and the stack walls has the effect of providing the appropriate phase delay between the reversed heat transfer. The inner thermoacoustic core is a porous medium defined generally as either a solid matrix with many shaped channels or a collection of solid bodies. So, defined as a solid matrix containing interconnected pores, the TAC domain allows the propagation of the working fluid within the system. The flowing fluid may therefore exchange mass and energy with the pores walls. In effect, the performance of a thermoacoustic device depends strongly on the thermophysical properties and geometry of the porous core.

	Ceramics	Copper	RVC
Density $[Kg/m^3]$	2500	8960	49500
Thermal conductivity $[W/mK]$	1.46	386	0.05
Specific heat $[J/kgK]$	1000	383	1260

Table 1.1: Thermophysical properties of the porous material used as inner thermoacoustic core

Adeff et al. [28] confirmed that the employ of a random porous vitreous carbon RVC has the same performance as an uniform stack geometry in thermoacoustic devices. Then, Garrett [29] stated that the porous core must typically fill less than 10% of the overall thermoacoustic device volume. In effect, the TAC can be constructed by material with substantial surface area, high porosity and low thermal conductivity [30]. Previous study focus experimentally on the examination of the the acoustic sensitivity and level of noise by the use of different materials such as Reticulated Vitreous Carbon (RVC), Nichrome and stainless steel grids. Furthermore, using the computational fluid simulation, Jensen [31] predicted numerically the thermoacoustic performance of porous core materials by quantifying their acoustic properties. Such simulation proved the dependency of pore geometry and nonlinear effects by investigating the thermoacoustic propagation within various fibrous geometries with applied temperature gradient.

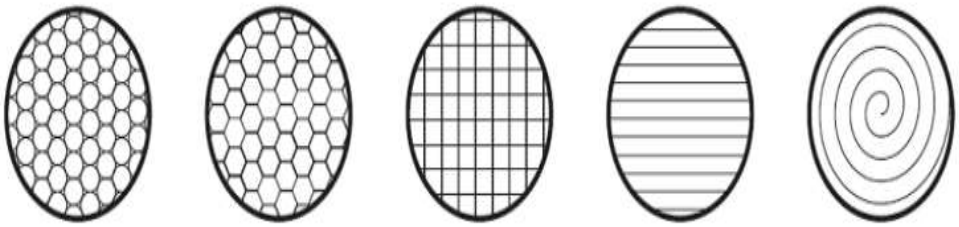

Figure 1.17: Various geometries used as stack geometry: honeycombs, square tubes, pins arrays, parallel plates and spiral shapes

The common geometries of thermoacoustic stacks are honeycombs, square tubes, pins arrays, parallel plates and spiral shapes as can be seen in Figure 1.17 [32]. The adequate geometry lead principally to achieve the demanded imperfect thermal contact required to obtain the proper phasing between the acoustic wave and the heat transfer.

The most used material for the construction of porous stack are ceramics, celcor, stainless steel and aluminium. For standing wave generation, the inner core material required must have feeble thermal conductivity and important specific heat capacity as illustrated in Table 1.1 [33].

1.7.3 Working fluid

The thermophysical features of gas such as the density, the thermal conductivity, Prandtl number and the specific heat capacity and their variation with temperature are the fundamental parameters for the selection of the corresponding thermoacoustic working gas. Correspondingly, the fluid properties affect strongly the operation of the device.

Basically, inert fluids with low Prandtl number and high ratio of specific heats are desirable to work within thermoacoustic devices. In effect low Prandtl number gases promotes the thermoacoustic conversion. Such working gases are also suitable for their properties as the high thermal conductivity that improves the intermolecular interaction with the porous medium walls of the thermoacoustic core. In addition, such fluid properties serves in the minimization of the flow thermo-viscous dissipation.

The performance of thermoacoustic devices can be optimized by the use of a mixtures of light and heavy noble gases. Gases mixture becomes required further to their lower value of Prandtl number compared to that for pure noble gases. The thermophysical properties of the usefull working gases in such devices are given as follow [34]:

	Argon	Air	Helium	Neon
Density $[Kg/m^3]$	1.623	1.223	0.163	0.821
Thermal conductivity $[W/mK]$	0.0177	0.0261	0.15	0.0491
Specific heat $[J/kgK]$	521.6	1005	5197	1029.9
Specific heat ratio	1.667	1.4	1.667	1.667

Table 1.2: Thermophysical properties of the working fluids within thermoacoustic devices

1.8 conclusion

In the first part of this chapter a brief history about the discovery and the development of the thermoacoustic field is outlined. Then, an overview about the the thermoacoustic theory is provided. At the following parts, the applications and configurations of the diverses thermoacoustic devices are presented. Therefore, the fifth part gives a description of the appropriate thermodynamic cycles experienced within the different thermodynamic conversion processes. At the final part of this chapter, a special regard to the standing wave thermoacoustic cycle is given. The common useful materials and structure has been detailed.

Bibliography

[1] B Higgins. On the sound produced by hydrogen gas. *Nicholson's Journal*, 1:130, 1802.

[2] Karl Thomas Feldman Jr, H Hirsch, and RL Carier. Experiments on the sondhauss thermoacoustical phenomenon. *The Journal of the Acoustical Society of America*, 39(6):1236–1236, 1966.

[3] PL Rijke. Notiz über eine neue art, die in einer an beiden enden offenen röhre enthaltene luft in schwingungen zu versetzen. *Annalen der Physik*, 183(6):339–343, 1859.

[4] Gustav Kirchhoff. Ueber den einfluss der wärmeleitung in einem gase auf die schallbewegung. *Annalen der Physik*, 210(6):177–193, 1868.

[5] JWS Lord. Rayleigh, the theory of sound, 1945.

[6] HA Kramers. Vibrations of a gas column. *Physica*, 15(11-12):971–984, 1949.

[7] Ralph VL Hartley. Electric power source. *US Classification*, 290(1.00), 1951.

[8] Warren A Marrison. Heat-controlled acoustic wave system, May 27 1958. US Patent 2,836,033.

[9] RL Carter, M White, and AM Steele. Private communication of atomics international division of north american aviation. *Inc., September*, 24, 1962.

[10] P Merkli and H Thomann. Thermoacoustic effects in a resonance tube. *Journal of fluid mechanics*, 70(1):161–177, 1975.

[11] GW Swift. Analysis and performance of a large thermoacoustic engine. *the Journal of the Acoustical Society of America*, 92(3):1551–1563, 1992.

[12] Thomas James Hofler. *THERMOACOUSTIC REFRIGERATOR DESIGN AND PERFORMANCE (HEAT ENGINE, RESONATOR, MICROPHONE)*. PhD thesis, University of California, San Diego, 1986.

[13] Jay A Adeff and Thomas J Hofler. Design and construction of a solar thermal powered thermo-acoustically driven thermoacoustic refrigerator. *The Journal of the Acoustical Society of America*, 107(5):2795–2795, 2000.

[14] T Yazaki, A Iwata, T Maekawa, and A Tominaga. Traveling wave thermoacoustic engine in a looped tube. *Physical Review Letters*, 81(15):3128, 1998.

[15] Swift Backhaus and GW Swift. A thermoacoustic stirling heat engine. *Nature*, 399(6734):335–338, 1999.

[16] Scott Backhaus and Greg W Swift. A thermoacoustic-stirling heat engine: Detailed study. *The Journal of the Acoustical Society of America*, 107(6):3148–3166, 2000.

[17] Orest G Symko, E Abdel-Rahman, YS Kwon, M Emmi, and R Behunin. Design and development of high-frequency thermoacoustic engines for thermal management in microelectronics. *Microelectronics Journal*, 35(2):185–191, 2004.

[18] Kees De Blok. Low operating temperature integral thermo acoustic devices for solar cooling and waste heat recovery. *Journal of the Acoustical Society of America*, 123(5):3541–3541, 2008.

[19] N Rott. 1980, thermoacoustics, adv. appl. mech., 20, academic press new york, ny.

[20] Gregory W Swift. Thermoacoustic engines. *the Journal of the Acoustical Society of America*, 84(4):1145–1180, 1988.

[21] Michael AG Timmer, Kees de Blok, and Theo H van der Meer. Review on the conversion of thermoacoustic power into electricity. *The Journal of the Acoustical Society of America*, 143(2):841–857, 2018.

[22] Tao Jin, Bao-sen Zhang, Ke Tang, Rui Bao, and Guo-bang Chen. Experimental observation on a small-scale thermoacoustic prime mover. *Journal of Zhejiang University-SCIENCE A*, 8(2):205–209, 2007.

[23] John J Wollan, Gregory W Swift, SN Backhaus, and David L Gardner. Development of a thermoacoustic natural gas liquefier. Technical report, 2002.

[24] http://www.thatea.eu.

[25] Islam A Ramadan, Hélène Bailliet, Gaëlle Poignand, and David Gardner. Design, manufacturing and testing of a compact thermoacoustic refrigerator. *Applied Thermal Engineering*, 189:116705, 2021.

[26] Peter H Ceperley. Gain and efficiency of a traveling wave heat engine. *The Journal of the Acoustical Society of America*, 72(6):1688–1694, 1982.

[27] Kees de Blok. Novel 4-stage traveling wave thermoacoustic power generator. In *Fluids Engineering Division Summer Meeting*, volume 49491, pages 73–79, 2010.

[28] Jay A Adeff, Thomas J Hofler, Anthony A Atchley, and William C Moss. Measurements with reticulated vitreous carbon stacks in thermoacoustic prime movers and refrigerators. *The Journal of the Acoustical Society of America*, 104(1):32–38, 1998.

[29] Steven L Garrett. Resource letter: Ta-1: Thermoacoustic engines and refrigerators. *American Journal of Physics*, 72(1):11–17, 2004.

[30] Flávio C Bannwart, Guillaume Penelet, Pierrick Lotton, and Jean-Pierre Dalmont. Measurements of the impedance matrix of a thermoacoustic core: Applications to the design of thermoacoustic engines. *The Journal of the Acoustical Society of America*, 133(5):2650–2660, 2013.

[31] Carl Jensen and Richard Raspet. Thermoacoustic properties of fibrous materials. *The Journal of the Acoustical Society of America*, 127(6):3470–3484, 2010.

[32] Mahmoud A Alamir. Thermoacoustic energy conversion devices: novel insights. *Journal of Advanced Research in Fluid Mechanics and Thermal Sciences*, 77(2):130–144, 2021.

[33] Syeda Humaira Tasnim, Shohel Mahmud, and Roydon Andrew Fraser. Compressible pulsating convection through regular and random porous media: The thermoacoustic case. *Heat and Mass Transfer*, 48(2):329–342, 2012.

[34] Abdullah A Alshorman. Analysis of thermoacoustic cooling and refrigeration for performance enhancement.

Chapter 2

Lattice Boltzmann method

2.1 Introduction

The lattice Boltzmann method is an efficient technique for the resolution of real engineering systems and handling complex geometries and phenomenon. This new approach comes instead of traditional computational fluid techniques such as finite volumes, finite elements and finite difference for solving the Navier-Stocks equations. The Lattice Boltzmann model is mainly based on the dynamic statistics for the prediction of the fluid dynamic flow and heat transfer problems on a mesoscopic scale. In the eighteen's of the past decade, MC Namara and Zanetti [1] introduced the lattice Boltzmann method to resolve the lattice gas automata for statistical noise. The fluid is explicitly designed as fractious particles that stream and collide following specific lattice directions. Besides, the lattice Boltzmann equation is judged linear since the nonlinearity is integrated implicitly in the advection term.

In this chapter, the theory of gases at the mesoscopic scale known as the kinetic theory of gases is described and the lattice Boltzmann method is introduced in the second part. The Bhatnagar-Gross-Krook approximation is detailed at the third part. Then, the various arrangement of lattices are presented followed by the discretization models of the equations of conservation. Thereafter, the extended method for the simulation of porous medium and thermoacoustic field are established respectively. Finally, the adequate boundary conditions to a standing wave thermoacoustic engine are developed.

2.2 Kinetic theory

The lattice Boltzmann method is mainly based on the mesoscopic kinetic theory and being used for the simulation of the macroscopic behaviour. Precisely, the kinetic model adress the critical physics with the microscopic or mesoscopic processes where the averaged macroscopic properties satisfy the macroscopic terms of the system of equations. A detailed description on the microscopic scale is approximated via the mesoscopic kinetic theory to find the equations of macroscopic fluid mechanics.

LBM is presented with particular regards to acoustic field specifications. For fluid mechanics investigations the fluid flow is assumed to be the topic then the fluid is almost considered

incompressible. Besides, that theory seems to be incompatible with the compressible phenomenon of sound under a constant density. For acoustic systems handling, the fluid is almost assumed to be at rest or nearly so. Actual methodology works by tracking the movement and the inetrmolecular interaction of particle distributions inside the computational system.

2.3 Lattice Boltzmann equation

The kinetic theory indicates that the evolution of particles interaction are described by the Boltzmann equation. That equation is a partial differential equation that governs the transport phenomenon and describes the evolution of the distribution function $f(x,c,t)$. The quantity $f(x,c,t)$ statistically represents the mass density at position x contributed by all particles at the moment time t located between positions x and $x+dx$ having velocities respectively c and $c+dc$ after certain time dt.

An external force F acts on a particle mass m will change location from x position to $x+cdt$ and the velocity of the molecule from c to $c+\frac{F}{m}dt$. Therefore, if molecule number does not change by the effect of the external force F and the molecules does not collide:

$$f(x+cdt,c+\frac{F}{m}dt,t+dt)dxdt - f(x,c,t)dxdt = 0 \tag{2.1}$$

Otherwise, if the collision occurs between the molecules it results a net rate of variation of the distribution function f in the interval dt. Hence, the difference between between final and initial situations of the distribution function is known as the collision operator Ω. The equation for evolution of the distribution function is therefore expressed as:

$$f(x+cdt,c+Fdt,t+dt)dxdt - f(x,c,t)dxdt = \Omega(f)dxdcdt \tag{2.2}$$

The aforementioned expression can further be simplified by dividing $dtdxdc$ and by tending dt towards zero as:

$$\frac{f(x+cdt,c+Fdt,t+dt) - f(x,c,t)}{dt} = \Omega(f) \tag{2.3}$$

Or it can be simply written as:

$$\Omega(f) = \frac{\partial f}{\partial t} \tag{2.4}$$

The mentioned equation states that the collision rate is equal to the total rate of difference of the number of molecules between t and $t + dt$ where it is expanded as:

$$df = \frac{\partial f}{\partial x}dx + \frac{\partial f}{\partial c}dc + \frac{\partial f}{\partial t}dt \tag{2.5}$$

Substituting (2.4) and (2.5):

$$\Omega(f) = \frac{\partial f}{\partial x}\frac{dx}{dt} + \frac{\partial f}{\partial c}\frac{dc}{dt} + \frac{\partial f}{\partial t}\frac{dt}{dt} \tag{2.6}$$

The equation is therefore expressed as,

$$\Omega(f) = \frac{\partial f}{\partial x}c + \frac{\partial f}{\partial c}a + \frac{\partial f}{\partial t} \tag{2.7}$$

where $a = \frac{dx}{dt}$ is the acceleration and may be expressed following the second law of Newton as $a = \frac{F}{m}$. without the existence of external force (2.7) is written as:

$$\frac{\partial f}{\partial t} + c\nabla f = \Omega(f) \tag{2.8}$$

From the above equations, the macroscopic quantities such as the fluid density ρ, the velocity vector u and internal energy e are therefore expressed as follow:

$$\rho(x,t) = \int f(x,c,t)dc \tag{2.9}$$

$$\rho(x,t)u(x,t) = \int mcf(x,c,t)dc \tag{2.10}$$

$$\rho(x,t)e(x,t) = \frac{1}{2}\int (c-u)^2 f(x,c,t)dt \tag{2.11}$$

The equations (2.9), (2.10) and (2.11) design respectively the equation of mass, momentum and energy conservation.

2.4 Bhatnagar-Gross-Krook approximation

The resolution of the Boltzmann equation seems difficult due to the complexity of the collision term. In 1954, Bhatnagar, Gross and Krook introduced the BGK approximation [2] to simplify the complications related to the resolution of the collision operator. The solution is based on adapting a simple collision operator in conformity with a single relaxation time (SRT). That assumption serving to obtain a negligible margin of error to the outcome. It becomes the most utilized operator due to its advanced computational efficiency:

$$\Omega = \tau^{-1}(f^{eq} - f) = \omega(f^{eq} - f) \tag{2.12}$$

τ design the relaxation time between two successive collisions, ω is the corresponding collision frequency. f^{eq} represents the local equilibrium distribution function called also Maxwell-Boltzmann distribution function.

Therefore, the equation describing the evolution of the distribution function under BGK approximation in term of pace, speed and time (2.7) can be expressed as:

$$\frac{\partial f}{\partial t} + c\nabla f = \tau^{-1}(f^{eq} - f) \tag{2.13}$$

Hence, the above equation 2.13 becomes valid and applicable following each lattice direction i as:

$$\frac{\partial f_i}{\partial t} + c_i\nabla f_i = \tau^{-1}(f_i^{eq} - f_i) \tag{2.14}$$

The spatial and temporal discretization of the above equation gives the so called BGK equation as:

$$f_i(x + c_i\Delta t, t + \Delta t) - f_i(x,t) = \Delta t\,\tau^{-1}(f_i^{eq}(x,t) - f_i(x,t)) \tag{2.15}$$

This equation can be simply applied for many physic systems and applications by simply specifying the equilibrium distribution function.

Two main steps are involved for the resolution of the above equation the method:

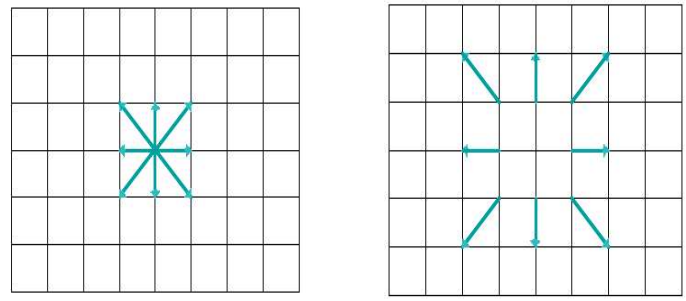

(a) (b)

Figure 2.1: (a) collision step (b) streaming step

- **Collision step**: The left side of the discrete evolution equation reveals the collision step(Figure 2.1. (a)). At the same node, the momentum exchange tackes place by the local collision of the particles with each other. It can be mathematically expressed as:

$$f_i(x+c_i\Delta t, t+\Delta t) = f_i(x,t)(1-\omega) + \omega f_i^{eq}(x,t) \tag{2.16}$$

- **Streaming step**: The right side of the discrete evolution equation reveals the streaming step(Figure 2.1. (b)).The particles are transported to the nearest neighbours along particular velocity direction without changing the distributions. It is stated as:

$$f_i(x+c_i\Delta t, t+\Delta t) = f_i(x,t+\Delta t) \tag{2.17}$$

2.5 Lattice arrangements

In lattice Boltzmann method, the domain needs to be discretized into equidistant segments by a finite number of nodes. Each node is considered as a particle where distribution functions are applied. The discretized velocity in Boltzmann equation is considered continuous in physical space and time. A specified lattice Boltzmann configuration is executed depending on the dimension of the problem and the number of speed directions. Accordingly, at the standard terminology, the lattice Boltzmann schemes are denoted as D_nQ_m. n is the space dimension (Unidimensional, bidimensional or threedimensional) and m is the number of microscopic ve-

locities directions. These discretizations are linked together which leads the lattice Boltzmann equation to have simple two steps in spatial and temporal evolution consisting of collision and streaming as mentioned respectively in (2.16) and (2.17).

2.5.1 Unidimensional model

The most used unidimensional configuration are respectively:

- D_1Q_3

  D_1Q_3 is the most popular unidimensional model. The particle lying at the central node (0) is at rest. Three vectors, corresponding to three distribution functions, are presented as in Figure 2.2. For $\Delta x = \Delta t = 1$, the discrete velocities and the corresponding weighing factors are:

$\vec{c}_0 = (0,0)$	$\omega_0 = \frac{4}{6}$
$\vec{c}_1 = (1,0)$	$\omega_1 = \frac{1}{6}$
$\vec{c}_2 = (-1,0)$	$\omega_2 = \frac{1}{6}$

Table 2.1: Unidimensional arrangement D_1Q_3 parameters

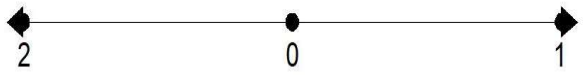

Figure 2.2: Configuration of unidimensional D_1Q_3

- D_1Q_5

  five vectors, corresponding to five distribution functions, are presented as in Figure 2.3. The particle at the central node is at rest with nil velocity. The velocity vectorsare defied as in Table 2.2 For $\Delta x = \Delta t = 1$, the discrete velocities and the corresponding weighing factors are:

$\vec{c}_0$ = (0,0)	$\omega_0=\frac{6}{12}$
$\vec{c}_1$ = (1,0)	$\omega_1=\frac{2}{12}$
$\vec{c}_2$ = (-1,0)	$\omega_2=\frac{2}{12}$
$\vec{c}_3$ = (2,0)	$\omega_1=\frac{1}{12}$
$\vec{c}_4$ = (-2,0)	$\omega_2=\frac{1}{12}$

Table 2.2: Unidimensional arrangement D_1Q_5 parameters

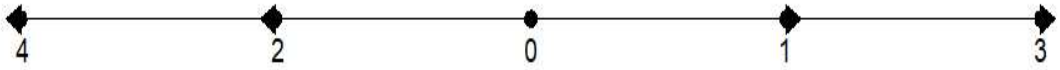

Figure 2.3: Configuration of unidimensional arrangement D_1Q_5

2.5.2 Bidimensional model

As minimum Five vectors, corresponding to five distribution functions, are presented as in Figure 2.4 (a). The most popular is the D_2Q_9 arrangement. For D_2Q_9 arrangement and Δx= Δt=1, the discrete velocities and the corresponding weighing factors are:

$\vec{c}_0$ = (0,0)	$\omega_0=\frac{4}{9}$
$\vec{c}_1$ = (1,0)	$\omega_1=\frac{1}{9}$
$\vec{c}_2$ = (0,1)	$\omega_2=\frac{1}{9}$
$\vec{c}_3$ = (-1,0)	$\omega_3=\frac{1}{9}$
$\vec{c}_4$ = (0,-1)	$\omega_4=\frac{1}{9}$
$\vec{c}_5$ = (1,1)	$\omega_5=\frac{1}{36}$
$\vec{c}_6$ = (-1,1)	$\omega_6=\frac{1}{36}$
$\vec{c}_7$ = (-1,-1)	$\omega_7=\frac{1}{36}$
$\vec{c}_8$ = (1,-1)	$\omega_8=\frac{1}{36}$

Table 2.3: Bidimensional arrangement D_2Q_9 parameters

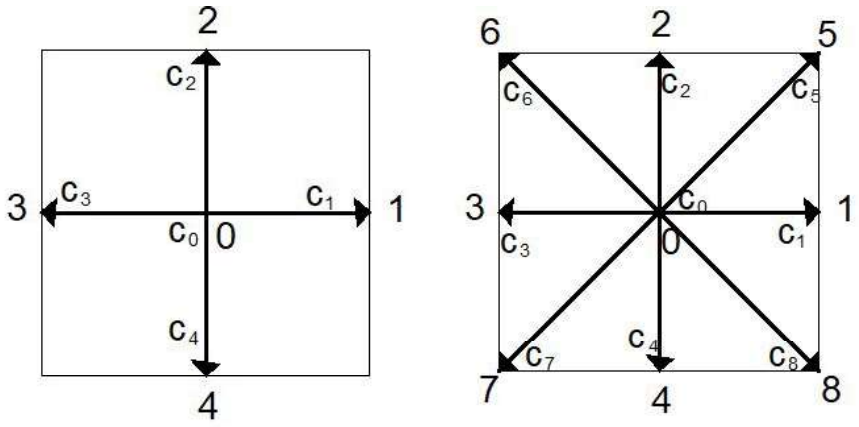

(a) (b)

Figure 2.4: (a) D_2Q_4 (b) D_2Q_9

2.5.3 Tree dimensional model

The D_3Q_{15} arrangement is showed as in Figure 2.5. For $\Delta x = \Delta t = 1$, the discrete velocities and the corresponding weighing factors are given in Table 2.4.

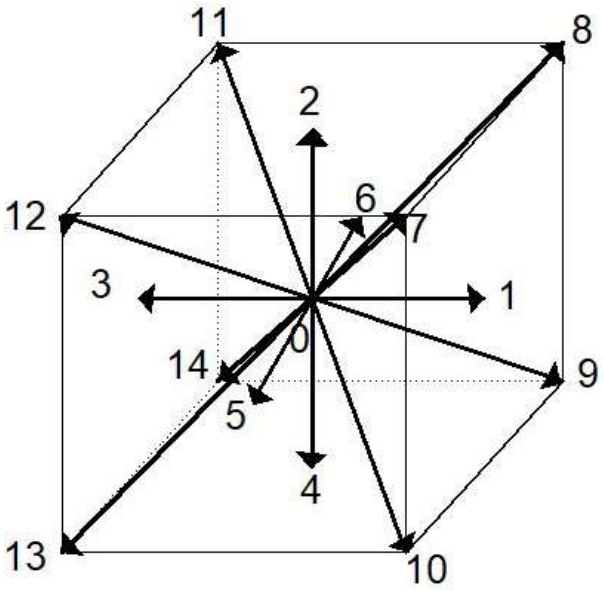

Figure 2.5: Three-dimensional configuration arrangement D_3Q_{15}

$\vec{c}_0$ = (0,0,0)	ω_0=$\frac{16}{72}$
$\vec{c}_1$ = (1,0,0)	ω_1=$\frac{8}{72}$
$\vec{c}_2$ = (0,1,0)	ω_2=$\frac{8}{72}$
$\vec{c}_3$ = (-1,0,0)	ω_3=$\frac{8}{72}$
$\vec{c}_4$ = (0,-1,0)	ω_4=$\frac{8}{72}$
$\vec{c}_5$ = (0,0,1)	ω_5=$\frac{8}{72}$
$\vec{c}_6$ = (0,0,-1)	ω_6=$\frac{8}{72}$
$\vec{c}_7$ = (1,1,1)	ω_7=$\frac{1}{72}$
$\vec{c}_8$ = (1,1,-1)	ω_8=$\frac{1}{72}$
$\vec{c}_9$ = (1,-1,1)	ω_9=$\frac{1}{72}$
$\vec{c}_{10}$ = (1,-1,-1)	ω_{10}=$\frac{1}{72}$
$\vec{c}_{11}$= (-1,1,-1)	ω_{11}=$\frac{1}{72}$
$\vec{c}_{12}$= (-1,1,1)	ω_{12}=$\frac{1}{72}$
$\vec{c}_{13}$= (-1,-1,1)	ω_{13}=$\frac{1}{72}$
$\vec{c}_{14}$= (-1,-1,-1)	ω_{14}=$\frac{1}{72}$

Table 2.4: Threedimensional arrangement D_3Q_{15} parameters

2.6 Equilibrium distribution function

f^{eq} denotes the local equilibrium distribution function extracted from the distribution function of Maxwell Boltzmann:

$$f^{eq}(x,t) = \rho(x,t)(\frac{m}{2\pi k_B T})^{\frac{D}{2}} exp(\frac{-m(\vec{c}-\vec{u}(x,t))^2}{2k_B T}) \tag{2.18}$$

ρ , $\vec{u}$ and T indicates respectively the macroscopic density, velocity and température. D is the space dimension and k_B is the Boltzmann constant. The seed of sound c_s is therefore defined as:

$$c_s = \frac{k_B T}{m} \tag{2.19}$$

with the assumption of low-Mach number

$$f^{eq}(x,t) = \frac{\rho(x,t)}{2\pi c_s^2} exp(\frac{-(c-u)^2}{2c_s^2})(\frac{m}{2\pi k_B T})^{\frac{D}{2}} exp(\frac{-m(\vec{c}-\vec{u}(x,t))^2}{2k_B T}) \tag{2.20}$$

using the third order in the Taylor series expansion, the Maxwell distribution function is rewritten as:

$$f^{eq}(x,t) = \omega_i \rho(x,t)[1 + \frac{c_i u}{c_s^2} + \frac{(c_i u)^2}{2c_s^4} - \frac{u^2}{2c_s^2}] \tag{2.21}$$

where the weighing factor is $\omega_i = (\frac{m}{2\pi k_B T})^{\frac{D}{2}} exp(\frac{-(c-u)^2}{2c_s^2})$ and the velocity along the lattice direction is c_i.

2.7 Extended lattice Boltzmann method for porous medium simulation

The lattice Boltzmann method is capable for the simulation of the flow within complex geometries and deals with diverse boundary conditions. The so-called Darcy-Brinkman-Forchheimer model [3] is adopted for the investigation of fluid flow and heat transfer within a porous structure at larger for a larger scale than the molecular dynamics. The presence of porous medium is indicated by including the porosity $\ll\varepsilon\gg$ into the equilibrium distribution function. Furthermore, additional force term are provided to the evolution equation accounting for for the linear and nonlinear drag forces.

Dynamic field

The fluid flow within a porous medium is confronted with different kind of forces as buoyancy and forces caused by the interaction of fluid particles and the porous matrix walls. Then, the evolution of the Boltzmann equation under BGK approximation is written as:

$$f_i(x + c_i\Delta t, t + \Delta t) - f_i(x,t) = -\Delta t {\tau_m}^{-1}[f_i(x,t) - f_i^{eq}(x,t)] + \Delta t F_{ei} \tag{2.22}$$

The equilibrium distribution function f_i^{eq} is given by:

$$f_i^{eq} = \rho\omega_i\Big[1 + \frac{c_i\vec{u}}{c_s^2} + \frac{(c_i\vec{u})^2}{2\varepsilon c_s^4} - \frac{\vec{u}\vec{u}}{2\varepsilon c_s^2}\Big] \tag{2.23}$$

c_s is the discrete microscopic speed of sound equal to $\frac{1}{\sqrt{3}}$ in D_2Q_9 LBM structure. ω_i is the weigh coefficient of each lattice.

F_{ei} is the total body force exercised on the fluid flow. It takes the following form:

$$F_{ei} = F\frac{(c_i - u)^2}{RT_{ref}} f^{eq}{}_i \tag{2.24}$$

F design the dimensionless form of the total body force expressed as [4–6]:

$$F = -\varepsilon[\frac{1}{ReDa} + \frac{F_\varepsilon}{\sqrt{Da}} \mid u \mid]u + \varepsilon G \tag{2.25}$$

The first term identify the "Darcy term" which account to the drop of pressure through the porous core and the second term is the Forchheimer drags expressing the nonlinear effect occurred within the porous material.

G is the buoyancy force:

$$G = Pr.Ra.(\theta - \theta_{ref}) \tag{2.26}$$

where Ra and Pr indicates respectively Rayleigh and Prandtl numbers.

The macroscopic density is obtained as:

$$\rho(x,t) = \sum_i f_i(x,t) \tag{2.27}$$

Then, the discrete velocity is calculated using the following formula:

$$\rho(x,t)u(x,t) = \sum_i c_i f_i(x,t) + \rho(x,t)\Delta t F_{ei} \tag{2.28}$$

The pressure at a node x should be defined as:

$$p(x,t) = c_s^2 \rho(x,t) \tag{2.29}$$

Thermal field

The thermal LBM in models the flow in porous media having complex structure networks is writing as [7]:

$$g_i(x+c_i\Delta t,t+\Delta t)-g_i(x,t)=\frac{1}{\tau_{sm}})[g_i(x,t)-g_i^{eq}(x,t)]+\Delta t\tilde{\phi}_i \tag{2.30}$$

where the equilibrium distribution function is defined as:

$$g_i^{eq}(x,t)=\theta(x,t)\omega_i[1+\frac{c_iu}{c^2}] \tag{2.31}$$

$$g_i^{eq}(x,t)=\theta(x,t)\omega_i[1+\frac{c_iu}{c^2}+\frac{(c_iu)^2}{2c^4}-\frac{u^2}{2c^2}] \tag{2.32}$$

τ_{sm} determine the nature of heat exchange between the fluid particles and the porous solid walls defined as [8–10]:

$$\tau_{sm}=3Pr(\tau_m-0.5)C+0.5 \tag{2.33}$$

where C and Prandt number Pr are respectively expressed:

$$C=\frac{R_k}{R_C} \qquad Pr=\frac{\mu C_{pf}}{k_f} \tag{2.34}$$

The thermal capacity ratio R_c and the conductivity ratio R_k are expressed as [9]:

$$R_c=\varepsilon+(1-\varepsilon)\frac{(\rho C_p)_s}{(\rho C_p)_f} \quad and \quad R_k=\varepsilon+(1-\varepsilon)\frac{k_s}{k_f} \tag{2.35}$$

The viscous heat dissipation is expressed as:

$$\tilde{\phi}_i=\omega_i[1+\frac{c_iu}{{c_s}^2}(\frac{\tau_{sm}-0.5}{\tau_{sm}})]\tilde{\phi} \tag{2.36}$$

Therefore, the dimensionless temperature can be calculated using the following equation:

$$\theta(x,t)=\sum_i g_i(x,t) \tag{2.37}$$

2.8 Lattice Boltzmann method applied to computational thermoacoustics

The ability of lattice Boltzmann method (LBM) for the simulation of thermoacoustic problems has been well confirmed by Wang [11–13] and Shan [14]. Previous studies proves the quantitative agreement of LBM results with the experimental data and the other conventional numerical methods. Those efforts demonstrates the performance of such numerical method progress in the comprehension of the thermoacoustic conversion fundamentals. Besides, Rafat et al. [15] simulated the acoustic streaming within standing wave tubes using a scheme based on LBM. Results found show good correspondence to the acoustic linear theory. Therefore, Kam et al. [16] demonstrates the feasibility the Boltzmann method for the simulation of thermoacoustic waves within a two dimensional enclosures.

The Boltzmann equation is mainly resolved considering the variation of density with temperature (Boussinesq approximation). For the simulation of thermoacoustic systems, the fluid flow is assumed to be laminar and weakly compressible (low Mach number Ma ≤ 0.3) and can be invoked as the nearly incompressible limit.

2.9 Boundary condition

Based on Navier-Stockes equations, the determination of the distribution functions to resolve the desired macroscopic conditions can be found by several ways. In lattice Boltzmann method, the inward distribution functions must be determined at the boundaries. By that way, the implementation of the boundary conditions in complex geometries is further simple without affecting the numerical stability or accuracy. Actually, the appropriate boundary conditions applied for modeling the adequate physical boundaries are further explained.

Dynamic boundary conditions

- **Open boundary**: sometimes the velocity at a boundary is unknown. In that case, the usual solution concerns the unknown distribution function extrapolation. For unknown

velocity at the outlet boundary, it can be written as:

$$\begin{aligned} f_1 &= 2f_{1/n-1} - f_{1/n-2} \\ f_5 &= 2f_{5/n-1} - f_{5/n-2} \\ f_8 &= 2f_{8/n-1} - f_{8/n-2} \end{aligned} \tag{2.38}$$

Sometimes, the above condition results unstable solutions. So, adopting first order extrapolation boundary condition can lead to higher stability than the second order scheme. The following equation can therefore be used to reduce the instability:

$$\begin{aligned} f_1 &= f_{1/n-1} \\ f_5 &= f_{5/n-1} \\ f_8 &= f_{8/n-1} \end{aligned} \tag{2.39}$$

- **Bounce-Back**: Principally used in case of nonslip condition, solid stationary or for modeling flow-over obstacles. This condition can be simply applied and it implies that an incoming particle towards the solid boundary bounces back into flow domain. The wall is situated at a half the distance from the lattice sites so some distribution functions are obtained from the streaming process. Thus, the implementation of the boundary condition comes after identifying streamlines. At the outlet boundary, this condition is expressed as:

$$\begin{aligned} f_1 &= f_{1/n-1} \\ f_5 &= f_{5/n-1} \\ f_8 &= f_{8/n-1} \end{aligned} \tag{2.40}$$

It can be noted that the bounce back condition guarantees the conservation of mass and momentum quantities at the walls. Otherwise, a practicable arrangement exist when the subjected region extend within the solid boundary.

- **Reflective wall**: The specular reflective bounce-back condition implies that an incoming particle towards the solid boundary is reflected or partially reflected into flow domain. For a specified boundary it can be written as [17]:

$$f_k = r f_k^- + (1-r) f_k^* \tag{2.41}$$

noting that k^* is the mirror lattice and the k^- is the opposite one. r design the reflection coefficient describing the reflection of bounce-back at the wall while $(1-r)$ describes the slip coefficient. The reflection coefficient r corresponds to pure specular refection when it is nil while pure bounce-back reflection is described when $r = 1$ [18].

- **Symmetric condition**: Lot of problems exhibit symmetry condition in relation to a specific axis or plane. This condition lead to simplify the problem resolution, it is enough to resolve the problem for just a side of the system. In other world, the problem resolution is carried only for one portion of the domain where symmetry boundary condition is applied at the axis of symmetry. The distribution functions at the untreated boundary are unknown. The way to construct these functions is to set them equal to their mirror images as: $f_i = fi^*$. For the problem of two dimensional channel, the flow at the top part the symmetry axis is the mirror image of the flow at bottom part so the condition is written as:

$$f_5 = f_8 \quad f_2 = f_4 \quad f_6 = f_7 \tag{2.42}$$

Figure 2.6: Illustrative drawing of basic lattices used for fluid-solid interface treatment

- **Fluid-solid interface treatment**: Non-slip boundary condition is imposed at the fluid solid interface to ensure fluid flow continuity and is written as [19]:

$$f_{i/s} = f_{i/f} \tag{2.43}$$

Where i denote the appropriate lattice index as illustrated in Figure 2.6 and s and f indicates respectively the solid and the fluid phases.

Thermal boundary conditions

- **Isothermal walls** : When the wall is set at constant or the temperature of the inlet flow to the domain is constant, the Dirichlet boundary condition is the suitable condition to apply. For example, if the upper and lower boundaries are isothermal at $\theta = \theta_w$, the condition is written resoactively as [20]:

$$\begin{aligned} g_4 &= \theta_w(w_4 + w_2) - g_2 \\ g_7 &= \theta_w(w_7 + w_5) - g_5 \\ g_8 &= \theta_w(w_8 + w_6) - g_6 \end{aligned} \tag{2.44}$$

and

$$\begin{aligned} g_2 &= \theta_w(w_2 + w_4) - g_4 \\ g_5 &= \theta_w(w_5 + w_7) - g_7 \\ g_6 &= \theta_w(w_6 + w_8) - g_8 \end{aligned} \tag{2.45}$$

- **Boundary with unknown temperature** : The arriving unknown distribution functions are assumed to be at the equilibrium state with an unknown temperature called θ^{eq}. It is determined as the desirable incoming temperature profile can be set. So following the D'Orazio's approach [21] that agrees with the second-order treatment of fluid flow at a boundary. Precisely, the arriving unknown populations are assumed to be at equilibrium state and temperature θ_p.

The unknown temperature at the outlet is formulated as [22]:

$$\begin{aligned} g_3 &= \tfrac{1}{9}\theta^{eq}(1-\tfrac{3}{c_s^2}u) \\ g_6 &= \tfrac{1}{36}\theta^{eq}(1-\tfrac{3}{c_s^2}(u-v)) \\ g_7 &= \tfrac{1}{36}\theta^{eq}(1-\tfrac{3}{c_s^2}(u+v)) \end{aligned} \tag{2.46}$$

θ^{eq} is calculated by:

$$\theta^{eq} = \frac{6(\theta_w - \theta_p)}{1+\frac{3}{c_s^2}u} \tag{2.47}$$

θ_p is the sum of the known distribution functions coming from the adjacent internal wall nodes calculated as:

$$\theta_p = g_0 + g_2 + g_3 + g_4 + g_5 + g_8 \tag{2.48}$$

Then the unknown distributions g_i at the outlet boundary are calculated by:

$$g_i = \omega_i \theta^{eq} \tag{2.49}$$

The fluid domain is set initially isotherm at $\theta_{ref} = \theta_w$.

- **Fluid-solid thermal boundary condition**: The heat transfer continuity at the porous medium limits is numerically ensured as follow for D2Q9 model:

$$\begin{aligned} g_{i_{/x_o}} &= g_{i^-_{/x_o}} \\ g_{i_{/x_o}} &= \frac{4}{3}g_{i_{/x_o+\Delta x}} - \frac{1}{3}g_{i_{/x_o+2\Delta x}} - k_f g_{i^-_{/x_o}} + \frac{4}{3}k_f g_{i^-_{x_o-\Delta x}} - \frac{1}{3}k_f g_{i^-_{/x_o-2\Delta x}} \end{aligned} \tag{2.50}$$

The subscript i^- denotes the opposite lattice index. x_o is the positions of fluid-solid interfaces.

2.10 Lattice Boltzmann method Algorithm

The resolution of the Boltzmann equation is based on the streaming and collision processes. The numerical solution is then realized by an algorithm consisting of the streaming and colli-

sion steps with the application of the adequate boundary conditions.

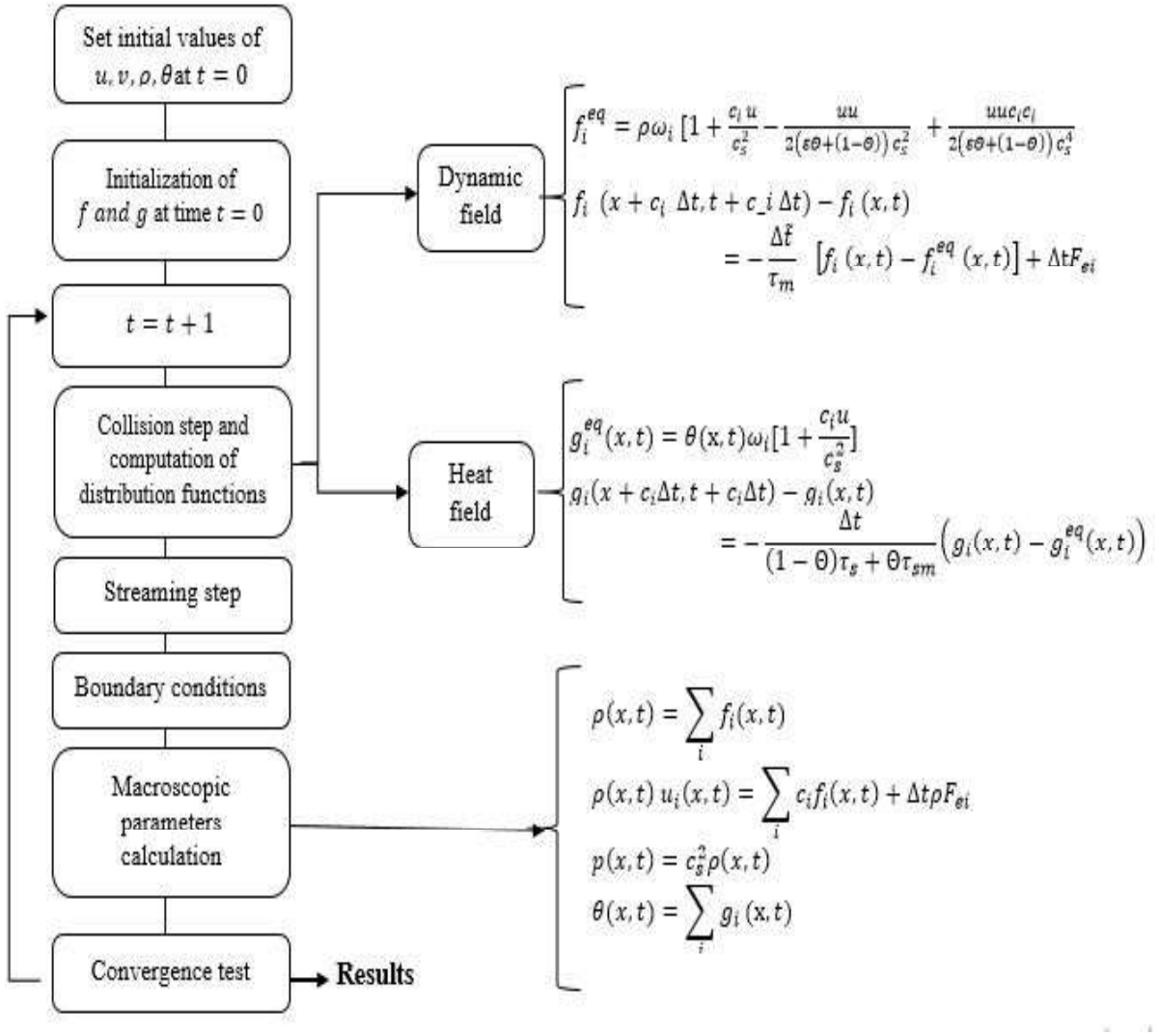

Figure 2.7: Organizational structure of lattice Boltzmann method (LBM) algorithm

2.11 conclusion

In this chapter, the theory of gases and the lattice Boltzmann method are firstly introduced. Then, agreeing with the BGK approximation, the extended lattice Boltzmann method for the simulation of porous medium and thermoacoustic devices is established. The D_2Q_9 model is adopted to investigate our standing wave thermoacoustic system. The boundary conditions at the different walls of the system are developed.

Bibliography

[1] Guy R McNamara and Gianluigi Zanetti. Use of the boltzmann equation to simulate lattice-gas automata. *Physical review letters*, 61(20):2332, 1988.

[2] Prabhu Lal Bhatnagar, Eugene P Gross, and Max Krook. A model for collision processes in gases. i. small amplitude processes in charged and neutral one-component systems. *Physical review*, 94(3):511, 1954.

[3] Zhaoli Guo and TS Zhao. Lattice boltzmann model for incompressible flows through porous media. *Physical review E*, 66(3):036304, 2002.

[4] Bayssain Amami, Hacen Dhahri, and Abdallah Mhimid. Viscous dissipation effects on heat transfer, energy storage, and entropy generation for fluid flow in a porous channel submitted to a uniform magnetic field. *Journal of Porous Media*, 17(10), 2014.

[5] Qing Liu and Ya-Ling He. Double multiple-relaxation-time lattice boltzmann model for solid–liquid phase change with natural convection in porous media. *Physica A: Statistical Mechanics and its Applications*, 438:94–106, 2015.

[6] Qing Liu and Ya-Ling He. Lattice boltzmann simulations of convection heat transfer in porous media. *Physica A: Statistical Mechanics and its Applications*, 465:742–753, 2017.

[7] Jinku Wang, Moran Wang, and Zhixin Li. A lattice boltzmann algorithm for fluid-solid conjugate heat transfer. *International journal of thermal sciences*, 46(3):228–234, 2007.

[8] Edo S Boek, Jonathan Chin, and Peter V Coveney. Lattice boltzmann simulation of the flow of non-newtonian fluids in porous media. *International Journal of Modern Physics B*, 17(01n02):99–102, 2003.

[9] Mahmoud Jourabian, A Ali Rabienataj Darzi, Davood Toghraie, and Omid ali Akbari. Melting process in porous media around two hot cylinders: Numerical study using the lattice boltzmann method. *Physica A: Statistical Mechanics and its Applications*, 509:316–335, 2018.

[10] Dongyan Gao and Zhenqian Chen. Lattice boltzmann simulation of natural convection dominated melting in a rectangular cavity filled with porous media. *International Journal of Thermal Sciences*, 50(4):493–501, 2011.

[11] Yong Wang, Yaling He, Jing Huang, and Qing Li. Implicit–explicit finite-difference lattice boltzmann method with viscid compressible model for gas oscillating patterns in a resonator. *International journal for numerical methods in fluids*, 59(8):853–872, 2009.

[12] Yong Wang, Dong-Ke Sun, Ya-Ling He, and Wen-Quan Tao. Lattice boltzmann study on thermoacoustic onset in a rijke tube. *The European Physical Journal Plus*, 130(1):1–10, 2015.

[13] Yong Wang, YL He, Qing Li, and GH Tang. Numerical simulations of gas resonant oscillations in a closed tube using lattice boltzmann method. *International journal of heat and mass transfer*, 51(11-12):3082–3090, 2008.

[14] Feng Shan, Xiasheng Guo, Juan Tu, Jianchun Cheng, and Dong Zhang. Multi-relaxation-time lattice boltzmann modeling of the acoustic field generated by focused transducer. *International Journal of Modern Physics C*, 28(03):1750038, 2017.

[15] Yasser Rafat, Kaveh Habibi, and Luc Mongeau. Direct numerical simulations of acoustic streaming in standing wave tubes using the lattice boltzmann method. In *Proceedings of Meetings on Acoustics ICA2013*, volume 19, page 045006. Acoustical Society of America, 2013.

[16] EWS Kam, RMC So, and Sau Chung Fu. One-step simulation of thermoacoustic waves in two-dimensional enclosures. *Computers & Fluids*, 140:270–288, 2016.

[17] Ehsan Kamali Ahangar, Mohammad Bagher Ayani, and Javad Abolfazli Esfahani. Simulation of rarefied gas flow in a microchannel with backward facing step by two relaxation

times using lattice boltzmann method–slip and transient flow regimes. *International Journal of Mechanical Sciences*, 157:802–815, 2019.

[18] GH Tang, WQ Tao, and YL He. Lattice boltzmann method for simulating gas flow in microchannels. *International journal of modern physics C*, 15(02):335–347, 2004.

[19] M Sukop and DT Thorne Jr. Lattice boltzmann modeling lattice boltzmann modeling, 2006.

[20] AA Mohamad et al. Fundamentals and engineering applications with computer codes, 2011.

[21] Annunziata D'Orazio, Massimo Corcione, and Gian Piero Celata. Application to natural convection enclosed flows of a lattice boltzmann bgk model coupled with a general purpose thermal boundary condition. *International Journal of Thermal Sciences*, 43(6):575–586, 2004.

[22] H Shokouhmand, F Jam, and MR Salimpour. Simulation of laminar flow and convective heat transfer in conduits filled with porous media using lattice boltzmann method. *International Communications in Heat and Mass Transfer*, 36(4):378–384, 2009.

Chapter 3

Optimization of a standing wave thermoacoustic engine performance by entropy generation minimization

3.1 Introduction

Thermoacoustic technology has promoted several applications in renewable energy [1, 2] and in the reduction of global warming emissions [3]. Furthermore, it is considered as a promising application in low-grade heat recovery [2, 4]. As prime mover, thermoacoustic engines are employed in a large variety of applications such energy regeneration and for microcircuit technology [5]. In effect, those sorts of devices have outstanding features which make them very reliable [6] and ensures long life functioning. Low maintenance is required owing to the simple structure and the lack of moving pieces. Although, the principal components are a straight resonator and a core; the core is composed of a stack sandwiched between cold and hot heat exchangers. Flowing across the stack, the heat absorbed from the hot exchanger is partly converted into acoustic work [7–9].

Much of works [10, 11] states that the thermal to acoustic conversion is governed by several irreversible processes such as nonlinear heat transfer, acoustic streaming and viscous friction. The irreversible process within the device reduce its performance. Indeed, the thermodynamic quality of thermoacoustic engines is evaluated by analyzing the influence of those irreversibilities on the engine performance. Actually, the thermodynamic interaction of the acoustic oscillations within the stack, subject to a temperature gradient, provide significant viscous losses and heat instabilities. The heat exchange process between the working gas and the stack walls occurs irreversibility which limit its efficiency [12, 13]. In fact, heat transfer irreversibility and fluid frictions are the main cause of entropy generation and energy dissipation through the thermoacoustic core [14, 15]. Correspondingly, Chen et al. [11] found that the oscillating flow in a thermoacoustic engine is dominate by the diffusive vorticity at the stack ends where the majority of momentum is dissipated irreversibly. Moreover, Tsimpoukis et al. [16] stated that the nonlinear effect become more significant by the increase of the power of external forces on the flow.

Few attentions [17, 18] are given to the investigation of entropy generation accompanying the thermoacoustic conversion process inside a standing-wave thermoacoustic engine. While fewer efforts has been made for the minimization of those undesirable effects. To cite few, Kuzuu et al. [19] has numerically investigated the nonlinear flow behavior effect on the heat transfer through stacked plates thermoacoustic core. Results found denotes that nonlinearities are observed not just at the stack entries but also at the region where a high temperature gradient exist.

Accordingly, Migliorino et al. [20] identified the regions where major nonlinearities are localized in a standing-wave thermoacoustic device. They found that the main source of dissipation is the vortex shedding at the stack limits where appear the highest temperature gradient. The effect of viscous dissipation and heat heat transfer on the thermoacoustic efficiency has been investigated by Yanagimoto et al. [21]. In fact, they found that the sustained mean temperature gradient in the flow direction improve the conversion process as it amplifies the acoustic waves. Otherwise, Chen et al. [22] analyzed both theoretically and experimentally the effect of a one-dimensional SWTAE entries boundary conditions in term of onset temperature and frequency on the dynamic istabilities. They stated that thermoacoustic instabilities are observed when the temperature gradient around the core reaches the onset temperature. Moreover, energy losses inside the hot buffer and the resonator are stronger as the onset temperature increase. According to the same study, if the viscous and thermal dissipation provides important instabilities at the stack region the engine will be forced to work at the onset frequency.

The concept of entropy generation minimization in real thermal devices has been well discussed by Bejan et al. [23]. Their analyses was based on the importance of temperature gradient on the nonlinear heat transfer minimization. Further, Pan et al. [24] found that as the temperature difference between the stack limits becomes higher as the energy dissipated in term of entropy generation is important. As a solution, Ishikawa et al. [18] established the optimum surface area of heat exchangers in term of dimensionless geometrical parameters serving in the minimization of thermodynamic instabilities by the reduction of viscous dissipation and thermoacoustic losses. In another study, Ishikawa et al. [15] demonstrated that an increasing of stack plate spacing enhances the longitudinal temperature gradient and then generate more entropy. Therefore, based on the second law of thermodynamics, fundamental approaches are given to carefully determine the space distance between the stacked plates for minimum instabilities. Likewise, Shokouhmand et al. [25] investigated the optimum porosity serving to minimum entropy generation and thermodynamic imperfection in a channel partially filled with a porous matrix subject to a uniform heat flux. According to the above literature, the effect of stack material properties on heat transfer and entropy generation along a standing-wave engine has not yet been investigated completely then it needs to be more understanding. In effect, the thermo-viscous interaction at the engine core depend strongly on the thermophysical properties of the constructive material.

In this paper, a parametric study is carried out to minimize the nonlinear behavior and instabilities in order to optimize the engine efficiency. In the second section of this paper, a numerical description and mathematical formulation of the system is detailed. Then in the third section, the acoustic work production and entropy generation by a simple standing wave thermoacoustic engine are defined. The fourth section establish the method of lattice Boltzmann adopted for the resolution of the system with implementing the corresponding boundary conditions. Subsequently, a mesh grid independence test is drawn at the fifth section followed up by the code validation. In the next section, results and founds obtained by our in-house developed numerical code are provided. Particular attentions are given for the investigation of the friction factor f and Nusselt number Nu at the thermoacoustic porous core indicating the dependency of thermodynamic interaction between the flowing fluid parcels at the solid walls and the dimensionless geometrical parameters. Therefore, the influence of thermal and viscous features of stack material on the energy dissipation and thermal losses is evaluated. Finally, the entropy generation of the SWTAE is investigated by analyzing the heat leakage and dynamic instabilities through the standing-wave core and at the resonator walls.

3.2 Problem description

3.2.1 Physical model

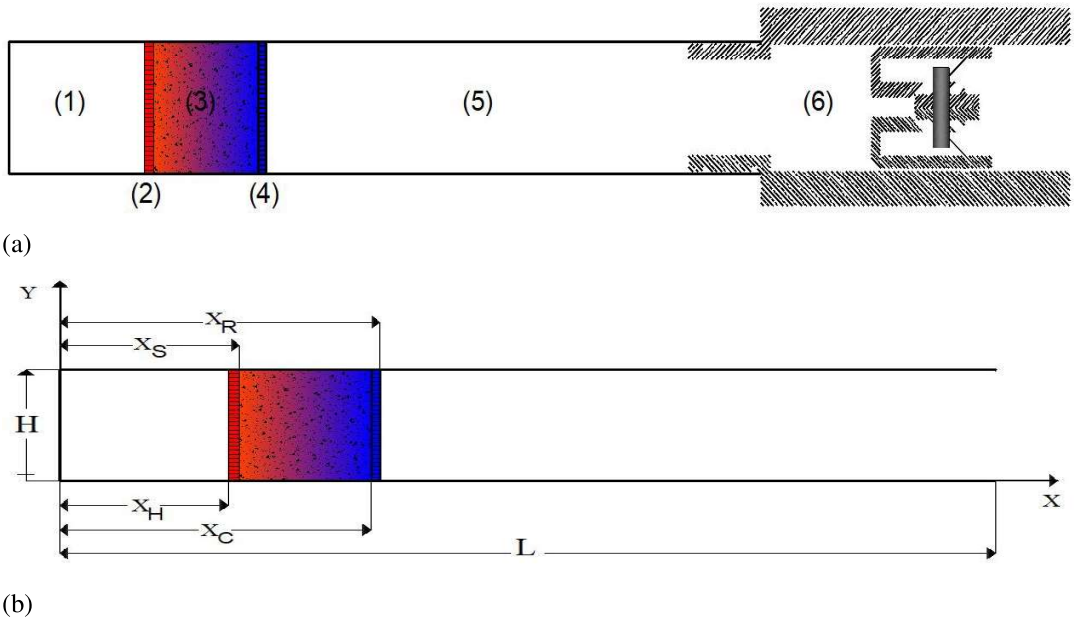

Figure 3.1: (a) Schematic drawing of the standing-wave thermoacoustic engine (b) The simulation domain

The standing-wave thermoacoustic engine (SWTAE) are considered very reliable and are long life devices further to the low requirement of maintenance and the lack of moving pieces. They consist of a thermal buffer, thermoacoustic core (TAC) and a resonator as shown in the Figure 3.1 (& Table 3.1). The TAC is composed of a porous medium (inner core) sandwiched between a hot and cold heat exchangers. Flowing from the hot side of the core, the heat absorbed from the hot exchanger is partly converted into acoustic work; it spontaneously oscillates until it falls to the cold side. The resulting acoustic waves can be therefore converted into electrical energy by means of electric generator such as alternator.

Component number	Description
(1)	Hot buffer
(2)	Hot exchanger
(3)	Inner-porous core
(4)	Cold exchanger
(5)	Resonator tube
(6)	Piston system

Table 3.1: Components of the standing wave thermoacoustic engine

Actual SWTAE (Figure 3.1. (b)) is made of a semi-closed thermoacoustic resonator of length L (= 1 meter) where the right end is open to a piston system. The hot exchanger (2), of length $(X_S - X_H)$, is situated at the left side of the TAC and is made of stainless steel with 50% porosity. The inner thermoacoustic core located at X_R from the left closed end is of $(X_C - X_S)$ length and constructed of a saturated, homogeneous and isotropic porous medium. The permeability and the degree of flow blockage inside the inner porous core is controlled by the porosity ε which ranges under $(\varepsilon \leq 0.6)$ for better heat transfer stability [26]. At the right side of the TAC (X_C) is placed a cold exchanger made of a Copper material with 50% porosity.

3.2.2 Mathematical formulation

The thermoacoustic engine is computed as a two-dimensional channel filled in part with a porous medium. The high speed of sound agree to low Mach number $(M_a < 0.3)$. In that case, the velocity varies slightly, so that the fluid is considered weak compressible. The natural

convective heat transfer caused by the temperature gradient around the TAC is neglected due to the fin width of the domain. The effect of viscosity is considered in this study while the effect of gravity is neglected due to the fin width of the domain. The flow is assumed to be laminar. The governing equations [27] are stated in the two-dimensional Cartesian coordinate (Figure 3.1 (b)).

Continuity equation

The microscopic governing conservation of mass equation in two-dimensional Cartesian coordinates is expressed as:

$$\nabla.\vec{U} = 0 \tag{3.1}$$

where $\vec{U}(U\vec{e_x} + V\vec{e_y})$ is the velocity vector of the fluid circulating through the system.

Momentum equation

Through the resonator, the momentum conservation equation is written as follow:

$$\frac{\partial \vec{U}}{\partial t} + (\vec{U}\nabla).\left((\frac{\Theta}{\varepsilon} + (1-\Theta))\vec{U}\right) = -\nabla\left((\Theta\varepsilon + (1-\Theta))\frac{P}{\rho_f}\right) + \mu_f\nabla^2\vec{U} - \Theta\varepsilon\left(\frac{\nu_f}{K} + \frac{F_\varepsilon}{\sqrt{K}}||\vec{U}||\right)\vec{U} \tag{3.2}$$

Θ is a binary number defining the existence of the porous medium. It is equal to 1 at the porous area and nil away. ε is the porosity of the engine core. ρ_f, P, μ_f and ν_f design respectively the fluid density, the pressure the dynamic and kinematic viscosities of the working fluid. The second term at the right side is the Brinkman term to depict viscous effects. The third term at the right side of the momentum expression is called the Darcy-Forchheimer term where the first part ($\frac{\nu_f}{K}\vec{U}$) account to the pressure drop into the system and the second term ($\frac{F_\varepsilon}{\sqrt{K}}||\vec{U}||\vec{U}$) is the Forchheimer drags caused by the nonlinear effect of the porous medium.
K and F_ε are the permeability of the porous core and the geometrical function expressed as:

$$K = \frac{\varepsilon^3 d^2}{150(1-\varepsilon)^2} \qquad F_\varepsilon = \frac{1.75}{\sqrt{150\varepsilon^3}} \tag{3.3}$$

d design the spherical pores mean diameter.

Energy equation

The dominating phenomena occurring between the engine limits are the heat conduction and heat convection appeared in the energy conservation equation as follow:

$$\left((1-\Theta)(C_p)_f+\Theta(C_p)_e\right)\frac{\partial T}{\partial t}+(C_p)_f(\vec{U}\nabla).T=\left((1-\Theta)k_f+\Theta k_e\right)\frac{\nabla^2 T}{\rho_f}+ \\ \Theta\varepsilon\left(\frac{\nu_f}{K}+\frac{F_\varepsilon}{\sqrt{K}}||\vec{U}||\right)||\vec{U}||^2+\nu_f\left(2((\frac{\partial U}{\partial X})^2+(\frac{\partial V}{\partial Y})^2)+(\frac{\partial U}{\partial Y}+\frac{\partial V}{\partial X})^2\right) \quad (3.4)$$

T is the temperature of the fluid and the subscripts e,s,f design respectively the effective, the solid and the fluid properties. The last term at the right side exhibit the effect of viscous dissipation.

The effective specific heat and thermal conductivity are calculated as follow:

$$(\rho C_p)_e=\varepsilon(\rho C_p)_f+(1-\varepsilon)(\rho C_p)_s \quad and \quad k_e=\varepsilon k_f+(1-\varepsilon)k_s \quad (3.5)$$

3.2.3 Initial and boundary conditions

The working gas is air initially set under standard atmosphere $P_o=P_{atm}$ and ambient temperature $T_o=T_{amb}$. The density of the gas is $\rho_0=1.184\ Kg/m^3$ and the dynamic viscosity is $\mu_f=1.849\ 10^-5\ Pa.s$ while Prandt is set equal to 0.71.

- Ambient temperature $(T_w=T_{amb})$ and non-slip boundary condition $(U=V=0)$ are applied at the external west, upper and bottom boundaries ($X=0$ and $0<Y<H$; $0<X<L$ and $\begin{cases} \text{Y=0} \\ \\ \text{Y=H} \end{cases}$;
- The outlet end of the engine $(X=L$ and $0<Y<H)$ is open to a power piston $(\partial U/\partial X=0;\ \partial V/\partial X=0)$ as can be seen in Figure 1. (a);
- The hot exchanger $(X_H<X<X_S$ and $0<Y<H)$ is set at temperature $T=T_H$;
- The cold exchanger $(X_C<X<X_R$ and $0<Y<H)$ is set at temperature $T=T_C$;
- The flow continuity at the solid- fluid interfaces $(X=X_H$ and $X=X_R$; $0<Y<H)$ is

ensured via the non-slip condition:

$$\vec{U}(X,t)_p = \vec{U}(X,t)_f \quad and \quad \frac{1}{\varepsilon} < \partial\vec{U}/\partial X|_p =< \partial\vec{U}/\partial X|_f \tag{3.6}$$

The heat flux continuity is expressed as:

$$T(X,t)_p = T(X,t)_f \quad and \quad k_e < \partial T/\partial X|_p = k_f < \partial T/\partial X|_f \tag{3.7}$$

3.3 Dimensionless problematic

The spatio-temporal domain under consideration is numerically discretized as:

$$x = \frac{X}{L} \qquad y = \frac{Y}{H} \qquad \tilde{t} = t\frac{U_{ref}}{H} \tag{3.8}$$

where L, H represent the real length and width of the geometry; X and Y are the coordinates in x-, y-,directions, respectively. U_{ref} is the reference velocity ($U_{ref} = \sqrt{\frac{2P_o}{\rho_{f_o}}}$, ρ_o is the fluid density at $t = 0s$.).

$$u = \frac{U}{U_{ref}} \qquad v = \frac{V}{U_{ref}} \qquad p = \frac{P}{\rho_f U_{ref}^2} \qquad \theta = \frac{T - T_C}{T_H - T_C} \tag{3.9}$$

For the non-dimensionalization of the above equations (1),(2),(4) the following dimensionless parameters are introduced:

$$Re = \frac{U_{ref}H}{\nu_f} \qquad E_c = \frac{U_{ref}^2}{C_p\Delta T} \qquad Da = \frac{K}{\varepsilon H^2} \qquad R_K = \varepsilon + (1-\varepsilon)\frac{k_s}{k_f} \quad and \quad R_K = \varepsilon + (1-\varepsilon)\frac{(\rho C_p)_s}{\rho_f C_p} \tag{3.10}$$

Subsequently, the governing equations at dimensionless form are written as:

$$\nabla.\vec{u} = 0 \tag{3.11}$$

$$\frac{\partial\vec{u}}{\partial\tilde{t}} + \vec{u}.\nabla.\left(\left(\frac{\Theta}{\varepsilon} + (1-\Theta)\right)\vec{u}\right) = -\nabla\left(\left(\Theta\varepsilon + (1-\Theta)\right)p\right) + \frac{1}{Re}\nabla^2\vec{u} - \Theta\varepsilon\left[\frac{1}{ReDa} + \frac{F_\varepsilon}{\sqrt{Da}}||\vec{u}||\right]\vec{u} \tag{3.12}$$

$$[1+\Theta(1-\varepsilon)(R_C-1)]\frac{\partial\theta}{\partial\tilde{t}}+(\vec{u}\nabla).(\theta)=(1+\Theta(1-\varepsilon)(R_K-1))\nabla^2\theta$$
$$+\Theta E_c(\frac{1}{ReDa}+\frac{\varepsilon F_\varepsilon}{\sqrt{Da}}||\vec{u}||)||\vec{u}||^2+\frac{E_c}{Re}[2((\frac{\partial u}{\partial x})^2+(\frac{\partial v}{\partial y})^2)+(\frac{\partial u}{\partial y}+\frac{\partial v}{\partial x})^2] \quad (3.13)$$

The boundary conditions corresponding to the above equations are:

- u=0; v=0 and $\theta=\theta_w$ for x=0 and $0<y<1$;
- u=0 ; v=0 and $\theta=\theta_w$ at $0<x<1$ and $\begin{cases}\text{y=0}\\ \\ \text{y=1}\end{cases}$;
- $\frac{\partial u}{\partial x}=0$; $\frac{\partial v}{\partial x}=0$ at x=1 and $0<y<1$;
- $\frac{\partial u}{\partial y}=0$; $v=0$ and $\theta=\theta_H$ at $x=x_S$ and $0<y<1$;
- $\frac{\partial u}{\partial y}=0$; $v=0$ and $\theta=\theta_C$ at $x=x_F$ and $0<y<1$;
- $u(x,t)_{/_f}=u(x,t)_{/_p}$ and $\frac{\partial u}{\partial x}_{/_f}=\frac{1}{\varepsilon}\frac{\partial u}{\partial x}_{/_p}$ at $0<y<1$ and $\begin{cases}\text{x=x}_H\\ \\ \text{x=x}_C\end{cases}$;
- $\theta_{/_f}=\theta_{/_p}\quad and\quad k_f\frac{\partial\theta}{\partial x}_{/_f}=k_e\frac{\partial\theta}{\partial x}_{/_p}$; at $0<y<1$ and $\begin{cases}\text{x=x}_H\\ \\ \text{x=x}_C\end{cases}$

3.4 Acoustic work and entropy generation

The time-averaged acoustic power generated ahead the cold end of the TAC is calculated by [28]:

$$W=\frac{1}{2}S|P||U|cos(\phi)\qquad(Watt) \quad (3.14)$$

where S design the cross-sectional area of the resonator tube. The phase difference ϕ between the pressure and velocity oscillations along the wave propagation direction. ϕ is close to 90 for standing-wave devices at the center of the porous core [29] as illustrated in the Figure 3.2.

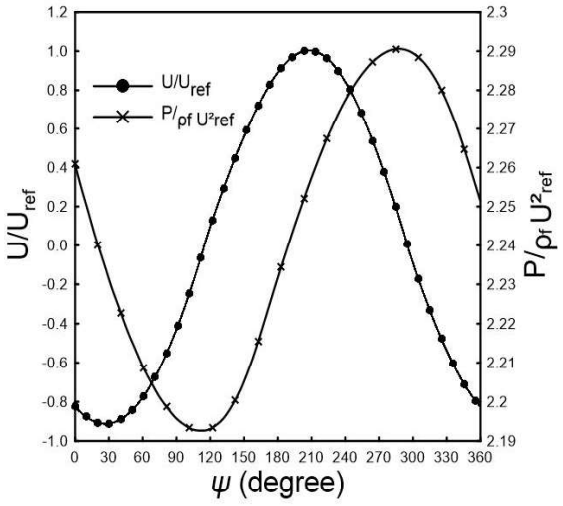

Figure 3.2: Phase variation of velocity and pressure at the TAC mid-section

The entropy generation in two-dimensional flow is expressed as follow [14, 15]:

$$N_s = HTI + FFI \tag{3.15}$$

Where

FFI is the fluid friction irreversibility; caused essentially by the viscous effect inside the channel and at the wall layers, written as follow:

$$FFI = \frac{\upsilon}{T_{moy}}\Phi \tag{3.16}$$

T_{moy} is the dimensionless average temperature and Φ is dimensionless viscous dissipation. HTI represent the amount of heat transfered irreversibility by the existence of temperature gradient and is expressed as:

$$HTI = \frac{R_k}{T_{moy}^2}\nabla {T_{moy}}^2 \tag{3.17}$$

The rate of irreversible heat transfer to the total entropy generation is called Bejan number defined as:

$$Be = \frac{HTI}{N_s} \tag{3.18}$$

To more understand the heat transfer activity through the engine core, an analysis of the heat transfer rate between the porous medium and the engine walls is examined in term of the nondimensional parameter Nusselt number.

The local Nusselt number along the TAC walls is calculated as [30]:

$$Nu = (\frac{Y_o}{T_w - T_b})\frac{\partial T}{\partial Y}_{/Y=Yo} \tag{3.19}$$

Then the average Nusselt number Nu_{av} is obtained by :

$$Nu_{av} = \frac{1}{T_w - T_b}\int_0^H \frac{\partial T}{\partial X}_{/Y=Yo} dY \tag{3.20}$$

3.5 Lattice Boltzmann method

The Lattice Boltzmann Method (LBM) is an efficiently way, compared to that of the traditional continuum Navier-Stokes method, in predicting flow and heat transfer characteristics in thermoacoustic devices. In fact, this method has been affirmed as an efficient method for the simulation of heat transfer and entropy generation in the porous medium. In the present study, a simple relaxation time Bhatnagar-Gross-Krook (BGK) scheme is adopted. Two-dimensional and nine directional speed square lattice model is designated for both thermal and flow field resolution. The lattice vectors arrangement for D2Q9 model are presented as in the Figure 3.3.

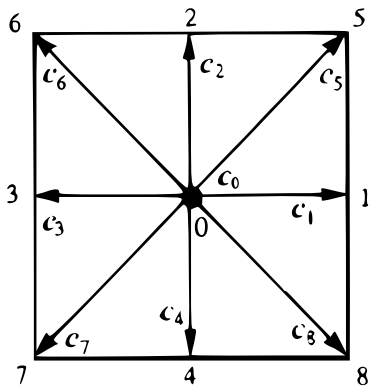

Figure 3.3: Lattice arrangement for two dimensional and nine directions problem

3.5.1 LBM equation for the velocity field

For the coupled thermal LBM model, the velocity evaluation equation is extracted from the mass and momentum conservation equations it is written as [31]:

$$f_i(x + c_i\Delta t, t + \Delta t) - f_i(x,t) = -\frac{\Delta t}{\tau_m}[f_i(x,t) - f_i^{eq}(x,t)] + \Delta t F_{ei} \tag{3.21}$$

τ_m is the momentum dimensionless relaxation time:

$$\tau_m = 3\nu\frac{\Delta t}{(\Delta x)^2} + 0.5 \tag{3.22}$$

f_i^{eq} is the equilibrium density distribution function, it takes the following form:

$$f_i^{eq} = \rho\omega_i[1 + \frac{c_i\vec{u}}{c_s^2} + \frac{(c_i\vec{u})^2}{2(\varepsilon\Theta + (1-\Theta))c_s^4} - \frac{\vec{u}^2}{2(\varepsilon\Theta + (1-\Theta))c_s^2}] \tag{3.23}$$

c_s is the discrete microscopic speed of a single particle equal to $\frac{1}{\sqrt{3}}$.
F_{ei} is the total body force written as:

$$F_{ei} = F\frac{(c_i - u)^2 f_i^{eq}}{RT_{ref}} \tag{3.24}$$

$F(= \varepsilon\left(\frac{1}{ReDa} + \frac{F_\varepsilon}{\sqrt{Da}}||\vec{u}||\right)\vec{u})$ is the total body force within the porous structure. The values at each lattice are respectively,$c_0(0,0)$, $c_1(1,0)$,$c_2(0,1)$, $c_3(-1,0)$, $c_4(0,-1)$, $c_5(1,1)$, $c_6(-1,1)$, $c_7(-1,-1)$ and $c_8(1,-1)$.
Then, the discrete density, velocity and pressure are calculated as:

$$\rho(x,t) = \sum_i f_i(x,t) \quad , \quad \tilde{\rho}(x,t)u(x,t) = \sum_i c_i f_i(x,t) + \frac{\Delta t}{2}\rho F_{ei} \quad , \quad p(x,t) = c_s^2\rho(x,t) \tag{3.25}$$

3.5.2 LBM equation for the heat field

The evolution of the heat field is simulate using the following equation [32]:

$$g_i(x + c_i\Delta t, t + \Delta t) - g_i(x,t) = -\frac{\Delta t}{(1-\Theta)\tau_s + \Theta\tau_{sm}}[g_i(x,t) - g_i^{eq}(x,t)] + \Delta t\phi \tag{3.26}$$

τ_s and τ_{sm} are the non-dimensional thermal relaxation time determining the nature of heat exchange between the gas particles and the solid surfaces respectively within the resonator and the porous core:

$$\tau_s = 3\frac{\Delta t}{(\Delta X)^2}\alpha + 0.5 \qquad \tau_{sm} = 3PrR_k\frac{(\tau_m - 0.5)}{R_c} + 0.5 \tag{3.27}$$

Pr, α are Prandt number and the thermal diffusivity coefficient.

ϕ is the viscous dissipation term written as:

$$\phi = \omega_i(1+\frac{\tau_{sm}-0.5}{\tau_{sm}}\frac{c_i u}{c_s^2})[E_c(\frac{1}{ReDa}+\frac{\varepsilon F_\varepsilon}{\sqrt{Da}}\mid u \mid)u^2+\frac{E_c}{Re}[2((\frac{du}{dx})^2+(\frac{dv}{dy})^2)+(\frac{du}{dy}+\frac{dv}{dx})^2] \tag{3.28}$$

The discrete internal energy equilibrium distribution function g_i^{eq} takes the following form:

$$g_i^{eq}(x,t) = \theta(x,t)\omega_i[1+\frac{c_i\vec{u}}{c^2}] \tag{3.29}$$

ω_i is the weigh coefficient of each lattice given by:

$$\omega_i = \begin{cases} \frac{4}{9} & i=0 \\ \frac{1}{9} & i=1,2,3,4 \\ \frac{1}{36} & i=5,6,7,8 \end{cases}$$

The discrete temperature can be calculate using the following equation:

$$\theta(x,t) = \sum_i g_i(x,t) \tag{3.30}$$

3.5.3 LBM Boundary conditions

The actual standing wave thermoacoustic engine is typically made of a resonator and a porous core inserted between hot and cold exchangers.

- Dynamic boundary condition

  Bounce-back boundary condition is applied at the external boundaries of the resonator:

  $f_1 = f_3 \quad f_5 = f_7 \quad f_8 = f_6$ for x=0 and $0 < y < 1$

  $f_2 = f_4 \quad f_5 = f_7 \quad f_6 = f_8$ for y=0 and $0 < x < 1$

  $f_4 = f_2 \quad f_7 = f_5 \quad f_8 = f_6$ for y=1 and $0 < x < 1$

  Zero order extrapolation open boundary condition is applied at the resonator end expressed as [33]:

  $$f_{1/n} = f_{1/n-1} \quad f_{5/n} = f_{5/n-1} \quad f_{8/n} = f_{8/n-1} \tag{3.31}$$

To ensure the continuity of the flow, non-slip condition is applied at the west and east sides ($x = x_S$ and $x = x_F$) of the porous core [34]:

$$f_{i/p} = f_{i/f} \tag{3.32}$$

where i denote the appropriate lattice index as illustrated in Figure 4.3 and p and f indicates respectively the porous and the fluid domain.

- Thermal boundary condition

  The external boundaries of the resonator are set isothermal at ambient temperature θ_w:

  $g_i = \theta_w(w_i + w_i^+) - g_i^+$ at $\begin{cases} \text{x=0 and } 0 < y < 1 \\ \text{y=0 and } 0 < x < 1 \\ \text{y=1 and } 0 < x < 1 \end{cases}$ i and i^+ are the indices corresponding lattices and their opposite.

  The temperature at the resonator end is treated by adopting the approach defined by Orazio et al. [35]. The incoming unknown population to the east end are supposed at equilibrium state at dimensionless temperature θ^{eq} defined as the temperature in a Dirichlet boundary.

  The corresponding unknown distribution functions at the outlet boundary are defined as:

$$\begin{aligned} \mathrm{g}_3 &= \tfrac{1}{9}\theta^{eq}(1 - \tfrac{3}{c^2}u) \\ \mathrm{g}_6 &= \tfrac{1}{36}\theta^{eq}(1 - \tfrac{3}{c^2}(u - v)) \\ \mathrm{g}_7 &= \tfrac{1}{36}\theta^{eq}(1 - \tfrac{3}{c^2}(u + v)) \end{aligned} \tag{3.33}$$

  θ^{eq} is calculated by:

$$\theta^{eq} = \frac{6(\theta_w - \theta_p)}{1 + \frac{3}{c^2}u} \tag{3.34}$$

θ_p is the sum of the known distribution functions coming from the adjacent internal wall nodes calculated as:

$$\theta_p = g_0 + g_2 + g_3 + g_4 + g_5 + g_8 \tag{3.35}$$

Then the unknown distributions of the outlet boundary are therefore calculated by:

$$g_i = \omega_i \theta^{eq} \tag{3.36}$$

A temperature gradient is applied at the TAC limits, a hot exchanger is placed at the west boundary ($x = x_S$) while an ambient heat exchanger is set at the opposite side ($x = x_F$). At the TAC entrance, the hot heat exchanger deliver a temperature θ_H from an external source such heat waste or a solar thermal collector.

$$\begin{aligned} g_3 &= \theta_H(w_3 + w_1) - g_1 \\ g_7 &= \theta_H(w_7 + w_5) - g_5 \\ g_6 &= \theta_H(w_6 + w_8) - g_8 \end{aligned} \tag{3.37}$$

At the other side, an ambient exchanger is placed maintaining the fluid at $\theta = \theta_C$.

$$\begin{aligned} g_1 &= \theta_C(w_1 + w_3) - g_3 \\ g_5 &= \theta_C(w_5 + w_7) - g_7 \\ g_8 &= \theta_C(w_8 + w_6) - g_6 \end{aligned} \tag{3.38}$$

The continuity at the fluid-solid interface of the porous core is defined as [34, 36] :

$$\theta_f = \theta_s \qquad and \qquad k_f \frac{\partial \theta}{\partial x} = k_s \frac{\partial \theta}{\partial x} \tag{3.39}$$

3.6 Validation

It should be noted that our in-house numerical code based on the BGK-TLBM was already validated [37]. To further validate the model, we consider the problem of an oscillating flow within a two-dimensional channel [38, 39]. The external walls of the deemed system are set isotherm at temperature T_w and the flow is driven by a periodic pressure gradient.

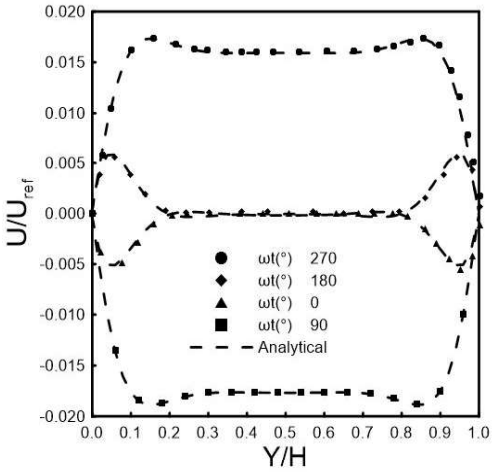

Figure 3.4: Development of velocity profile at the middle of the channel ($X = \frac{L}{2}, Y = \frac{H}{2}$)

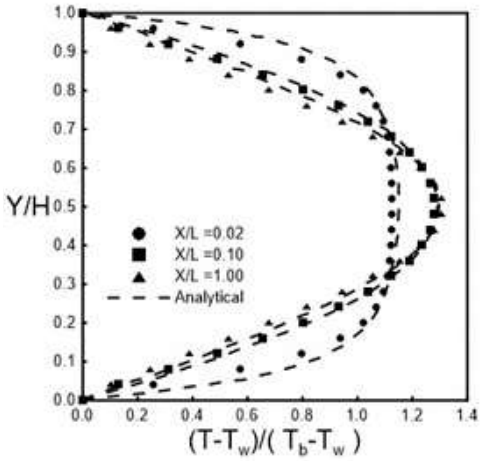

Figure 3.5: Mean temperature profile at three positions in the cross for the sections steady flow

Figure 3.4 reveals the velocity profile at the mid-channel ($X = \frac{L}{2}, Y = \frac{H}{2}$. At can be seen, the velocity at the centerline is closer to the minimum and always lower than the velocity nearby the upper and lower walls. The annular effect in the centerline is formed due to the presence of viscous dissipation phenomenon coupled by an important inertial force in the center of the channel. The provided instabilities are due to the existence of fluid friction near the walls.
Figure 3.5 depicts the evolution of the mean temperature profile $\theta_w = \frac{T_w - T_C}{T_H - T_C}$ [40] at three positions in the cross for the sections steady flow ($X/L = 0.02$;$X/L = 0.1$ and $X/L = 1$). The bulk temperature T_b express the evolution of temperature inside the channel compared to the wall temperature. As can be seen, the temperature profile is parabolic and uniform over all the flow. It is nil at the wall boundaries and maximal at the center of the channel. The flat profile at the engine entrance reflect the important interaction between the fluid layers and the channel walls. As observed, the profile become developed from the one-tenth length position and it maximal increase slightly from there.

3.7 Mesh independence test

Figure 3.6 exhibits the check of mesh independence test in terms of lengthwise velocity evolution in the X direction of the computed SWTAE at $Y = H/2$. To ensure simulation stability, five different mesh grids are evaluated (600X30, 800X40,1000X50, 1200X60, 1400X70) for $\varepsilon = 0.5$, $Re = 100$, $R_K = 3$, $R_C = 20$ and $Da = 0.001$.

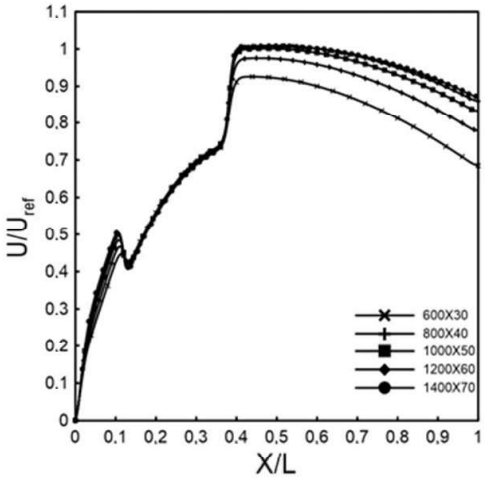

Figure 3.6: Mesh independence test of the lengthwise velocity evolution along the standing-wave engine at $H/2$ for $\varepsilon = 0.5$, $Re = 100$, $R_K = 3$, $R_C = 20$ and $Da = 0.001$

A quite small difference in the velocity evolution between the five grids is observed at the hot buffer. Then, inside the porous core, the flow become insensitive to the number of grid nodes. A remarkable difference between the chosen grids is observed in the simulation of the fluid flow at the TAC outlet region $X_R < X < L$. As can be seen, the acoustic velocity amplitude between (600X30) and (800X40) grid sizes has about 8.42% difference. Then, a deviation by about 2% between the mean velocity amplitude at the resonator tube is noted between the second (800X40) and third mesh (1000X50) grids while it is about 5.46% at the resonator end. Therefore, it is seen that the simulation become independent of the grid number nodes for a more refined grids. Lower than 2% of mean velocity difference is observed between (1000X50) and (1200X60) grids. Definitely, for more refined grids the acoustical velocity evolution profiles become identical. Eventually, for optimum computational time execution (1000X50) grid size is adopted in this work.

3.8 Result and discussion

In this section, we study the effect of the inner porous media parameters on the fluid flow and the heat transfer within the standing wave thermoacoustic engine core. The relevant parameters influencing the dynamic and thermal fields within the device are Reynolds number, Darcy number, the heat conductivity and heat capacity of the constructive material (viz,R_C and R_K). It should be recalled that the working gas is air with Prandt number $Pr = 0.71$ and the engine is computed as two dimentional semi-closed tube where the length ($L = 1meter$) is set sufficient

long to minimize losses [40] and end effects. The inner porous TAC has 50% porosity ($\varepsilon = 0.5$) where the temperature difference between its boundaries is set constant at ($T_H - T_C$)=80 °C.

3.8.1 Engine configuration

To ensure an efficient investigation, an expectation about the optimum configuration is elaborated. For the same porosity, seven different core lengths positioned at five positions along the first half of the resonator.

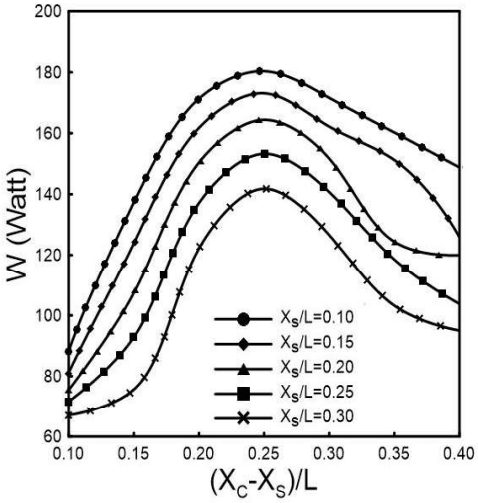

Figure 3.7: Effect of the TAC position ($\frac{X_S}{L}$) and length ($\frac{X_C - X_S}{L}$) on the thermoacoustic work with $\varepsilon = 0.5$, $Re = 400$, $R_K = 3$, $R_C = 20$ and $Da = 0.001$

Figure 3.7 exhibits simultaneously the effect of both TAC position ($\frac{X_S}{L}$) and length ($\frac{X_C - X_S}{L}$) on the standing wave thermoacoustic engine work generation for the following dimensionless parameters: $\varepsilon = 0.5$, $Re = 400$, $R_K = 3$, $R_C = 20$ and $Da = 0.001$. It is observed that through the different positions ($0.1 < X_S/L < 0.3$), the best acoustic production is obtained when the TAC is positioned at one-tenth wavelength distance from the pressure antinode.

Thus, the generated acoustic power is reduced as the distance of the TAC from the pressure antinode increase. Furthermore, when extending the TAC length ($\frac{X_C - X_S}{L} < 0.25$)) the temperature gradient around the TAC increase considerably, so that the conversion process slow down. Then, it can be concluded that the engine perform better for $L/4$ TAC length. The fluid parcel interaction becomes more important and the energy of the intermolecular collusion increase. Then, for more extended length ($(\frac{X_C - X_S}{L} < 0.25)$), the acoustic power generation decreases gradually due to the fact that the viscous losses at the porous core are linearly proportional to

the contact surface area.

For the rest of our study, the TAC is positioned near to the pressure antinode at $X_s = L/10$ and it has long ($\frac{X_C - X_S}{L} = 0.25$)).

3.8.2 Dynamic Field

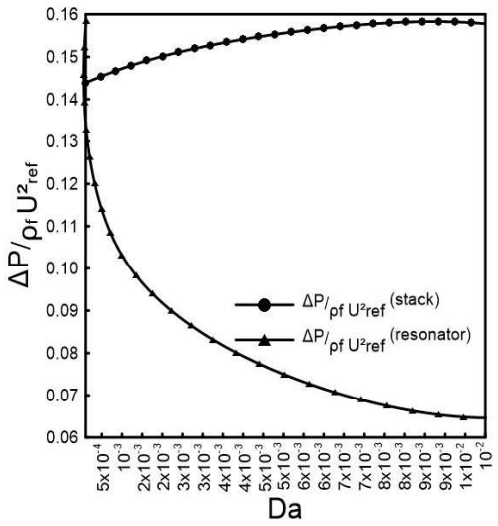

Figure 3.8: Maximum pressure difference between the TAC ends and resonator tube limits by Darcy number for $\varepsilon = 0.5$, $Re = 400$, $R_K = 3$, $R_C = 20$ at $Y = H/2$

Figure 3.8 illustrates the effect of Darcy number Darcy number on the pressure difference ($\frac{\Delta P}{\rho_f U_{ref}^2}$) between the porous inner-core ends ($X = X_S$ and $X = X_C$) and between the resonator tube limits ($X = 0$ and $X = L$) at $Y = H/2$ for $\varepsilon = 0.5$, $Re = 400$, $R_K = 3$, $R_C = 20$. As observed, the pressure difference between the TAC ends becomes more important at higher Da number. That can be explained by the importance of viscous resistance at low permeability inside the inner TAC. Inversely, ($\frac{P_L - P_0}{\rho_f U_{ref}^2}$)) between the resonator tube ends decrease by the increasing of Darcy number where P_L is pressure at $X = L$ and P_0 is the pressure nearby the closed end $X = 0$. Then, from the fact that best conversion can occurred at high pressure difference between TAC limits it can be concluded that the use of minor permeable core is not advised.

Figure 3.9 exhibits simultaneously the influence of both Darcy number and Reynolds number on the friction factor at the thermoacoustic core with porosity $\varepsilon = 0.5$ and for $R_K = 3$, $R_C = 20$. As illustrated, the decreasing of the porous medium permeability ensure most effective fluid frictions due to the enlargement of the contact area. Additionally, it can be seen that the friction factor is inversely proportional to Reynolds number. The influence of Reynolds number on the frictions at the porous TAC is clearly observed at low values. In fact, weaker flow enforce

the fluid shearing causing strong viscous forces. Then, as observed in the figure the influence become negligible by the increase of the permeability further to the decreasing of layer shearing and instabilities.

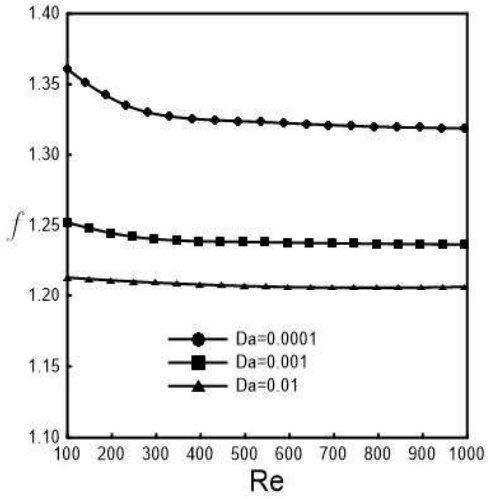

Figure 3.9: Maximum friction factor at the engine core versus Reynolds and Darcy number for $\varepsilon = 0.5$, $R_K = 3$, $R_C = 20$

Figures 3.10. (a) and (b) illustrates the dimensionless velocity profile of the acoustic wave respectively at the middle ($X = \frac{X_C + X_S}{2}$) and the outlet of the porous core ($X = X_R$). As observed in the Figure 3.10. (a), at the middle of the TAC, the acoustic velocity profile takes an annular form. It is nil at the solid walls due to the non-slip condition while a maximal value occurs at the neighboring layers and then attenuated at the center. The velocity overshoot near the walls is well known as the "Richardson effect", this phenomenon is widespread in the case of an oscillatory flow in a porous medium. That is explained by the existence of important viscous forces due to the intermolecular interaction nearby the porous core walls.

It is readily apparent that the amplitude of the centerline velocity is higher as the permeability of the TAC is low. Additionally, the annular effect becomes larger following the raising of the fluid shearing near the engine walls. In effect, the increasing of contact area ensures the acceleration of the fluid parcel motion and then result both significant frictions and larger acoustic waves over there. Although the overshooting gradient near the external walls slows down at feeble Darcy due to the weakness of the viscous dissipation at the wall layers.

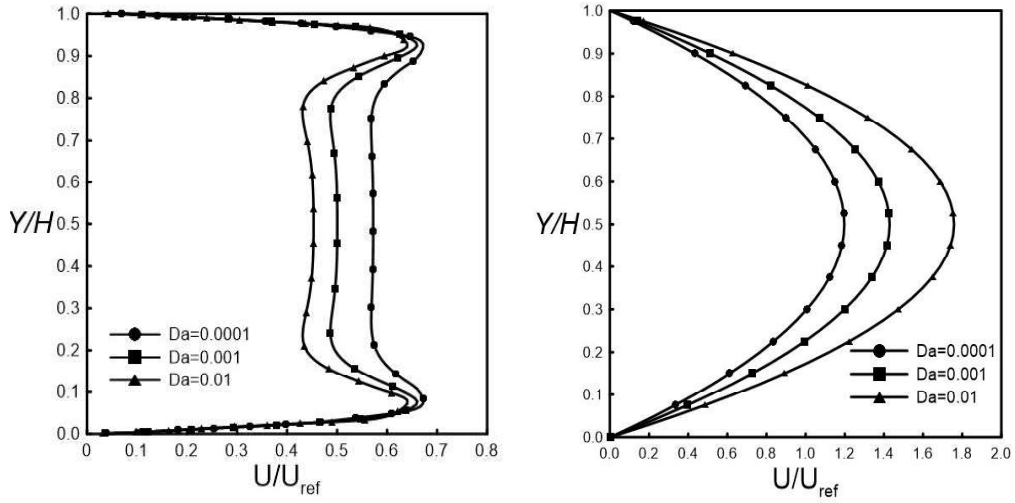

(a) (b)

Figure 3.10: Darcy number effect on the dimensionless acoustic velocity (a) at the center $\frac{X_C+X_S}{2}$) and (b) at the outlet of the TAC (X_R) for $\varepsilon = 0.5$, $Re = 400$, $R_K = 3$, $R_C = 20$

Besides, as illustrated in the Figure 3.10. (b), it is found that the velocity amplitude increases by the increase of Darcy number. This condition conduct to the minimization of nonlinear interaction at the TAC limits and then reduce perturbations as the thermodynamic irreversible process that subsequently implicate the production of greater acoustic waves.

3.8.3 Thermal field

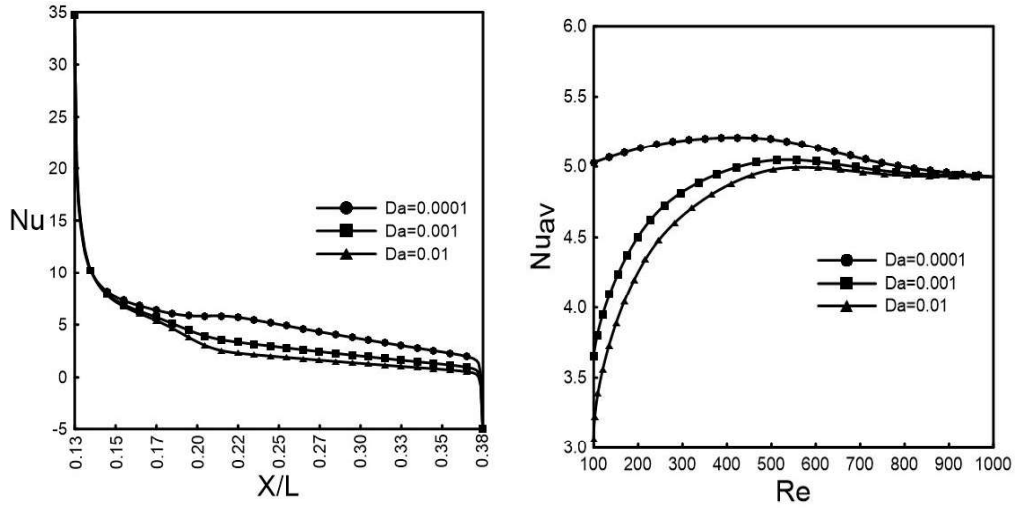

(a) (b)

Figure 3.11: (a) Variation of the local Nusselt number evolution at the TAC walls $(Y = H)$ with Da number (b) The average Nusselt number dependency on Re and Da for $\varepsilon = 0.5$, $R_K = 3$, $R_C = 20$

Figure 3.11. (a) outline the variation of the local Nusselt number Nu at the upper wall of the engine core $(Y = H)$ for $\varepsilon = 0.5$, $Re = 400$, $R_K = 3$, $R_C = 20$. Note that maximum heat transfer rate occurs at the hot side of the thermoacoustic core while it is minimum at the vicinity of cold heat exchanger. Major heat transfer rate is recorded at low Da values where the heat convection is significant and viscous dissipation becomes negligible which correspond to Darcy.Therefore, the dependency of the average Nusselt number on both Darcy number (Da) and flow pattern (Re) is plotted in the Figure 3.11. ((b). For high Re values $(Re > 800)$ the heat transfer rate depends slightly on Da number. It can be seen that Nu_av converge towards a constant value indicating the domination of heat convection. For $(Re < 800)$, it is seen that the decrease of Da number leads an important evolution of Nu_av principally caused by the enlargement of exchange area within the porous inner-core.

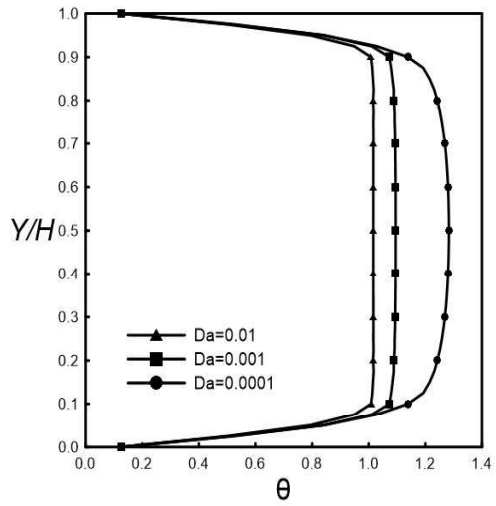

Figure 3.12: Darcy number effect on the temperature at the west side of the porous core $(X = X_S + \delta X)$ for $\varepsilon = 0.5$, $R_C = 10$ $R_K = 1$ and $Re = 400$

As the Figure 3.12 illustrates the effect of Da number on temperature profile nearby the hot exchanger $(X = X_S + \delta X)$. The temperature at the upper and lower walls is $\theta = \theta_w$ then it takes a nearly constant amplitude that increase with the decrease of inner-core permeability. In effect, viscous frictions within the porous structure delivers an additional heat to the working gas. Consequently, the increase of temperature amplitude is mainly explained by the importance of thermo-viscous interaction effect at higher contact area between the operating fluid particles and the solid walls of the TAC especially at the hot side. Indeed, the temperature increasing within the porous core slows down the particles motion which serve to provide weaker acoustic waves amplitude at the engine outlet as mentioned in Figure 3.10. (b).

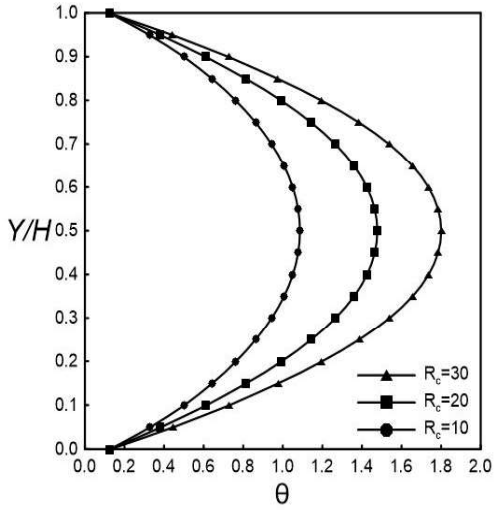

Figure 3.13: Capacity ratio effect on the temperature at the mid-core($X = (X_S + X_C)/2$) for $\varepsilon = 0.5$ $R_k = 1$ $Re = 400$

Figure 3.13 outlines the variation of temperature profile with the heat capacity ratio R_C at the midcore $(X = (X_S + X_C)/2)$ for $\varepsilon = 0.5$ $R_k = 1$ $Re = 400$. As shown, the temperature profile at the center of the inner porous core is parabolic where its amplitude is higher as the capacity ratio (R_C) increase. The effect of the porous material heat capacity weakens at low values so that the flow behaviors affect more in the mean temperature inside the engine. More precisely, the temperature gradient at the porous core become larger when the heat capacity of the used material is higher. In fact, the rate of heat transfer between the TAC borders must be smaller to decrease the instabilities and to be close to reversible thermoacoustic engines conditions. Eventually, low heat capacity materials are very reliable to such converter devices.

Figure 3.14 reveals the effect of the conductivity ratio R_K on the temperature distribution within the standing-wave thermoacoustic engine for $\varepsilon = 0.5$ $R_c = 10$ $Re = 400$. It can be seen that the conductivity of the porous material has great effect on the heat transfer within the porous core and on the temperature at the end of the resonator tube. The increasing of the ratio of the porous material and working fluid conductivities reduce the effect of thermo-viscous interaction within the core. Precisely, the additional heat produced inside the core becomes insignificant (Figure 3.14 (b)) causing therefore minor non-linear heat transfer between porous core limits. In essence, increasing of the constructive material conductivity decrease the conductive heat losses. However, at low values, the heat transfer becomes uncontrollable and provide strong harmonics due to the enlargement of the longitudinal temperature gradient.

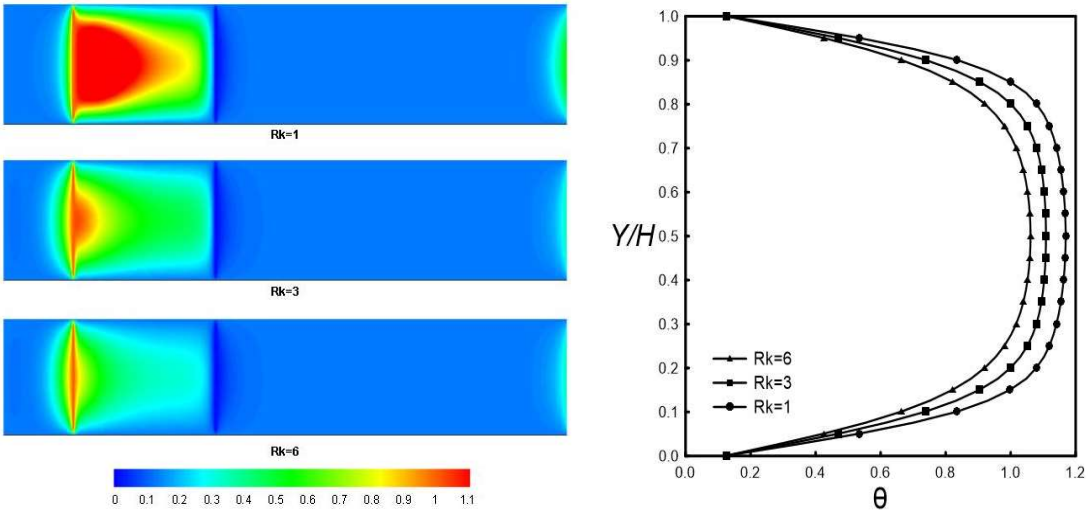

(a) (b)

Figure 3.14: Conductivity ratio effect on (a) the heat transfer and end effect within the SWTAE (b) and the temperature profile within west side of the core (X_S) for $\varepsilon = 0.5$ $R_c = 10$ $Re = 400$

Additionally, the temperature at the engine end is more affected. An important temperature increasing is observed at the resonator open end. This can be explained by the creation of vortex at the outlet end result of the nonlinear perturbations. Therefore, it can be conclude that for $R_K = 3$ the temperature at the TAC has minor instabilities and the linear interpolation between the hot and cold exchanger were perfect. That value of conductivity ratio correspond better to most adequate conversion operator.

3.8.4 Entropy generation

Except the thermoacoustic conversion, several irreversible processes are provided by the interaction of fluid parcel at the walls of the porous TAC. In effect, heat transfer and fluid frictions through a porous media subject to temperature gradient induces the entropy generation. The thermal-to acoustic efficiency of a thermoacoustic system is widely retarded by the generation of entropy. Typically, each form of energy conversion must be arranged so that the entropy generation although should be minimum. Therefore, operating under conditions close to those of reversible devices is interesting for standing-wave engine, looking for the improvement of the acoustic production with low cost. In this work, the determination of the entropy generation by the system serves to analyze the performance and the acoustic losses thus to propose the optimization procedure. Then, the suitable inner thermoacoustic core material features and structure are examined for the minimization of nonlinear behaviors through the standing-wave

engine.

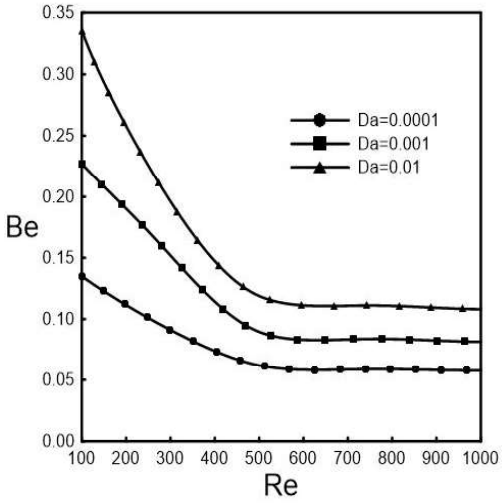

Figure 3.15: Bejan number dependency on Re and Da for $\varepsilon = 0.5$, $R_K =$ and $R_C =$ at the mid-core $(X = (X_S + X_C)/2, Y = H/2)$

Figure 3.15 illustrates the effect of Re number for three values of Da on Bejan (Be) at the middle of the inner thermoacoustic core $(X = (X_S + X_C)/2, Y = H/2)$. This investigation were carried out for the relevant parameters $\varepsilon = 0.5$, $R_K =$ and $R_C =$. Our study reveal that fluid friction irreversibility (FFI) dominate in the irreversible process for the tested values of Da and $100 < Re < 1000$ due to the importance viscous interaction within the porous structure.

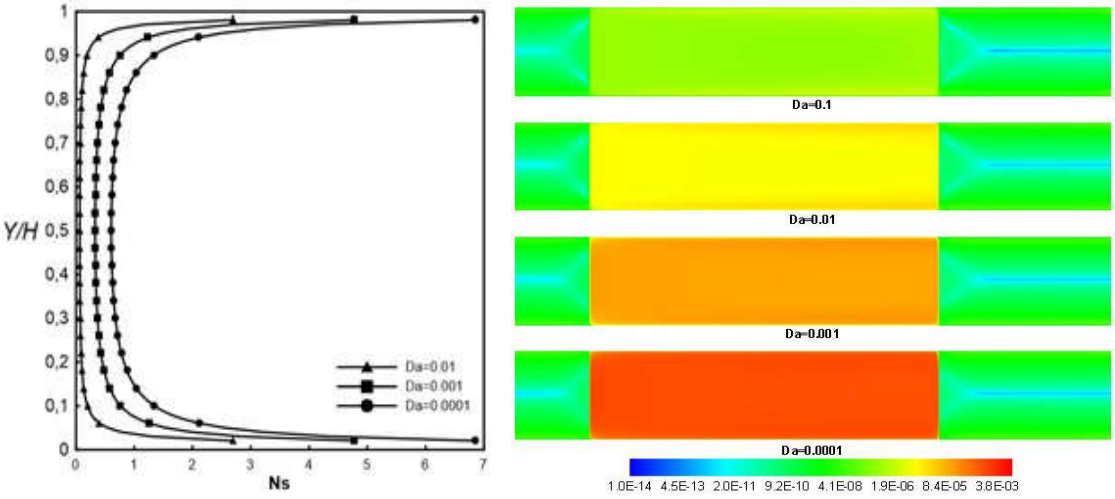

(a) (b)

Figure 3.16: Influence of Darcy number on (a) the entropy generation at the middle of a standing-wave thermoacoustic core $X = ((X_S + X_C)/2)$ (b) Fluid Friction contribution through and around the thermoacoustic core for $\varepsilon = 0.5$, $Re = 400$, $R_K = 3$ and $R_C = 20$

It can be clearly observed that Bejan is minimal for lower Darcy number value. That can be explained by the enhancement of fluid friction irreversibility by reducing the media's permeability. Besides, Bejan is weaken sharply by the increase of Re. The impact of heat transfer irreversibility (HTI) is more important at weak flow. In effect, the thermal interaction between the fluid parcels and the solid walls augment at low Re number. Then, for more powerful flow the effect of viscous frictions dominates the irreversible process which express the insignificance of thermal losses compared to viscous losses.

The influence of Darcy number on the entropy generation (Ns) and on the fluid friction contribution within the thermoacoustic core is presented in Figure 3.16 for $\varepsilon = 0.5$, $Re = 400$, $R_K = 3$ and $R_C = 20$. As can be seen in (Figure 3.16 (a)), the entropy generation is maximal at the walls layer where thermal losses and viscous dissipation are maximum. Those losses are linked to the acoustic energy losses crossing the channel section and then minimizing the ability of the system to convert the heat to the acoustic energy. The degree of molecular activities inside the porous core become important by the decreasing of Da which improve the increase of Ns. In Figure 3.16 (b), it can be seen that fluid friction irreversibility is important as Da is feeble. In effect, fluid layers shearing are intensified at low permeability. Therefore, acoustic losses and instabilities are remained greater. As observed, the irreversibility appear at the porous medium and at the vicinity of the resonator walls where fluid layers interaction are most important. Away from the TAC, higher entropy generation occur near the resonator walls then it diminishes monotonically to the inner flow.

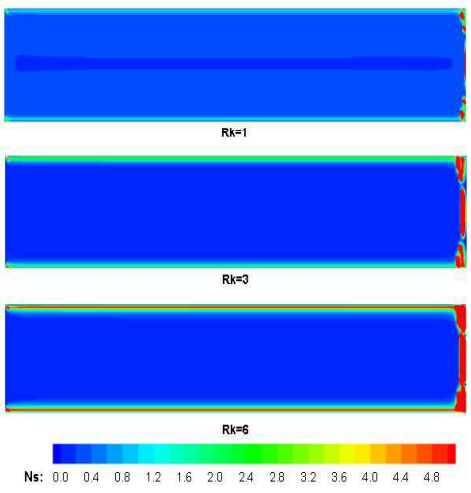

Figure 3.17: Entropy generation variation with the Conductivity ratio R_K for $\varepsilon = 0.5$,$Re = 400$, $Da = 0.001$ and $R_c = 35$

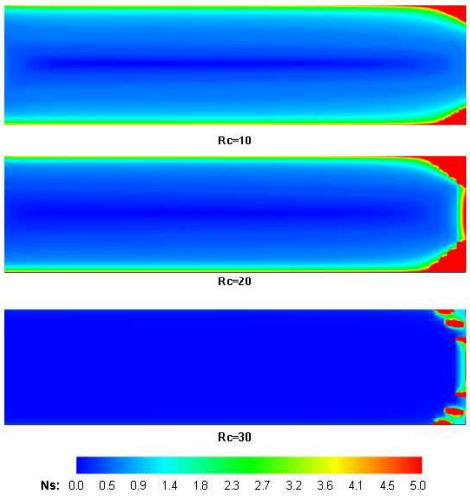

Figure 3.18: Entropy generation variation with the Capacity ratio R_C for $\varepsilon = 0.5$,$Re = 400$, $Da = 0.001$ and $R_K = 6$

Figure 3.17 illustrates the influence of conductivity ratio R_K on the entropy generation within the TAC ($X_S < X < X_C$) for $\varepsilon = 0.5$,$Re = 400$, $Da = 0.001$ and $R_c = 35$. As can be seen, the entropy generation has its maximal value at the cold side and is considerable at the external walls. In essence, heat leakage is maximal nearby the cold exchanger where exist significant thermal losses. Then, those losses are important as the thermal conductivity of the constructive material is higher. At high R_K, heat losses from the resonator walls increase providing high heat transfer irreversibility. Meanwhile, thermo-viscous interaction at middle of the TAC are calmed down at higher R_K value where minor entropy is observed.
Figure 3.18 exhibits the impact of the heat capacity ratio on the entropy contribution within the thermoacoustic core for the relevant parameters $\varepsilon = 0.5$,$Re = 400$, $Da = 0.001$ and $R_K = 6$. For lower value, the entropy generation within the porous matrix is more important due to the increase of heat transfer resistance. Furthermore, the heat losses from the external walls become larger caused by an important. Then, the heat transfer nearby the cold exchanger enhance. In effect, in this condition the rate of heat transfer between the core borders must be smaller to decrease the instabilities and to be close to reversible thermoacoustic engines conditions.

3.9 Conclusion

In this study, lattice Boltzmann method is applied to investigate the flow field and heat transfer through a thermoacoustic engine. The standing wave thermoacoustic engine is computed as a two dimensional tube occupied in part with a porous structre submitted to a temperature difference. Optimum porous core position and length giving maximum acoustic production were firstly studied. Then, for different porous core parameters, the thermodynamic flow behavior and on the entropy generation was investigated. Results found serves on the minimization of irreversible process by the insertion of a corresponding porous material.
As a conclusion, it is found that:

- At low Darcy number, minimal acoustic velocity is observed at the engine outlet due to the great frictions and heat transfer nonlinearities occurred through the TAC. A rather important entropy is observed at the porous core, in essence the acoustic wave generation become accompanied by an unstable fluid fluctuation.

- Minor heat transfer instabilities are obtained for a constructive material having reasonable high thermal conductivity and low heat capacity. Such material utilization leads to

the minimization of heat transfer irreversibilities at the porous core ends and it serves in the suppression of the end effects.

- The entropy generated by the thermoacoustic engine is mainly influenced by the temperature gradient at the external walls and the TAC boundaries and it is dominated by viscous frictions irreversibilities at the porous medium. In essence, maximum irreversibilities are observed at the cold region where important heat losses are occurred.

- The standing-wave engine operate at conditions closer to them of a reversible device if the porous core material is more thermal conductive and has lower heat capacity. Those conditions serves on the minimization of heat accumulation and temperature gradient improvement at the core boundaries.

Bibliography

[1] Kees De Blok. Low operating temperature integral thermo acoustic devices for solar cooling and waste heat recovery. *Journal of the Acoustical Society of America*, 123(5):3541–3541, 2008.

[2] S Zhang, ZH Wu, RD Zhao, GY Yu, W Dai, and EC Luo. Study on a basic unit of a double-acting thermoacoustic heat engine used for dish solar power. *Energy conversion and management*, 85:718–726, 2014.

[3] J-A Mumith, C Makatsoris, and TG Karayiannis. Design of a thermoacoustic heat engine for low temperature waste heat recovery in food manufacturing: A thermoacoustic device for heat recovery. *Applied Thermal Engineering*, 65(1-2):588–596, 2014.

[4] MEH Tijani and S Spoelstra. A hot air driven thermoacoustic-stirling engine. *Applied thermal engineering*, 61(2):866–870, 2013.

[5] Orest G Symko. Acoustic approach to thermal management: miniature thermo acoustic engines. In *Thermal and Thermomechanical Proceedings 10th Intersociety Conference on Phenomena in Electronics Systems, 2006. ITHERM 2006.*, pages 6–pp. IEEE, 2006.

[6] Chao Shen, Yaling He, Yuguang Li, Hanbing Ke, Dongwei Zhang, and Yingwen Liu. Performance of solar powered thermoacoustic engine at different tilted angles. *Applied Thermal Engineering*, 29(13):2745–2756, 2009.

[7] Limin Qiu, Bo Wang, Daming Sun, Yu Liu, and Ted Steiner. A thermoacoustic engine capable of utilizing multi-temperature heat sources. *Energy conversion and management*, 50(12):3187–3192, 2009.

[8] Nikolaus Rott. Thermoacoustics. In *Advances in applied mechanics*, volume 20, pages 135–175. Elsevier, 1980.

[9] Arganthaël Berson, Marc Michard, and Philippe Blanc-Benon. Measurement of acoustic velocity in the stack of a thermoacoustic refrigerator using particle image velocimetry. *Heat and Mass Transfer*, 44(8):1015–1023, 2008.

[10] Scott Backhaus and Greg W Swift. A thermoacoustic-stirling heat engine: Detailed study. *The Journal of the Acoustical Society of America*, 107(6):3148–3166, 2000.

[11] Geng Chen, Yufan Wang, Lihua Tang, Kai Wang, and Zhibin Yu. Large eddy simulation of thermally induced oscillatory flow in a thermoacoustic engine. *Applied Energy*, 276:115458, 2020.

[12] GW Swift. Analysis and performance of a large thermoacoustic engine. *The Journal of the Acoustical Society of America*, 92(3):1551–1563, 1992.

[13] Yuki Ueda and Chisachi Kato. Stability analysis of thermally induced spontaneous gas oscillations in straight and looped tubes. *The Journal of the Acoustical Society of America*, 124(2):851–858, 2008.

[14] Shohel Mahmud and Roydon Andrew Fraser. Flow, thermal, and entropy generation characteristics inside a porous channel with viscous dissipation. *International Journal of Thermal Sciences*, 44(1):21–32, 2005.

[15] Haruko Ishikawa and David J Mee. Numerical investigations of flow and energy fields near a thermoacoustic couple. *The Journal of the Acoustical Society of America*, 111(2):831–839, 2002.

[16] A Tsimpoukis, N Vasileiadis, G Tatsios, and D Valougeorgis. Nonlinear oscillatory fully-developed rarefied gas flow in plane geometry. *Physics of Fluids*, 31(6):067108, 2019.

[17] Tang Ke, Lin Xiaogang, Lei Tian, and Jin Tao. Study on self-excited oscillation in a thermoacoustic engine with glansdorffprigogine stability criterion. *Journal of Non-Equilibrium Thermodynamics*, 36(4):393–404, 2011.

[18] H Ishikawa and PA Hobson. Optimisation of heat exchanger design in a thermoacoustic engine using a second law analysis. *International Communications in Heat and Mass Transfer*, 23(3):325–334, 1996.

[19] Kazuto Kuzuu and Shinya Hasegawa. Effect of non-linear flow behavior on heat transfer in a thermoacoustic engine core. *International Journal of Heat and Mass Transfer*, 108:1591–1601, 2017.

[20] Mario Tindaro Migliorino and Carlo Scalo. Real-fluid effects on standing-wave thermoacoustic instability. *Journal of Fluid Mechanics*, 883, 2020.

[21] Kohei Yanagimoto, Shin-ichi Sakamoto, Yosuke Nakano, Kentaro Kuroda, and Yoshiaki Watanabe. Multistage stack with multiple pore radii applying the temperature gradient to a thermoacoustic engine. *Journal of Energy and Power Engineering*, 7(8), 2013.

[22] Geng Chen, Lihua Tang, and Brian R Mace. Theoretical and experimental investigation of the dynamic behaviour of a standing-wave thermoacoustic engine with various boundary conditions. *International Journal of Heat and Mass Transfer*, 123:367–381, 2018.

[23] Adrian Bejan. Entropy generation minimization: The new thermodynamics of finite-size devices and finite-time processes. *Journal of Applied Physics*, 79(3):1191–1218, 1996.

[24] Na Pan, Shuangfeng Wang, and Chao Shen. Visualization investigation of the flow and heat transfer in thermoacoustic engine driven by loudspeaker. *International journal of heat and mass transfer*, 55(25-26):7737–7746, 2012.

[25] Hossein Shokouhmand, Fereidoun Jam, and Mohammad Reza Salimpour. Optimal porosity in an air heater conduit filled with a porous matrix. *Heat transfer engineering*, 30(5):375–382, 2009.

[26] Wigdan Kisha, Paul H Riley, Jon McKechinie, and David Hann. The influence of heat input ratio on electrical power output of a dual-core travelling-wave thermoacoustic engine. 2018.

[27] Oumayma Miled, Hacen Dhahri, and Abdallah Mhimid. Numerical investigation of porous stack for a solar-powered thermoacoustic refrigerator. *Advances in Mechanical Engineering*, 12(6):1687814020930843, 2020.

[28] Tianjiao Bi, Zhanghua Wu, Limin Zhang, Guoyao Yu, Ercang Luo, and Wei Dai. Development of a 5 kw traveling-wave thermoacoustic electric generator. *Applied energy*, 185:1355–1361, 2017.

[29] Tetsushi Biwa, Yusuke Tashiro, Uichiro Mizutani, Motoki Kozuka, and Taichi Yazaki. Experimental demonstration of thermoacoustic energy conversion in a resonator. *Physical Review E*, 69(6):066304, 2004.

[30] Syeda Humaira Tasnim, Shohel Mahmud, and Roydon Andrew Fraser. Modeling and analysis of flow, thermal, and energy fields within stacks of thermoacoustic engines filled with porous media. *Heat transfer engineering*, 34(1):84–97, 2013.

[31] Y Wang, YL He, GH Tang, and WQ Tao. Simulation of two-dimensional oscillating flow using the lattice boltzmann method. *International Journal of Modern Physics C*, 17(05):615–630, 2006.

[32] Bayssain Amami, Hacen Dhahri, and Abdallah Mhimid. Viscous dissipation effects on heat transfer, energy storage, and entropy generation for fluid flow in a porous channel submitted to a uniform magnetic field. *Journal of Porous Media*, 17(10), 2014.

[33] Lakshmi Nizampatnam, Klaus Hoffmann, Michael Papadakis, and Ramesh Agarwal. Investigation of boundary conditions for computational aeroacoustics. In *37th Aerospace Sciences Meeting and Exhibit*, page 357, 1999.

[34] Jinku Wang, Moran Wang, and Zhixin Li. A lattice boltzmann algorithm for fluid-solid conjugate heat transfer. *International journal of thermal sciences*, 46(3):228–234, 2007.

[35] Annunziata D'Orazio, Massimo Corcione, and Gian Piero Celata. Application to natural convection enclosed flows of a lattice boltzmann bgk model coupled with a general purpose thermal boundary condition. *International Journal of Thermal Sciences*, 43(6):575–586, 2004.

[36] A Piccolo and G Pistone. Computation of the time-averaged temperature fields and energy fluxes in a thermally isolated thermoacoustic stack at low acoustic mach numbers. *International Journal of Thermal Sciences*, 46(3):235–244, 2007.

[37] Sahar Slimene, Abir Yahya, Hacen Dhahri, and Hassane Naji. Simulating rayleigh streaming and heat transfer in a standing-wave thermoacoustic engine via a thermal lattice boltzmann method. *International Journal of Thermophysics*, 43(7):1–30, 2022.

[38] Zhaoli Guo and TS Zhao. Lattice boltzmann model for incompressible flows through porous media. *Physical review E*, 66(3):036304, 2002.

[39] GH Tang, WQ Tao, and YL He. Simulation of fluid flow and heat transfer in a plane channel using the lattice boltzmann method. *International Journal of Modern Physics B*, 17(01n02):183–187, 2003.

[40] Qunte Dai and Luwei Yang. Lbm numerical study on oscillating flow and heat transfer in porous media. *Applied thermal engineering*, 54(1):16–25, 2013.

Chapter 4

Simulating Rayleigh streaming and heat transfer in a standing-wave thermoacoustic engine

4.1 Introduction

Thermoacoustic engines (TAEs) are heat engines where self-sustaining acoustic waves appear through gradient temperature application along a porous open cell medium (or stack) placed inside an acoustic resonator. Simply put, within these devices, the thermoacoustic effects are based on heat transfer interactions between a gas subjected to an acoustic excitation and a porous medium (or a stack as the case may be) where a temperature gradient is set in the propagation direction of acoustic waves. These devices can be classified into standing wave (SW) or travelling wave systems depending on the acoustic wave kind generated (see Figure 4.1b for illustrative purposes). They are mainly intended to combine thermal and acoustic interaction and recover energy. Explicitly, they can either consume acoustic work to ensure heat transfer, or produce acoustic work from thermal energy, which in turn can be converted to mechanical or electrical power. They may be a promising approach to recover heat such as geothermal energy [1–3], industrial waste heat [4, 5], solar thermal energy [6] and exhaust heat from internal combustion engines [7]. In addition, they are an attractive alternative for harnessing low quality heat using little or no moving components and environmentally friendly working fluids (e.g. inert gases or noble). They can become thermo-acoustically unstable beyond a critical heat input. Besides the efficiency of thermoacoustic conversion at low temperature gradient around the TAC [8], thermoacoustic technology remains a fairly promising technique in low grade thermal energy [9], to name a few. This low gradient heat recovery has become technically safe by preferably using thermoacoustic systems such as TAEs for power generation. Thereby, the approach based mainly on acoustic waves effect on heat exchange and vice versa from different points of view has long since become a major research issue. In addition, thermoacoustic technology is of potential interest for the green energy production, the industrial waste and heat waste recovery.

In the present paragraph, some relevant experimental studies conducted on TAEs are reported. Both experimental [10, 11] and numerical [12] studies have reported that the reduction in onset temperature to less than 80 °C under wet conditions for low quality waste heat recovery was enabled. Moreover, studies [13–15] have dealt with the influence of geometric characteristics on low-grade heat conversion. Nakamura [16] succeeded in achieving a Carnot efficiency of 8% for a standing wave thermoacoustic engine (SWTAE) operating under low heat conditions by varying the length, position and permeability of the stack at a temperature gradient beyond

180 °C. To predict the temperature and the instability frequency occurrence, Chen et al. [17] investigated the dynamic behavior of a one-dimensional self-excited standing wave thermo-acoustics with various boundary conditions at the ends through simple acoustic analysis and/or linear thermoacoustic theory.

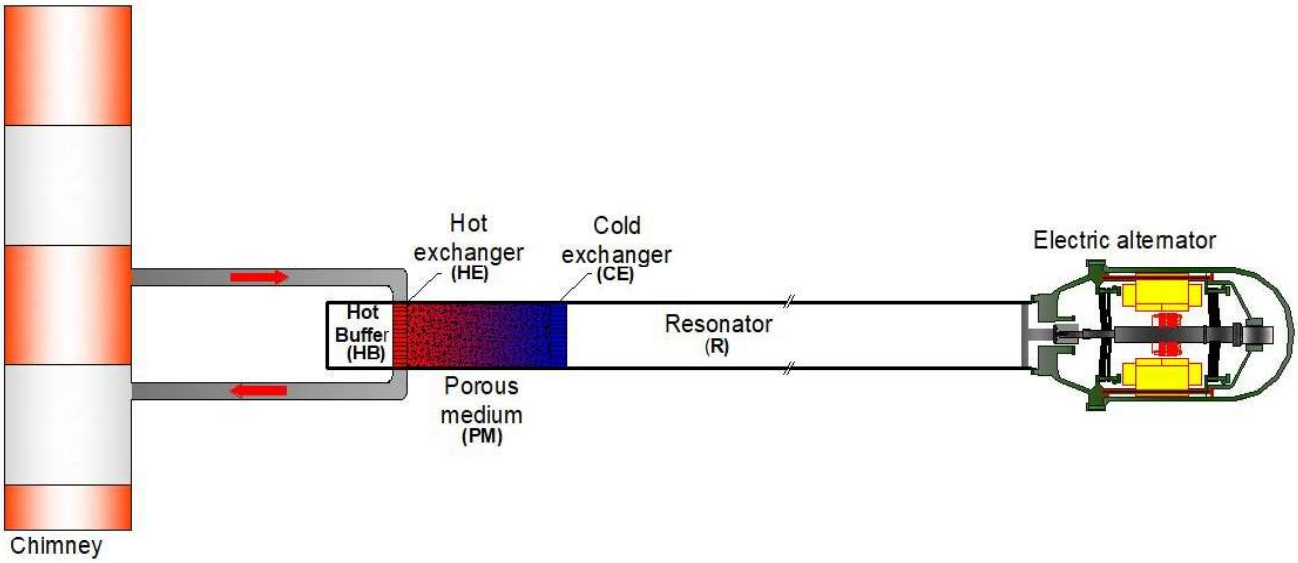

(a)

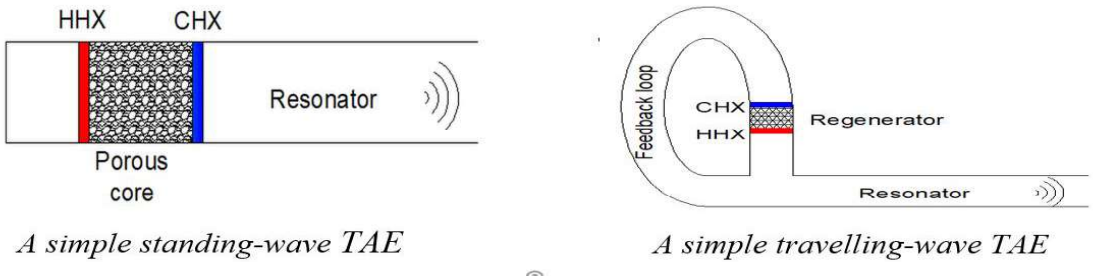

A simple standing-wave TAE *A simple travelling-wave TAE*

(b)

(c)

Figure 4.1: (a) Standing wave thermoacoustic engine with different parts and concept illustration sketch focus (b) standing and travelling wave devices (c) simulation domain

In thermoacoustic devices, the TAC is the key part for the thermoacoustic conversion. Its operation involves the thermal energy conduction perpendicular to that of the generated sound wave. Thereby, its manufacturing material choice is of paramount importance. The most used materials are ceramic and stainless steel which have good performance in energy conversion. Tijani et al. [18] designed a thermoacoustic Stirling heat engine whose stack consists of stainless steel screens. According to these authors, the performance achieved was 49% of the efficacy of Carnot. Ramadan et al. [19] experimentally investigated end-effects and natural convection effects on Rayleigh streaming pattern in a simple SWTAE with a ceramic stack. They found that the average velocity pattern changes in regions of cold flow, hot flow, and end effects while being or not in agreement with Rayleigh streaming. Jung and Matveev [20] reported on experimental and modelling results obtained with a small-scale SWTAE equipped with a glassy carbon stack. They stated that the efficiency of the device is reduced due to large hysteresis effects.

Sharify and Hasegawa [21] experimentally investigated a travelling wave thermoacoustic refrigerator driven by a multistage travelling wave thermoacoustic engine (TAE). Tijani [22] has shown experimentally that reducing the Prandtl number (Pr) to 0.2 allows for a coefficient of performance up to 70% greater than that with pure helium (Pr = 0.7). Long before, Tasnim and Fraser [23] have considered a porous reticulated vitreous carbon (RVC) as inner-core and providing better performance than traditional used materials.

Besides theoretical and experimental studies, numerical simulations and modelling have become a suitable alternative for studying thermoacoustic phenomena involved in SWTAE [24–28]. To this end, Hireche et al. [29] recently performed a 3D- numerical study of natural convection flow using a finite volume method to solve the mixed Navier-Stokes and Darcy-Brinkman equations under Boussinesq approximation in a thermoacoustic device with a porous medium. They highlighted thermal conductivity, permeability, and anisotropy influence of the porous medium on the dynamic and thermal fields. Daru et al [30] analyzed different streaming flow regimes in a resonant waveguide and pointed out two regimes which are function of the acoustic amplitude. Likewise, Daru et al. [31] assessed both numerically and theoretically the interaction between a standing wave and a solid wall resolving the averaged Navier-Stokes equations with acoustic correlation source terms whose effects have been highlighted. Along this same line, Rahpeima and Ebrahimi [32] numerically investigated effects of different geometric parameters and thermophysical properties of the stack. They demonstrated that reducing

thickness and thermal conductivity of stacked plates leads to lower cooling temperatures and higher coefficients of performance. Wang et al [33] presented a study on a one-dimensional time-domain model to predict the onset characteristics of travelling wave thermoacoustic engines with helium as the working gas. They found that the experimental damping temperature is closer to the computed onset temperature than the experimental onset temperature. Afterwards, they stated that the considered time-domain model clearly highlights internal trigger mechanisms involved.

Although many studies have been conducted to numerically investigate thermoacoustic standing wave processes, those that have been conducted using Boltzmann lattice-model methods remain scarce. The acute lack of these investigations motivated the present work. LBMs and their variants offer many assets due to their transient nature, explicitness, the evolution equation linearity, its simple structure, explicit computation avoidance of Poisson equation for pressure, its ability to handle non-linearities (such as acoustics) and all types of boundary conditions, and its straightforward implementation and potential coding on parallel computers. Often, when simulating thermal flows, these methods lean on a dual (double) distribution function (DDF) thermal model where the velocity and temperature fields are each handled by a different lattice Boltzmann equation (LBE). Based on these undeniable strengths, LBMs can be a more suitable alternative to traditional numerical methods such as finite difference, finite volume, finite element, etc., which may involve both a grid generation and tedious computation resolution processes. The LBE depicts the particle distribution function evolvement in the physical momentum space. Compared with the molecular dynamics which analyzes the position and momentum of each particle in fluids, Boltzmann's equation rather concerns a particles cluster occupying a small volume at a given position and short time, and momentum changes of this group (Figure 4.1, §2.1). Thereby, Boltzmann's equation can be applied on a larger scale while covering a wide variety of problems ranging up to nonlinear acoustic thermal problems. Moreover, based on the up-mentioned literature review, very few of these problems have been conducted regarding the simulation of standing wave thermoacoustic processes (from the process onset to the steady state) in a full domain (from left side closed to right end open; see §2.1) using mesoscopic methods such as TLBMs. It is thereby that the helium-filled domain (with a hot buffer, a porous medium filled TAC sandwiched between hot and cold heat exchangers) closed on one side and open on the other deemed as the SWTAE template has been studied numerically via a BGK-TLBM approach. The latter handles the fluid particles evolution using

the collision and streaming processes on a discrete lattice mesh and provides conserved flow variables such as density, momentum, and temperature by performing a local integration of particles distribution functions. It is worthwhile mentioning that such an approach (also called the single-relaxation-time (SRT) method), proposed by Bhatnagar-Gross-Krook (BGK), is a widely used simplification of the complicated Boltzmann collision kernel. This model is accepted as the first truly successful model depicting a particles distribution. It has been widely applied with success in many flow problems with heat transfer in porous or non-porous media and even with phase change. Unfortunately, it turned out to be inadequate in certain cases, such as for example at high Reynolds or Rayleigh numbers or when the Prandtl number is close to unity, i.e. the viscous and thermal effects are equivalent. To be succinct, the stability of the BGK method depends on the unique collision frequency which is a function of the grid resolution and the viscosity.

Much of previous works has confirmed that LBMs have the ability and accuracy required to capture acoustic oscillations that may occur in TAEs [34–39], to cite a few.

Nonetheless, it remains unknown whether a TLBM approach can address a topic dealing with Rayleigh streaming and heat transfer in a TAC filled with a porous medium and where the temperature difference is a key parameter.

This paper aims to answer that issue or at least provide some clarification. Firstly, using a DDF-TLBM with specular reflective bounce-back (SRBB) approach while securing the temperature and heat flux continuity at the fluid-solid interface. A numerical simulation is then performed to examine both dynamic/acoustic characteristics within the entire SWTAE and the thermal efficiency while highlighting the thermal gradient and porosity impacts. The findings thereby exhibited will certainly set the stage for more numerical simulations of such devices with the TLBM approach.

The remainder of this paper is split as follows: Section 2 presents the problem statement, its mathematical formulation and the associated simplifying conditions. Section 3 introduces the performance indicator used to characterize the TAC. Section 4 sets out the TLBM adopted to handle governing equations. Thereafter, the code validation is reported in section 5. Section 6 develops and comments on the outcomes obtained. Finally, conclusions are drawn in Section 7.

4.2 Problem statement, mathematical formulation and assumptions

4.2.1 Model aim and description

It is worth pointing out that standing wave devices are simple in structure with no moving parts. They are mainly composed of a resonator tube, a hot buffer and a core usually made of stacked plates or a porous medium (PM) sandwiched between a pair of cold and hot heat exchangers. When the working fluid passes through the engine hot part, the heat is partly converted into acoustic work [40]; it oscillates spontaneously through the PM (or stack if there is any) while passing to the cold side generating acoustic waves which can be converted into electrical energy using an generator such as an alternator [41].

	$CaCO_3$ (PM)	Stainless steel (HE)	Copper (CE)	Helium (Working fluid)
Density $[Kg/m^3]$	2600	7850	8960	0.179
Thermal conductivity $[W/mK]$	2.7	44.50	386	0.1513
Specific heat $[J/kgK]$	900	475	383	5193

Table 4.1: Materials kind used and working fluid physical properties.

Figure 4.1a shows the standing wave thermoacoustic engine (SWTAE) sketch with its left end $(X = 0.0m)$ closed and right end $(L = 1.0m)$ opened to an electric generator. Explicitly, the helium-filled SWTAE is mainly made up of a hot buffer, a PM-filled TAC placed between a hot exchanger (HE; left side) and a cold exchanger (CE; right side). The TAC is modeled as a saturated, homogeneous and isotropic porous medium ($CaCO_3$) and whose thermophysical properties are gathered in Table 4.1. The hot and cold plates' exchangers (PM's left and right sides) made of stainless steel and copper are placed at $X_H = 0.2$ m and $X_F = 0.4$ m , respectively. Their lengths are respectively $X_S - X_H \quad (= 3.10^{-2}m)$ and $X_C - X_F \quad (= 2.10^{-2}m)$ with 60% porosity for better numerical stability and computational time of simulations.

The CE is followed by a resonator of length $L - X_C$. The two commonly TAEs are sketched in Figure 1b, while Figure 1c shows the structural schematic diagram of the baseline model (heater, PM, cooler and resonator) deemed in CFD computations.

To sum up, the basic model's dimensions and types deemed here are listed in Table 4.2.

Item	Length (m)	Materials
Hot buffer (HB)	$X_H = 0.2$	-
Hot exchanger (HE)	$X_S - X_H = 0.03$	Stainless steel
Porous medium (TAC)	$X_F - X_S = 0.17$	$CaCO_3$
Cold exchanger (CE)	$X_C - X_F = 0.02$	Copper
Resonator (R)	$L - X_C = 0.58$	-

Table 4.2: Dimensions of the SWTAE's main parts.

Note that the working fluid is initially set at ambient temperature and uniform atmospheric pressure. Besides, the outer walls of the TAC are exposed to ambient air. The hot and cold exchangers generate a thermal gradient (resulting from a temperature difference) at the TAC limits, and a linear decrease from the higher temperature to the lower temperature is thereby applied to the upper and lower core's walls.

4.2.2 Simplifying conditions and governing equations

The assumptions that match to the subsequent mathematical model depicting physical phenomena which arise inside the SWTAE (Eqs. (4.1)-(4.3) hereinafter) are:

- The working fluid (helium) is assumed to be weakly compressible for which the condition $Ma < 0.3$ is achieved;
- The physical properties of the fluid and the solid are assumed to be constant with respect to the temperature except for the density which ascertain the Boussinesq assumption;
- The convective flow is laminar and viscous;
- The flow in the porous medium is considered as the Brinkman-Forchheimer-Darcy's flow (BFD);
- The fluid flow is assumed to be unsteady and two-dimensional;

It is noteworthy that such an approximation acts as a stabilizer of the base flow through the porous medium while preserving the weakly compressible character of the working fluid. The SWTAE channel being straight, the Cartesian coordinate system is used to describe the fluid flow whose X and Y -axis depict the lengthwise and upright directions. With the assumptions and conditions up stated above-mentioned, the spatio-temporal equations (conservations of mass, momentum and energy) in dimensional form governing the thermoacoustic conversion process within the saturated SWTAE under Boussinesq assumption can be expressed as follows [42]:

$$\nabla.\vec{U} = 0 \tag{4.1}$$

$$\frac{\partial \vec{U}}{\partial t} + (\vec{U}.\nabla)\left[(\frac{\Theta}{\varepsilon} + (1-\Theta))\vec{U}\right] = -\nabla\left((\Theta\varepsilon + (1-\Theta))\frac{P}{\rho_f}\right) + \nu_f(\varepsilon\Theta + (1-\Theta))\nabla^2\vec{U} - \Theta\left[\frac{\varepsilon\nu_f}{K} + \frac{\varepsilon F_\varepsilon}{\sqrt{K}}|\vec{U}|\right]\vec{U} + ((1-\Theta) + \Theta\varepsilon)g\beta(T - T_{ref})\vec{e_Y} \tag{4.2}$$

$$\left((1-\Theta)C_{pf} + \Theta C_{pe}\right)\frac{\partial T}{\partial t} + (\vec{U}.\nabla)(C_{pf}T) = \left((1-\Theta)k_f + \Theta k_e\right)\frac{\nabla^2 T}{\rho_f} + \Theta\varepsilon\left(\frac{\nu_f}{K} + \frac{F_\varepsilon}{\sqrt{K}}||\vec{U}||\right)||\vec{U}||^2 + \bar{\bar{\tau}} : \bar{\bar{D}}/2 \tag{4.3}$$

where $(\rho C_p)_e = \varepsilon(\rho C_p)_f + (1-\varepsilon)(\rho C_p)_s$ and $k_e = \varepsilon k_f + (1-\varepsilon)k_s$ with subscripts e , f and s standing for effective, fluid and solid parts.

In Eqs. (4.1) - (4.3), $\vec{U}(U\vec{e_X} + V\vec{e_Y})$ P and T are the volume-averaged velocity, pressure and temperature over the computational cell. g , $\beta = 1/T_{ref}$, and ν_f are gravity acceleration, thermal expansion coefficient, and kinematic viscosity. In addition ε and F_ε denote the porous medium's porosity and the Forchheimer coefficient (inertial coefficient) which is function of porosity and pore medium, respectively. As for the other variables and indices involved, reference may be made to the nomenclature.

The last term of Eq. (4.3) points out viscous dissipation whose expression is:

$$\Phi = \Theta\varepsilon\left(\frac{\nu_f}{K} + \frac{F_\varepsilon}{\sqrt{K}}||\vec{U}||\right)||\vec{U}||^2 + \bar{\bar{\tau}} : \bar{\bar{D}}/2 \tag{4.4}$$

$\bar{\bar{\tau}}$ et $\bar{\bar{D}}$ being the Newtonian shear stress and strain-rate tensors described by

$$\bar{\bar{\tau}} = 2\mu\bar{\bar{D}} \quad and \quad \bar{\bar{D}} = (\nabla\vec{U} + \nabla^t\vec{U})/2 \tag{4.5}$$

The thermophysical characteristics of the porous medium are its porosity ε , its permeability K , and its equivalent (effective) thermal conductivity k_e. Note that, for convenience, a binary parameter is regarded herein to unify the equations writing based on the media nature involved ($\Theta = 0$ for the fluid medium, $\Theta = 1$ for the porous medium) letting appear an additional term called the BFD term (3rd term on the right's sign "=" of Eq. (4.2)).
The permeability and porous medium geometrical function have been set as:

$$K = \varepsilon^3 d_p^2 (150(1-\varepsilon)^2)^{-1} \quad and \quad F_\varepsilon = 1.75(150\varepsilon^3)^{-0.5} \tag{4.6}$$

where d_p is the mean diameter of the equivalent spherical pores for the porous medium which has been freely set to set to 3.3 µm.

4.2.3 Boundary and initial conditions

The implementation of the initial (I) and boundary conditions (BCs) being needful in the numerical handling of any flow problem with or without heat transfer to pick up an appropriate solution, the initial and boundary conditions associated with the afore formulated equations are enforced on the geometric boundaries:

- $\partial U/\partial X = 0$ (specular reflective boundary); $V = 0$; $T = T_w$ at $X = 0$ and $0 < Y < H$ (left boundary);
- $\partial U/\partial X = \partial V/\partial X = 0$ at $X = L$ and $0 < Y < H$ (right boundary);
- $V = 0$; $\partial U/\partial Y = 0$ (specular reflective boundary); $T = T_w$ at $0 < X < L$, $Y = 0$ and $Y = L$ (lower and upper boundaries);
- $T = T_H$ at $X_H < X < X_S$ and $0 < Y < H$ (HE);
- $T = T_C$ at $X_F < X < X_C$ and $0 < Y < H$ (CE);
- Lastly , a non-slip condition is enforced on the porous TAC's limits forming the solid-

fluid interfaces ($X = X_H$ and $X = X_C$) of the porous core to maintain flow continuity:

$$\vec{U}(X,t)_{/_p} = \vec{U}(X,t)_{/_f} \quad and \quad \varepsilon^{-1} < \partial\vec{U}/\partial X|_{/_p} =< \partial\vec{U}/\partial X|_{/_f} \tag{4.7}$$

- Likewise, at these same interfaces, temperature and transverse heat fluxes continuity is translated as follows:

$$T(X,t)_{/_f} = T(X,t)_{/_p} \quad and \quad < k_e \partial T(X,t)|_{/_p}/\partial X =< k\partial T(X,t)|_{/_f}/\partial X \tag{4.8}$$

  Recall that subscripts p and f point out, respectively, the porous and fluid domains.

- The initial conditions include zero velocity (motionless fluid), charge pressure (Atmospheric pressure) and inside temperature of $298K$.

4.2.4 Dimensionless governing equations

It is more appropriate to consider the dimensionless transport equations instead to facilitate outcomes interpretation using dimensionless variables indicated by lowercase letters. These can be obtained through the following parameters:

$$(u,v) = (\frac{U}{U_{ref}}, \quad \frac{V}{U_{ref}}), \quad (x,y) = (\frac{X}{L}, \quad \frac{Y}{H}), \quad \tilde{t} = t\frac{U_{ref}}{H}, \quad p = \frac{P}{\rho_{fo}c_s^2}, \quad \theta = \frac{(T-T_C)}{(T_H-T_C)} \tag{4.9}$$

$U_{ref} = \sqrt{(2P_o/\rho_{fo})}$, ρ_{fo} (=0.179) and c_s being the reference velocity, the density and the sound speed, respectively.

Through this nondimensionalization process, relevant dimensionless parameters appear, viz., the Reynolds number $Re \quad (= U_{ref}H/\nu)$, the Darcy number $Da \quad (K/(\varepsilon H^2))$, the Eckert number $E_C \quad (= U_{ref}^2/(C_p\Delta T))$, to name a few. Subsequently, Eqs. (4.1) - (4.3) can be further rewritten in the following dimensionless form:

$$\nabla.\vec{u} = 0 \tag{4.10}$$

$$\frac{\partial \vec{u}}{\partial \tilde{t}} + (\vec{u}.\nabla)\left[(\frac{\Theta}{\varepsilon} + (1-\Theta))\vec{u}\right] = -\nabla\left((\Theta\varepsilon + (1-\Theta))\, p\right) + \frac{1}{Re}\nabla^2\vec{u} - \Theta\left[\frac{\varepsilon}{ReDa} + \frac{\varepsilon F_\varepsilon}{\sqrt{Da}}||\vec{u}||\right]\vec{u} - ((1-\Theta) + \Theta\varepsilon)PrRa(\theta - \theta_{ref})\vec{e_y} \quad (4.11)$$

$$[1 + \Theta(1-\varepsilon)(R_C - 1)]\frac{\partial \theta}{\partial \tilde{t}} \quad + \quad (\vec{u}.\nabla)\theta \quad = \quad [1 + \Theta(1-\varepsilon)(R_K - 1)]\nabla^2\theta \quad + \quad \phi \quad (4.12)$$

with parameters $Pr = \mu C_{pf}/k_f$, $Ra = \frac{g\beta(T_H - T_C)}{\nu\alpha}H^3$, $R_k = \varepsilon + (1-\varepsilon)\frac{k_s}{k_f}$ *and* $R_c = \varepsilon + (1-\varepsilon)\frac{(\rho C_p)_s}{(\rho C_p)_f}$ indicating the Prandtl number, thermal conductivities ratio and heat capacities ratio, respectively.

ϕ is the dimensionless viscous dissipation which is set as:

$$\phi = \Theta E_c(\frac{1}{ReDa} + \frac{\varepsilon F_\varepsilon}{\sqrt{Da}}||\vec{u}||)||\vec{u}^2|| + \frac{E_C}{Re}(\bar{\bar{d}} : \bar{\bar{d}}) \quad (4.13)$$

To solve the dimensionless governing equations (4.10) - (4.12), appropriate dimensionless initial and boundary conditions are applied, which are gathered in Table 4.3.

Boundary	Condition
$\tilde{t}$ =0	$u = v$ =0; $\theta = \theta_w \; \forall$ x and y
$x = 0$ and $0 < y < 1$	$\frac{\partial u}{\partial x} = 0$; $v = 0$ and $\theta = \theta_w$
$x = 1$ and $0 < y < 1$	$\frac{\partial u}{\partial x} = \frac{\partial v}{\partial x} = 0$
$0 < x < 1$ and $y = 0$ and $y = 1$	$v = 0$; $\frac{\partial u}{\partial y} = 0$ and $\theta = \theta_w$
$x_H < x < x_S$ and $0 < y < 1$	$\theta = \theta_H$
$x_F < x < x_C$ and $0 < y < 1$	$\theta = \theta_C$
$0 < y < 1$, $x = x_H$ and $x = x_C$	$< \varepsilon^{-1}\partial\vec{u}/\partial x\|_p =< \partial\vec{u}/\partial x\|_f$, $\vec{u}_p = \vec{u}_f$, $\theta_p = \theta_f$, $\frac{k_e\partial\theta}{\partial x}/_p = \frac{k\partial\theta}{\partial x}/_f$

Table 4.3: Boundary conditions synopsis used in the study

It is worth noting that in the LBM context, these macroscopic boundary conditions must be translated using mesoscopic distribution functions while maintaining their physical meaning (see §4.4.3 hereinafter).

4.3 Performance indicator

The thermal efficiency is seemingly the best quantity to typify the considered TAE. It can be defined as follows [43]:

$$\eta = 100W/Q \tag{4.14}$$

where $W(= S|P||U|cos(\psi)/2)$ is the net acoustic power gain when the sound wave passes through the TAC, $Q(= \dot{m}C_p(T_H - T_C))$ is the heat input at the porous medium (PM) boundaries, S is the cross-sectional area, and $\dot{m}$ is the masse flow rate (Kg.s-1).

4.4 Thermal lattice Boltzmann method

The Boltzmann equation depicts the particle distribution function (PDF) evolvement in the physical momentum space over a discrete lattice domain. Such a domain is subdivided into a structured lattice with the characteristic variables analogously to the meshes used in traditional schemes (finite differences, finite volumes, etc.). Transient macroscopic fluid characteristics are achieved via the two main ingredients of the lattice-Boltzmann Equation (LBE), viz streaming and collision processes. Simply put, variables such as density, momentum and temperature are obtained by performing local integration of the particle distribution function. Compared with the molecular dynamics which analyzes the position and momentum of each particle in fluids, Boltzmann's equation rather concerns a particles cluster occupying a small volume at a given position and short time, and momentum changes of this group (Figure 4.2 should be stood at a point inside Figure 4.1b). Thereby, the Boltzmann equation can be applied for a larger scale than the molecular dynamics, and seems suitable to address flow and heat transfer characteristics in thermoacoustic devices.

4.4.1 Lattice Boltzmann equation for the dynamic field

The discretized lattice Boltzmann equation (LBE) for incompressible low Mach number fluid flow with the Bhatnagar-Gross-Krook (BGK) approximation is as follows [44]:

$$f_i(x + c_i\Delta t, t + \Delta t) - f_i(x,t) = -\Delta t\,\tau_m^{-1}[f_i(x,t) - f_i^{eq}(x,t)] + \Delta t F_{ei} \tag{4.15}$$

where $\tau_m(=3\nu\Delta t/(\Delta X)^2+0.5)$ is the momentum dimensionless relaxation time, $F_{ei}(=F_i\frac{(c_i-u_i)^2}{RT_{ref}}f_i^{eq})$ depicts the total force and f_i^{eq} (equilibrium distribution function) is a mere approximation of the Maxwell–Boltzmann distribution, which for the D2Q9 model can be defined as:

$$f_i^{eq}=\rho\omega_i\Big[1+\frac{c_i\vec{u}}{c_s^2}+\frac{(c_i\vec{u})^2}{2(\Theta\varepsilon+(1-\Theta))c_s^4}-\frac{\vec{u}\vec{u}}{2(\Theta\varepsilon+(1-\Theta))c_s^2}\Big] \tag{4.16}$$

$c_i(=\sqrt{3c}/3$ is the lattice sound speed.
where ω_i is weighting factor defined as

$$\omega_i=\begin{cases}\frac{4}{9} & i=0\\ \frac{1}{9} & i=1,2,3,4\\ \frac{1}{36} & i=5,6,7,8\end{cases}$$

The total force $\vec{F}$ induced by porous matrix and buoyancy and enabling to couple the velocity and temperature fields is given as [45,46]:

$$\vec{F}=-\Theta[\frac{\varepsilon}{ReDa}+\Theta\frac{\varepsilon F_\varepsilon}{\sqrt{Da}}\mid\vec{u}\mid]\vec{u}-((1-\Theta)+\Theta\varepsilon)G\vec{e_y} \tag{4.17}$$

$G=PrRa(\theta-\theta_{ref})$ being the buoyancy term.

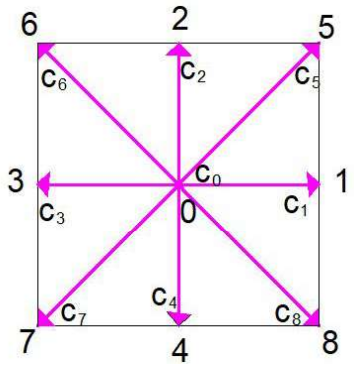

Figure 4.2: Lattice stencil for the D2Q9 model

The classical phase space model D2Q9 selected herein is depicted in Figure 4.2 whose lattice velocities are given by:

$$c_i = \begin{cases} (0,0) & i = 0 \\ (1,0),(0,1),(-1,0),(0,-1) & i = 1,2,3,4 \\ (1,1),(-1,1),(-1,-1),(1,-1) & i = 5,6,7,8 \end{cases}$$

Note that the choice of the BGK approximation was dictated by a simplification sake of implementation and computation cost reducing.
Lastly, the macroscopic fluid variables, density ρ , velocity u and pressure p are achieved from the distribution function moments $f_i(x,t)$ as follows:

$$\rho(x,t) = \sum_i f_i(x,t); \quad \rho(x,t)u(x,t) = \sum_i c_i f_i(x,t) + \rho(x,t)\Delta t F_{ei}; \quad p(x,t) = c_s^2 \rho(x,t) \quad (4.18)$$

From an algorithmic point of view, it is worthwhile to mention that the lattice Boltzmann method achieves the simulation through the classical collision and streaming (advection) processes of particle distribution functions (PDFs). That is, the collision relaxes the distribution functions to a local equilibrium, while the streaming propagates the post-collision distribution functions to new lattice locations.

4.4.2 Lattice Boltzmann equation for the thermal field

To characterize the thermal field, a second particle distribution function, $g_i(x,t)$, is used and whose discrete evolution equation is expressed as follows [47] to cite a few:

$$g_i(x + c_i\Delta t, t + \Delta t) - g_i(x,t) = -((1-\Theta)\tau_s + \Theta\tau_{sm})^{-1}\Delta t[g_i(x,t) - g_i^{eq}(x,t)] + \Delta t\tilde{\phi}_i \quad (4.19)$$

where τ_s is the dimensionless thermal relaxation times in the hot buffer and resonator, while τ_{sm} is dimensionless time characterizing heat transfer between gas particles and the TAC walls. Their respective expressions are [48, 49]:

$$\tau_s = (3\frac{\Delta t}{(\Delta x)^2}\alpha + 0.5) \quad and \quad \tau_{sm}(= 3Pr(\tau_m - 0.5)\frac{R_k}{R_C} + 0.5) \quad (4.20)$$

with Pr, R_k and R_C previously set via relationships (4.13) [48].

Moreover, the equilibrium particle distribution function of temperature $g_i^{eq}(x,t)$ can be put in the following form [45,50]:

$$g_i^{eq}(x,t) = \theta(x,t)\omega_i(1+\frac{c_i u}{c^2}) \tag{4.21}$$

The last term in Eq. (4.20) is the dimensionless viscous heat dissipation, and it can be stated via relationship:

$$\tilde{\phi}_i = \omega_i[1+\frac{c_i u}{{c_s}^2}(\frac{\tau_{sm}-0.5}{\tau_{sm}})]\tilde{\phi} \tag{4.22}$$

where the ϕ expression has already been specified from above (relationship (4.14)).

The macroscopic temperature is evaluated from:

$$\theta(x,t) = \sum_i g_i(x,t) \tag{4.23}$$

4.4.3 Implementation of dynamic and thermal BCs in the LBM context

In the TLBM framework, the BCs for velocity and temperature are translated in terms of the microscopic distribution functions f_i and g_i. Herein, it is obvious that these conditions are both dynamic and thermal. In the present framework and on the basis of the so-called specular reflective bounce-back approach adopted [50, 51], these BCs can be stated as follows

Dynamic boundary conditions (DBCs)

The DBCs can be suggested as:

- $f_1 = f_3$; $f_5 = rf_7 + (1-r)f_6$; $f_8 = rf_6 + (1-r)f_7$ (Left (closed) boundary)
- $f_{3/n} = f_{3/n-1}$; $f_{7/n} = f_{7/n-1}$; $f_{6/n} = f_{6/n-1}$ (Right (open) boundary)
- $f_2 = f_4$; $f_5 = rf_7 + (1-r)f_8$; $f_6 = rf_8 + (1-r)f_7$ (Lower boundary)
- $f_4 = f_2$; $f_7 = rf_5 + (1-r)f_6$; $f_8 = rf_6 + (1-r)f_5$ (Upper boundary)

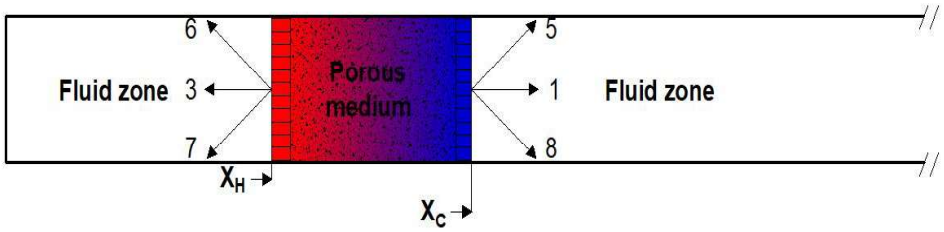

Figure 4.3: Illustrative sketch of basic lattices for fluid-solid interface treatment

It is worth recalling that r and $(1-r)$ points out the proportion bounce-back reflection and specular reflection proportion with wall, respectively.

- At $x = x_H$ and $x = x_C$ (Figure 4.3) , a fluid-solid interface condition is prescribed as:

$$f_{i/p} = f_{i/f} \tag{4.24}$$

where the subscript i denotes the appropriate variable.

Thermal boundary conditions (TBCs)

The TBCs can be depicted as:

- $g_1 = \theta_w(w_1+w_3) - g_3; \quad g_5 = \theta_w(w_5+w_7) - g_7; \quad g_8 = \theta_w(w_8+w_6) - g_6$ (Left boundary);
- $g_2 = \theta_w(w_2+w_4) - g_4; \quad g_5 = \theta_w(w_5+w_7) - g_7; \quad g_6 = \theta_w(w_6+w_8) - g_8$ (Lower boundary);
- $g_4 = \theta_w(w_4+w_2) - g_2; \quad g_7 = \theta_w(w_7+w_5) - g_5; \quad g_8 = \theta_w(w_8+w_6) - g_6$ (Upper boundary);
- $g_3 = \theta_H(w_3+w_1) - g_1; \quad g_7 = \theta_H(w_7+w_5) - g_5; \quad g_6 = \theta_H(w_6+w_8) - g_8$ (HE; $0 < y < 1$ & $x_H < x < x_S$)
- $g_1 = \theta_C(w_1+w_3) - g_3; \quad g_5 = \theta_C(w_5+w_7) - g_7; \quad g_8 = \theta_C(w_8+w_6) - g_6$ (CE; $0 < y < 1$ & $x_F < x < x_C$)

It should be mentioned that the unknown temperature at the outlet is set as [52]:

$$g_3 = \tfrac{1}{9}\theta^{eq}(1 - \tfrac{3}{c_s^2}u) \quad g_6 = \tfrac{1}{36}\theta^{eq}(1 - \tfrac{3}{c_s^2}(u-v)) \quad g_7 = \tfrac{1}{36}\theta^{eq}(1 - \tfrac{3}{c_s^2}(u+v)) \tag{4.25}$$

with $\theta^{eq} = \frac{6(\theta_w - \theta_p)}{1+\frac{3}{c_s^2}u}$ and $\theta_p = g_0 + g_2 + g_3 + g_4 + g_5 + g_8$
It follows that the unknown distribution function g_i is obtained by the following relationship:

$$g_i = \omega_i \theta^{eq} \tag{4.26}$$

Lastly, the heat transfer continuity at the porous TAC inlet and outlet is ensured numerically as follow:

$$\begin{aligned} g_{i/x_o} &= g_{i^-_{/x_o}} \\ g_{i/x_o} &= \frac{4}{3}g_{i_{/x_o+\Delta x}} - \frac{1}{3}g_{i_{/x_o+2\Delta x}} - k_f g_{i^-_{/x_o}} + \frac{4}{3}k_f g_{i^-_{x_o-\Delta x}} - \frac{1}{3}k_f g_{i^-_{/x_o-2\Delta x}} \end{aligned} \tag{4.27}$$

The subscript i^- denotes the opposite lattice index. x_o is the positions of fluid-solid interfaces(x_H or x_C).

4.5 Independence tests and preliminary validation

4.5.1 Grid and time step independence tests

To achieve a grid size independence solution, a grid independence check was performed using four sets of grids (from coarse grid to fine one). This needful step is intended to better establish the precision and correctness of subsequent computations. Thereby, by exploring four mesh combinations (600X30, 800X40, 1000X50, 1200X60), Figure 4.4 exhibits the velocity U evolvement vs. the lengthwise direction X at $Y = H/2$ for the case of $Re = 100$, $Pr = 0.67$, $\varepsilon = 0.6$, $T_H = 100$ °C and $T_C = 20$ °C.
The flow becomes insensitive to the number of nodes from the grid 1000X50. In addition, it can be seen that the average difference between the two largest grids (1000X50 and 1200X60) does not exceed 2% of errors indicating that the size of the 1000X50 -grid guarantees a solution independent of the grid as portrayed by this figure. Simply put, beyond these grids, the difference is greatly phased out. Then, to deal with the time-step independence-test, preliminary simulations have been performed at the same Re value by selecting the -grid and time steps ranging from 0.2 to 1 while keeping computational domain size identical.

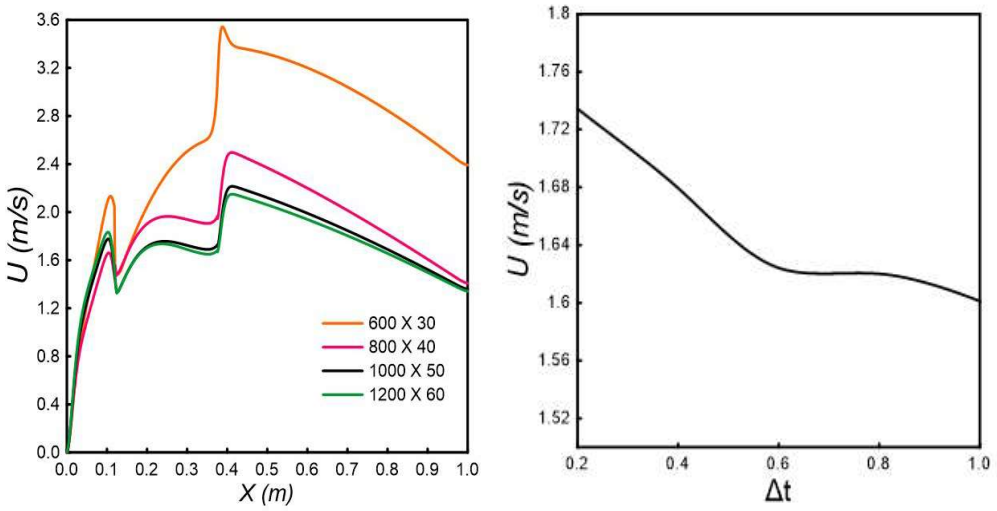

(a) (b)

Figure 4.4: Lengthwise velocity U dependence vis-à-vis a) the grid and b) time-step

Figure 4.4b depicts the time-step effect on velocity U. From these tests, it appears that this quantity has converged for the grid from the time step $\Delta t = 0.8$ with a deviation of about 3% between $\Delta t = 0.8$ and $\Delta t = 1$ This highlights the adequacy of this grid and the time step for subsequent computations.

4.5.2 Model validation

To tackle the crucial issue of comparing with available results, preliminary validations of our in-house numerical code were conducted to assess the solution accuracy achived via the BGK-TLBM deemed here. Thereby, the previous study of Kuzuu et al. [53] dealing with the flow and heat transfer in a simple standing wave engine is taken as a benchmark to validate current method. The phase variation of the axial velocity profile within a cycle at the middle section of the stack is compared with results from linear theory and LS-FLOW solver [53] in Figure 4.5. It can be seen that our results corroborate the reference solutions with non-significant variations of which the maximum is around 4.45%. In addition, the linear theory exhibits symmetrical acoustic oscillations over a period, while the LBM simulation shows a slight deviation of acceleration and deceleration trajectories. A slight overshoot of the sectional speed profile appears near the walls of the plate called the “Richardson effect”. Such an effect is involved within the oscillatory permanent flow induced by the viscous force due to the interaction of the fluid particles in the close vicinity of plates.

To sum up, from this comparison, it appears that the numerical approach provides satisfying results, highlighting the reliability of our in-house code implemented.

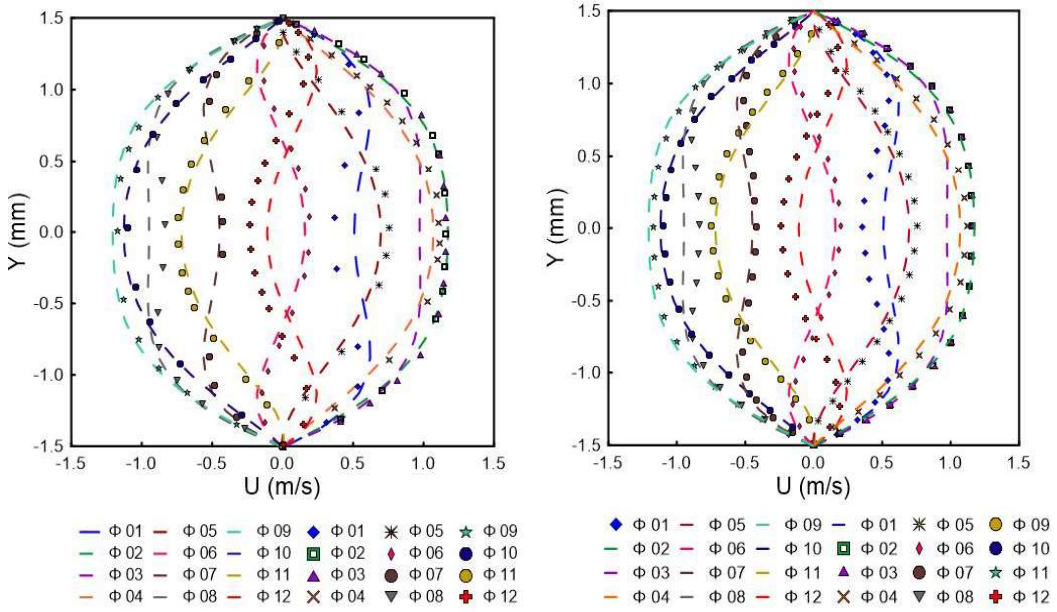

(a) (b)

Figure 4.5: Streamwise velocity profiles vs. upright distance Y to the TAC's middle section ($X = L/2$) set by the phase ψ (degree). a) LBM results (symbols) and linear theory (dashed lines); (b) LBM results (symbols) and CFD via LS-FLOW solver (dashed lines)[53]

4.6 Results and analysis

Before presenting and commenting on the salient results obtained, it is worth reiterating that it is the numerical simulation of an unsteady convection flow in an closed-open-SWTAE channel (see Sections 2 and 4) via a thermal BGK-LBM which has been targeted. Through the LB simulations, the thermal and acoustic response of the SWTAE with a thermal gradient ($\Delta T (= T_H - T_C)$) around the SWTAE has been successfully achieved. The main simulations were carried out for relevant parameters, viz. $Re = 100$, $Pr = 0.67$, $\varepsilon = 0.6$ and $T_C = 20$ °C. Furthermore, it should also be recalled that the LBM simulations conducted concern a simplified computational domain made up of a semi-open straight tube (Figure 4.1 c) mainly comprising a porous medium filled TAC placed between two hot and cold exchangers and two resonators located from either sides.

It should also be pointed out that simulations are performed until convergence is reached by specifying that the relative error of a quantity (between adjacent time steps) becomes less than a pre-specified value at around 10^{-5}.

4.6.1 Heat transfer stabilization in the porous core

The thermoacoustic conversion through the porous core gives rise to several undesirable effects such as vortices generation and Rayleigh and acoustic streaming. The average flow is mainly coupled with heat exchange and standing waves interaction which are the main source of heat transfer. Indeed, self-sustained acoustic oscillations generation involves the application of a fitting longitudinal temperature gradient between the porous core ends giving rise to significant thermo-viscous interactions. In addition, using the helium as a working fluid lets compression and expansion at low temperature and even at less than 10 °C at atmospheric pressure, and the HE can deliver temperatures of 40 °C, 60 °C, 80 °C and 100 °C to the working fluid. It is well accepted that self-excited acoustic oscillations occur inside the TAE if T_H (T_C being kept fixed) exceeds a certain value (called the onset temperature).

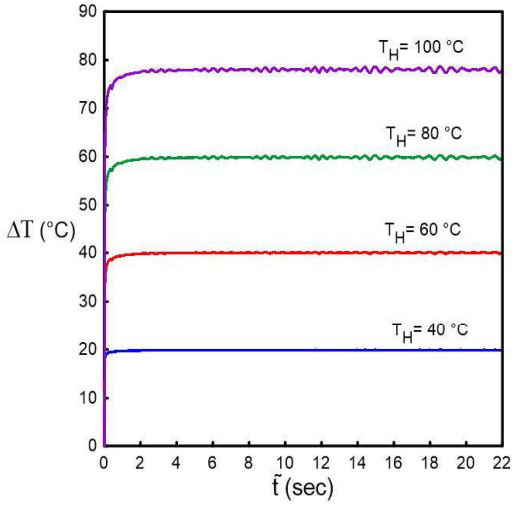

Figure 4.6: Difference temperature's time evolution ΔT at the start-up for $Re = 100$, $Pr = 0.67$, $\varepsilon = 0.6$ and $T_C = 20$ °C

Figure 4.6 presents the temperature difference Δ T evolution vs. computation time at the startup for $T_C = 20$ °C, $\varepsilon = 0.6$, $Re = 100$ and $Pr = 0.67$. As can be seen, the temperature difference increases sharply to tend towards a plateau which presents oscillations. At the initial times, it can be noted that the temperature fluctuates due to thermal conduction within the porous core (PM) which causes thermo-viscous losses near the exchangers.

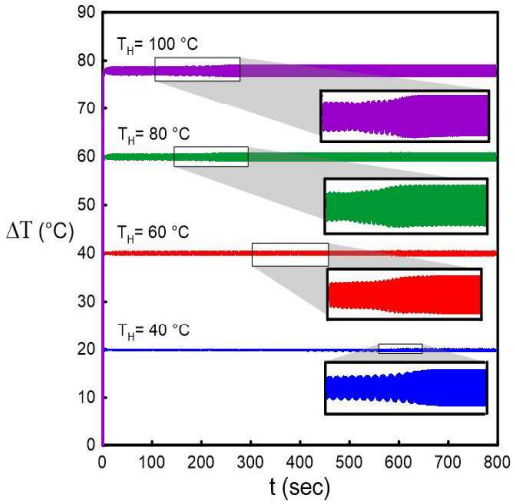

Figure 4.7: Time evolution of the temperature difference $\Delta T = T_H - T_C$ for T_C =20°C, ε=0.6, Re=100 and Pr=0.67

Figure 4.7 depicts the evolution of the temperature difference ΔT vs. the CPU time $\tilde{(t)}$ (computation time). The numerical investigations are achieved for the different temperatures considered at the HE level, viz. 40 °C, 60 ° C, 80 ° C and 100 °C, while the CE temperature is fixed at T_C = 20 °C. Note that, initially, the engine is in a linear unsteady state where the working fluid gradually starts to absorb heat by conductive transfer resulting in improved linear unsteady instability. This indicates that the weak interfacial interaction near exchangers governs the small amplitudes thermal oscillations. Moreover, the thermo-viscous losses are increasingly negligible compared to the convective heat transfer which improves the temperature amplitude while speeding-up the acoustic excitation onset. Simply put, the greater the temperature gradient, the more the interaction between the unsteady oscillations and the heat transfer by conduction becomes less and less linear. Besides, periodic thermal expansion and compression during a cycle induces steady sinusoidal thermal standing-waves whose amplitude extends significantly.

4.6.2 Thermoacoustic oscillations analysis

Figure 4.8 exhibits the time evolution of the streamwise acoustic velocity with time at the midcore ($(X = X_F + X_S)/2$ and $Y = H/2$) for $Re = 100$ and ε=0.6. The HE temperature is varied from 40 °C to 80 °C, while the CE temperature is maintained at T_C =20 °C. All figures (4.8 a-d) demonstrate the complete process of producing acoustic oscillations. They evolve in stages: Onset oscillation occurs due to the prompt increase in pressure. Then, it increases sharply while continuing to fluctuate to tend towards the steady state, after having heated the

TAC.

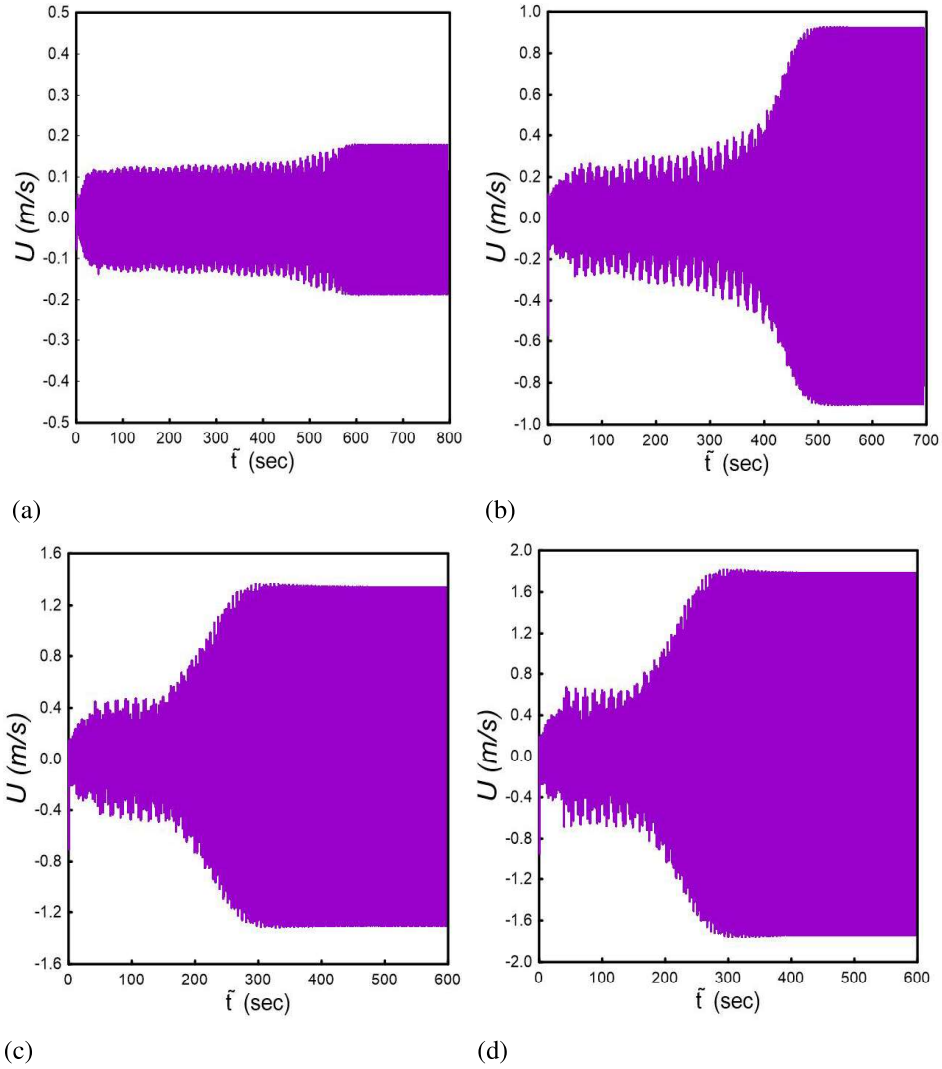

Figure 4.8: Time evolution of the self-sustaining acoustic velocity$X = \frac{X_F+X_S}{2}$ and $Y = \frac{H}{2}$ for Re=100, Pr=0.67 and ε=0.6 with (a) T_H=40°C (b) T_H=60°C (c) T_H=80°C (d) T_H=100°C

The pressure gradient between the engine inputs serves to generate weak acoustic oscillations visible at start-up and which dissipate afterwards. Thereby, by heat exchangers launching, the acoustic velocity amplitude is slightly improved thanks to the advanced coupling between the disturbed fluid motion and the unstable convective flow (buoyancy term effect). This linear unstable state will be further discussed later (see Figure 4.9 hereinafter). It can be clearly seen that the onset of the engine is retarded at low temperature gradient. Indeed, the conduction being dominant within the core, it causes an inefficient compression-expansion of gas and slows down the engine onset. The steady state is marked when the working fluid is expanded and compressed according to a periodic and harmonic motion (see Figure 4.10 below).

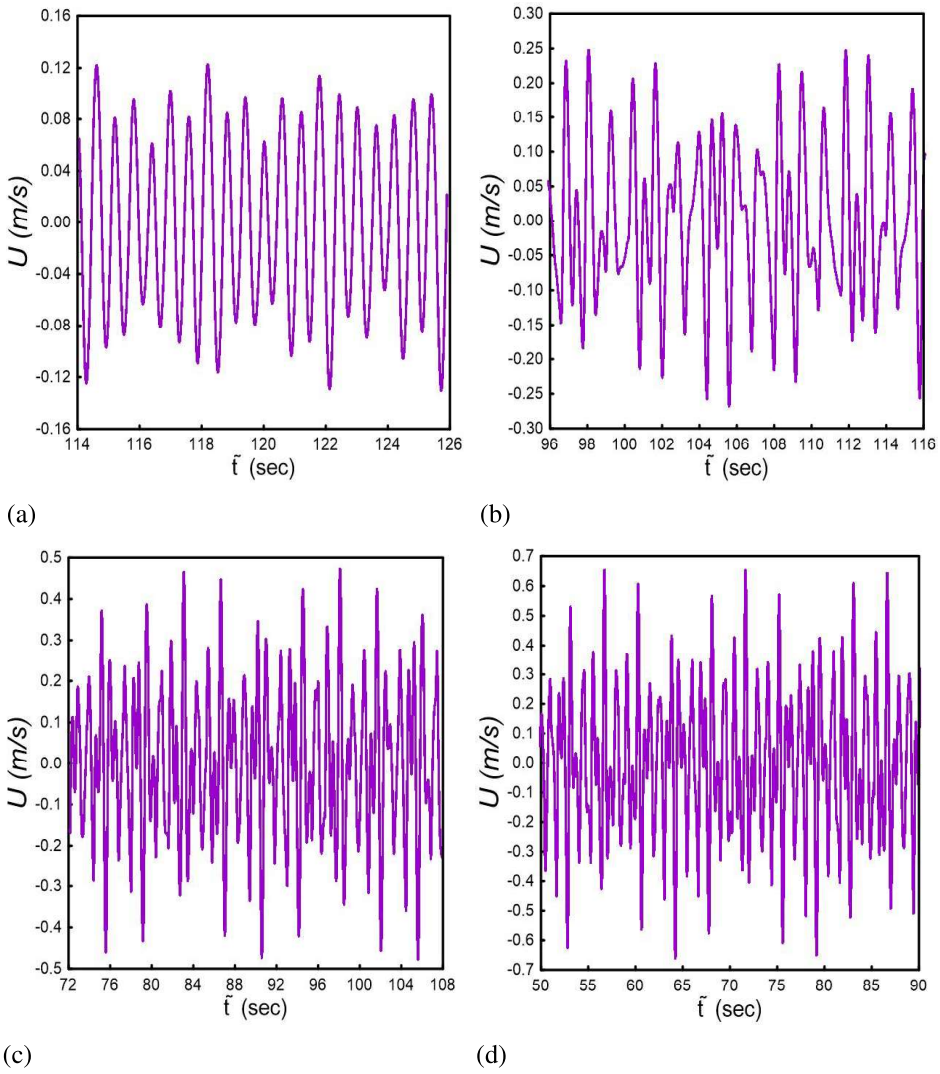

Figure 4.9: Time history of mid-core U -acoustic velocity at $X = \frac{X_F+X_S}{2}$ and $Y = \frac{H}{2}$ for Re=100, Pr=0.67 and ε=0.6 with (a) T_H =40 °C ; (b) T_H =60 °C ; (c) T_H =80 °C; (d) T_H =100 °C.

Figure 4.9 plots time history of mid-core U -acoustic velocity at $X = \frac{X_F+X_S}{2}$ and $Y = \frac{H}{2}$ for $Re = 100$, $Pr = 0.67$ and ε=0.6 at different$T_H$for the quasi-steady state. For low heat input, nonlinear convective heat transfer is insignificant, while conductivity governs smooth nonharmonic sound waves (Figure 4.9a). On the other hand, at high temperatures, the waves are captured and the nonlinear convection starts to control the non-harmonic acoustic propagation (Figures 4.9b-d). Indeed, the non-linear interaction between the non-harmonic movements improves the thermoacoustic conversion and rises the compressive/expansion power of the working gas.

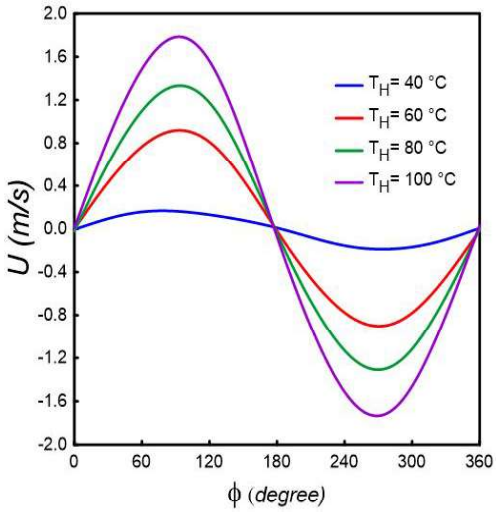

Figure 4.10: Steady state U-acoustic velocity vs. phase angle ψ at the mid-core ($X = \frac{X_F + X_S}{2}$ and $Y = \frac{H}{2}$)for Re=100, Pr=0.67 and ε=0.6

Figure 4.10 outlines the effect of thermal gradient on the steady state U -acoustic velocity through a period for T_C= 20 °C, ε = 0.6, Re = 100 and Pr = 0.67. It can be observed that the compression expansion of the acoustic velocity is larger by increasing T_H. Note that even when the exchangers provide a small temperature gradient, the acoustic standing wave exhibits a sinusoidal shape due to negligible non-harmonic interaction which serves to provide small resonant oscillations slowly propagating over time. Thereby, the acoustic propagation exhibits a small phase delay (of about 5 degrees between each successive input) not visible to the naked eye.

4.6.3 Convection effect on Rayleigh's streaming

In Figure 4.11, isotherms and streamlines through stainless steel core (Figure 4.11(a)-(b) and the $CaCO_3$ porous core (Figs. 11(c)-(d)) are depicted (from left to right) to unveil the flow direction in the system for $Re = 100$, $Pr = 0.67$, ε=0.6, T_H =100 °C and T_C =20 °C. As expected, the temperature at the SWTAE core and its close vicinity may be observed to be high. The heat flow through this porous core is obviously laminar since isotherms through the stainless steel core avoid the great effect of Rayleigh streaming. The buoyancy effect controls the heat flux in regions where the inertia dominates.Thermo-viscous dissipation combined with natural convection helps to give rise to vortex shedding near the hot end. Furthermore, the hot flow intensely penetrates the cold side thereby distressing the fluid expansion due to a faster decrease in the heat gradient between the boundaries of the core.

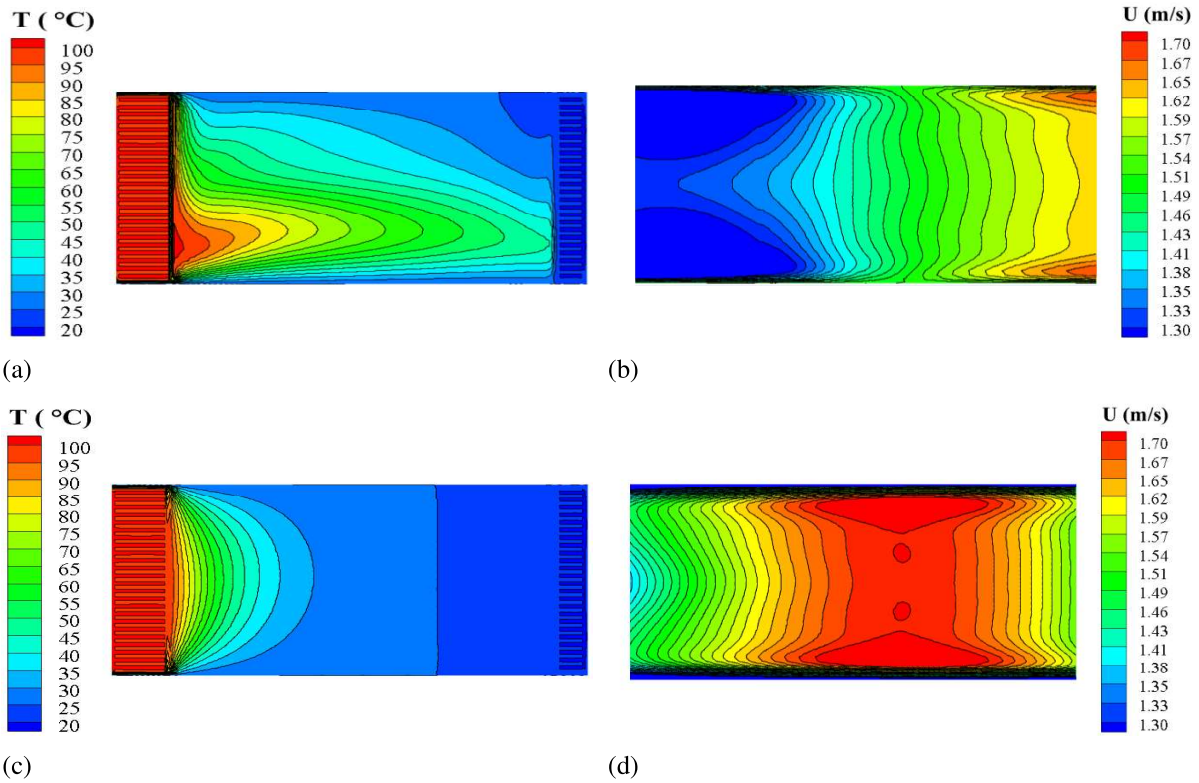

Figure 4.11: Isotherms and streamlines in the SWTAE core at the steady state for Re=100, Pr=0.67, ε=0.6, T_H =100 °C and T_C =20 °C with (a, b) stainless steel; (c, d)$CaCO_3$ porous material

For a conductive and better absorbent material, the buoyancy effect controls the heat flux where inertia dominates, inducing an important flow near the lower wall (case of stainless steel; Figure 4.11a), while Figure 11c highlights the symmetrical aspect of the isotherms via the thermophysical properties of $CaCO_3$ (thermal conductivity and heat capacity) compared to stainless steel. It can also be noted that the $CaCO_3$'s use ensures a laminar convective flow with high velocities in the resonator while damping the undesirable perturbations in the porous core. Figure 4.12 presents the upright evolution of the temperature close to the HE ($X = X_S + 2\delta X; \delta X = 10^{-3}m$) for ε = 0.6 and two values of T_H , viz. 40 °C and 100 °C. At this porosity, the temperature profile is not or almost not influenced by the buoyancy effect, even at a low thermal gradient (Figure 4.12a) where a slight rise in temperature is observed in the hot zone near the low side. Besides, at T_H= 100 °C (Figure 4.12b), the temperature sets out a parabolic and symmetrical profile.

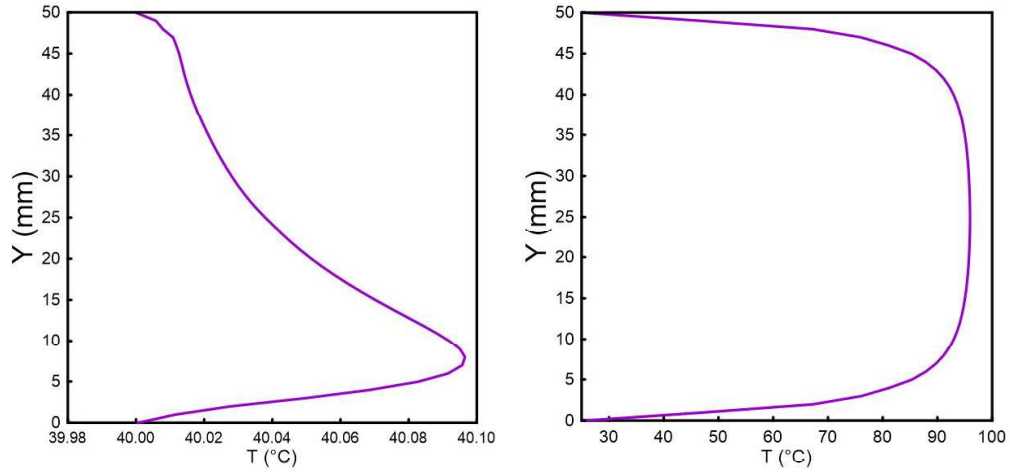

(a) (b)

Figure 4.12: Upright evolvement of temperature close-up the hot exchanger ($X = X_S + 2\delta X$; ($\delta X = 10^{-3}$ m) for ε=0.6 and with (a) T_H=40 °C (b) T_H=100 °C

Figure 4.13 displays the acoustic U -velocity vs. the upright coordinate Y at the west side of the TAC set by the phase ψ for different hot temperature over a cycle. Acoustic oscillation is typically asymmetric where the amplitude ratio decreases with the non-harmonic interaction mitigation at high T_H. The Richardson effect is clearly discerned for most phases and large velocity overshoots are induced by the viscous force near outer walls. Besides, counter-rotating convection seems to be the main factor in the appearance of vortices, reflecting the importance of the non-linear effect at the core edges.

4.6.4 Heat transfer analysis within the SWTAE

Figure 4.14 portrays the temperature along the SWTAE at $Y = H/2$ for ε=0.6and $Re = 100$ set by the HE temperature (T_H). All the profiles are almost similar exhibiting respectively a maximum and a minimum near the HE and CE except at low temperature T_H (=40 °C). The temperature at the hot buffer (HB) and at the resonator (except at the outlet) remains constant (in this case a plateau) due to the transfer of heat between the HE and external walls (no wall at the outlet). Note that at this low temperature of 40 °C , the plateau remains from the buffer to the left vicinity of the CE indicating the absence of a maximum. Obviously, the HE and the TAC's left side ($0.2 \leq X \leq 0.3$) supply heat to the fluid, while the TAC and CE's right sides, as well as the left side of the resonator ($X_F = 0.42$) extract heat from the fluid.

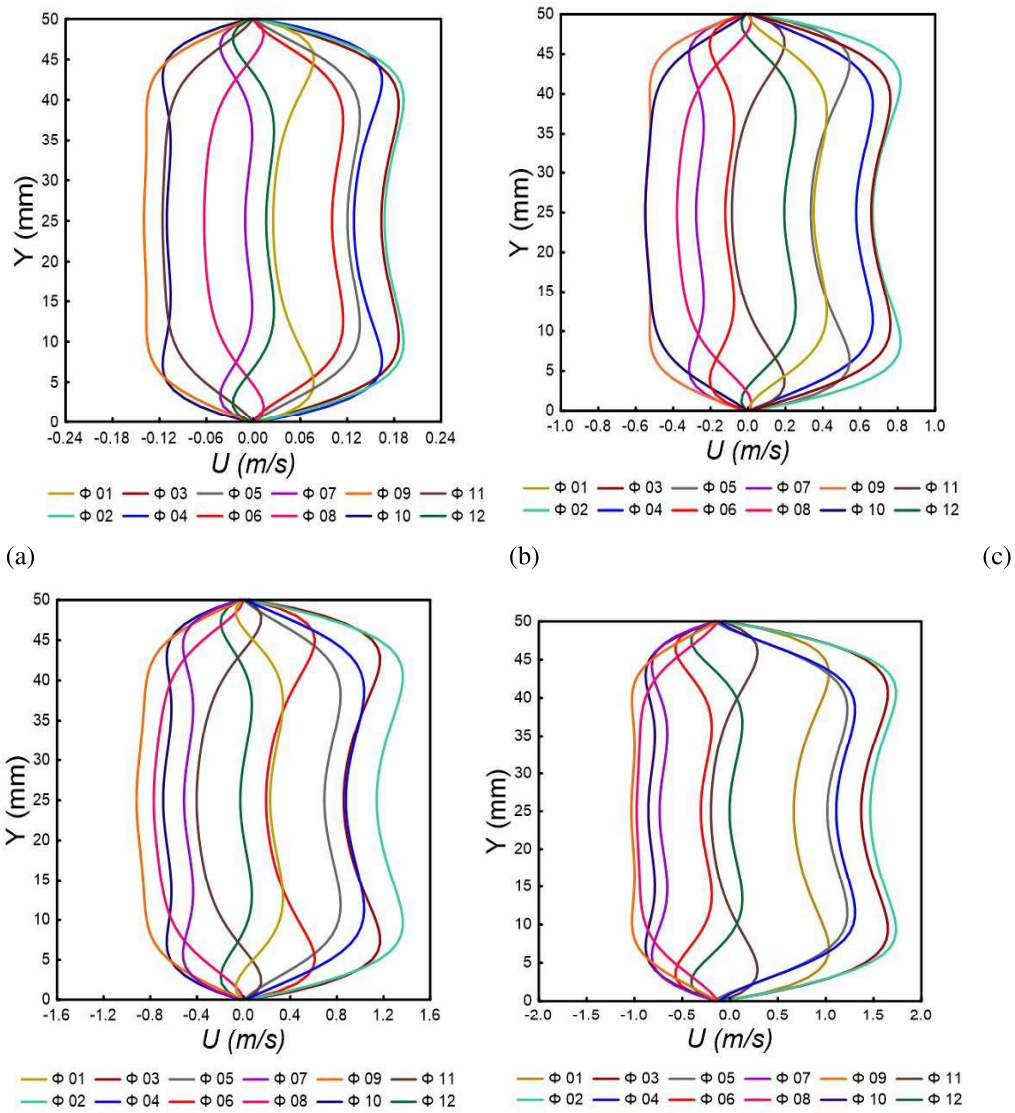

Figure 4.13: Streamwise acoustic velocity evolution vs. the upright direction close-up the hot exchanger ($X = X_F - 2\delta X$; (δX =1 mm)) set by phase ψ for Re=100, Pr=0.67 and ε=0.6 with (a) T_H=40 °C (b) T_H=60 °C (c) T_H=80 °C (d) T_H=100 °C

This in accordance with the result of Figure 4.11. Specifically, compression and expansion become minor, providing insignificant thermoacoustic conversion. Further, the temperature near the open outlet end is strongly elevated due to heat build-up coupled with low acoustic vibrations which induce large viscous forces. At higher thermal gradient between the core limits, the end effect is still important. For T_H =100 °C , the temperature increases from the ambient value (25 °C) at the resonator tube up to 40 °C at the outlet.

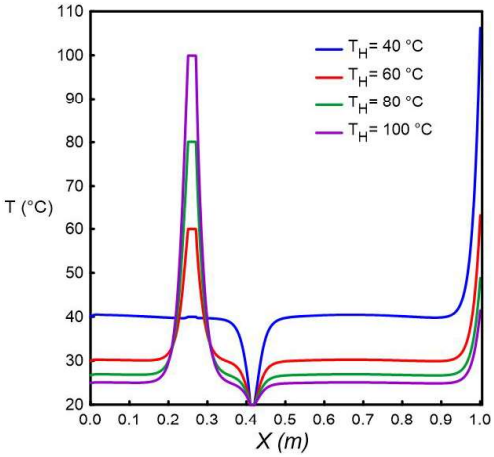

Figure 4.14: Streamwise temperature evolution a $Y = \frac{H}{2}$ for ε =0.6, Re =100 at different T_H values.

4.6.5 Thermal-acoustic efficiency

Figure 4.15 depicts the thermal efficiency η vs. the temperature gradient (Δ T) set by different porosities medium ranging from 0.4 to 0.7 for $Re = 100$ and $Pr = 0.67$. Overall, it can be seen that a high heating temperature leads to an efficiency rise. In addition, the greater the porosity, the better the efficiency demonstrating that the porosity has a propitious influence on thermal efficiency, in particular at high difference temperature. For a high porosity (0.6 and 0.7), the thermal efficiency increases continuously, displays a slight plateau for further increasing at large Δ T. This is due to the contact surface decreasing between solid walls and the working fluid mitigating the thermal instability effect while ensuring an effective compression expansion of the fluid.

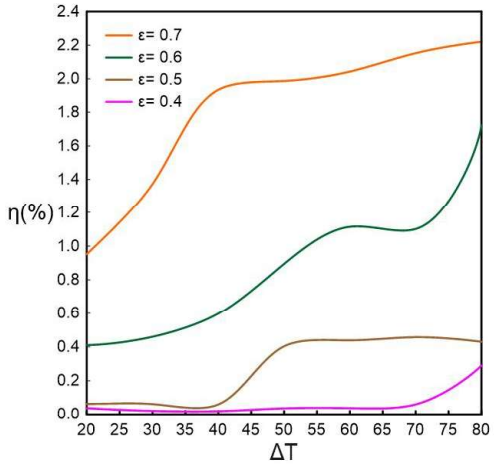

Figure 4.15: Thermal efficiency η (%) vs ΔT set by the core porosity at Re=100 and Pr=0.67

4.7 Conclusion

This paper numerically investigated Rayleigh streaming and heat transfer in a standing-wave thermoacoustic engine via a lattice Boltzmann method on D2Q9 lattice. To handle streaming flow and heat transfer, a TLBM with dual density functions' approach has been applied to solve the extended Brinkman-Forchheimer Darcy equations as a mathematical model depicting the targeted problem. Beforehand, a grid independence check was performed to better secure the present solution independency. This work mainly endeavored to explore the effects of relevant parameters such as temperature difference around thermoacoustic core and porosity on the SWTAE thermal efficiency. Besides, the dynamic and thermal fields were investigated inside the TAC. The spatial distributions of velocity and temperature in the streamwise and transverse directions and the temporal history were exhibited. As a result, all the stages leading to the steady state for different thermal gradients have been highlighted. Through this investigation, it appeared that a small difference temperature slightly inhibits the appearance of oscillations. Within the range of our computations, the main outcomes of the present study can be pointed up as follows:

- The temperature difference imposed on the TAC limits and the porosity are key parameters that have a major impact, especially on performance;
- Optimal thermal performance is picked up at large porosities regardless of the imposed gradient temperature.
- At a fixed cooling temperature and at a heating temperature in the range 40-100 °C, the efficiency generally increases at high porosity.
- The velocity and temperature oscillations in the TAC have been affirmed;
- Porous $CaCO_3$ media could be used as an inner core due to its longer life and low cost construction;
- The TLBM simulations performed characterized the operating mechanism of a SWTAE;
- Numerical simulations report properly the flow behavior in a SWTAE including a porous medium thereby demonstrating that the present DDF-based TLBM herein deemed can now be applied to deal with such problems.

Bibliography

[1] Tao Jin, Rui Yang, Yi Wang, Yuanliang Liu, and Ye Feng. Phase adjustment analysis and performance of a looped thermoacoustic prime mover with compliance/resistance tube. *Applied Energy*, 183:290–298, 2016.

[2] Jingyuan Xu, Jianying Hu, Ercang Luo, Limin Zhang, and Wei Dai. A cascade-looped thermoacoustic driven cryocooler with different-diameter resonance tubes. part i: Theoretical analysis of thermodynamic performance and characteristics. *Energy*, 181:943–953, 2019.

[3] Jingyuan Xu, Jianying Hu, Yanlei Sun, Huizhi Wang, Zhanghua Wu, Jiangfeng Hu, Simone Hochgreb, and Ercang Luo. A cascade-looped thermoacoustic driven cryocooler with different-diameter resonance tubes. part : Experimental study and comparison. *Energy*, 207:118232, 2020.

[4] Jingqi Tan, Jianjian Wei, and Tao Jin. Electrical-analogy network model of a modified two-phase thermofluidic oscillator with regenerator for low-grade heat recovery. *Applied Energy*, 262:114539, 2020.

[5] Jingyuan Xu, Ercang Luo, and Simone Hochgreb. Study on a heat-driven thermoacoustic refrigerator for low-grade heat recovery. *Applied Energy*, 271:115167, 2020.

[6] Chao Shen, Yaling He, Yuguang Li, Hanbing Ke, Dongwei Zhang, and Yingwen Liu. Performance of solar powered thermoacoustic engine at different tilted angles. *Applied Thermal Engineering*, 29(13):2745–2756, 2009.

[7] Dan Zhao, Shihuai Li, Wenming Yang, and Zhiguo Zhang. Numerical investigation of the effect of distributed heat sources on heat-to-sound conversion in a t-shaped thermoacoustic system. *Applied Energy*, 144:204–213, 2015.

[8] A Kruse, A Ruziewicz, A Nemś, and M Tajmar. Numerical analysis of competing methods for acoustic field adjustment in a looped-tube thermoacoustic engine with a single stage. *Energy conversion and management*, 181:26–35, 2019.

[9] S Zhang, ZH Wu, RD Zhao, GY Yu, W Dai, and EC Luo. Study on a basic unit of a double-acting thermoacoustic heat engine used for dish solar power. *Energy conversion and management*, 85:718–726, 2014.

[10] Kenichiro Tsuda and Yuki Ueda. Critical temperature of traveling-and standing-wave thermoacoustic engines using a wet regenerator. *Applied Energy*, 196:62–67, 2017.

[11] K Tang, T Lei, T Jin, XG Lin, and ZZ Xu. A standing-wave thermoacoustic engine with gas-liquid coupling oscillation. *Applied Physics Letters*, 94(25):254101, 2009.

[12] Richard Raspet, William V Slaton, Craig J Hickey, and Robert A Hiller. Theory of inert gas-condensing vapor thermoacoustics: Propagation equation. *The Journal of the Acoustical Society of America*, 112(4):1414–1422, 2002.

[13] K Tang, ZJ Huang, T Jin, and GB Chen. Influence of acoustic pressure amplifier dimensions on the performance of a standing-wave thermoacoustic system. *Applied thermal engineering*, 29(5-6):950–956, 2009.

[14] Rui Bao, Guobang Chen, Ke Tang, Zhengzhong Jia, and Weihua Cao. Influence of resonance tube geometry shape on performance of thermoacoustic engine. *Ultrasonics*, 44:e1519–e1521, 2006.

[15] Rui Yang, Yi Wang, Tao Jin, Ye Feng, and Ke Tang. Performance optimization of the regenerator of a looped thermoacoustic engine powered by low-grade heat. *International Journal of Energy Research*, 42(14):4470–4480, 2018.

[16] Kenta Nakamura and Yuki Ueda. Design and construction of a standing-wave thermoacoustic engine with heat sources having a given temperature ratio. *Journal of Thermal Science and Technology*, 6(3):416–423, 2011.

[17] Geng Chen, Lihua Tang, and Brian R Mace. Theoretical and experimental investigation of the dynamic behaviour of a standing-wave thermoacoustic engine with various boundary conditions. *International Journal of Heat and Mass Transfer*, 123:367–381, 2018.

[18] MEH Tijani and S Spoelstra. A high performance thermoacoustic engine. *Journal of Applied Physics*, 110(9):093519, 2011.

[19] Islam A Ramadan, Hélène Bailliet, and Jean-Christophe Valière. Experimental investigation of the influence of natural convection and end-effects on rayleigh streaming in a thermoacoustic engine. *The Journal of the Acoustical Society of America*, 143(1):361–372, 2018.

[20] S Jung and KI Matveev. Study of a small-scale standing-wave thermoacoustic engine. *Proceedings of the Institution of Mechanical Engineers, Part C: Journal of Mechanical Engineering Science*, 224(1):133–141, 2010.

[21] Esmatullah Maiwand Sharify and Shinya Hasegawa. Traveling-wave thermoacoustic refrigerator driven by a multistage traveling-wave thermoacoustic engine. *Applied Thermal Engineering*, 113:791–795, 2017.

[22] Moulay El Hassan Tijani. *Loudspeaker-driven thermo-acoustic refrigeration*. Technische Universiteit Eindhoven Eindhoven, 2001.

[23] Syeda Humaira Tasnim and Roydon Andrew Fraser. Modeling and analysis of flow, thermal, and energy fields within stacks of thermoacoustic engines filled with porous media: a conjugate problem. *Journal of Thermal Science and Engineering Applications*, 1(4), 2009.

[24] Sergey Karpov and Andrea Prosperetti. A nonlinear model of thermoacoustic devices. *The Journal of the Acoustical Society of America*, 112(4):1431–1444, 2002.

[25] Mark F Hamilton, Yurii A Ilinskii, and Evgenia A Zabolotskaya. Nonlinear two-dimensional model for thermoacoustic engines. *The Journal of the Acoustical Society of America*, 111(5):2076–2086, 2002.

[26] DM Sun, K Wang, LM Qiu, BH Lai, YF Li, and XB Zhang. Theoretical and experimental investigation of onset characteristics of standing-wave thermoacoustic engines based on thermodynamic analysis. *Applied acoustics*, 81:50–57, 2014.

[27] Guillaume Penelet, Matthieu Guedra, Vitalyi Gusev, and Thibaut Devaux. Simplified account of rayleigh streaming for the description of nonlinear processes leading to steady

state sound in thermoacoustic engines. *International journal of heat and mass transfer*, 55(21-22):6042–6053, 2012.

[28] Guoyao Yu, Wei Dai, and Ercang Luo. Cfd simulation of a 300 hz thermoacoustic standing wave engine. *Cryogenics*, 50(9):615–622, 2010.

[29] Omar Hireche, Catherine Weisman, Diana Baltean-Carlès, Virginie Daru, and Yann Fraigneau. Numerical study of the effects of natural convection in a thermoacoustic configuration-natural convection in thermoacoustics. *Mechanics & Industry*, 20(8):807, 2019.

[30] Virginie Daru, Ida Reyt, Hélène Bailliet, Catherine Weisman, and Diana Baltean-Carles. Acoustic and streaming velocity components in a resonant waveguide at high acoustic levels. *The Journal of the Acoustical Society of America*, 141(1):563–574, 2017.

[31] Virginie Daru, Diana Baltean-Carlès, Catherine Weisman, Hélène Bailliet, and Ida Reyt. Acoustic rayleigh streaming: Comprehensive analysis of source terms and their evolution with acoustic level. *The Journal of the Acoustical Society of America*, 142(4):2608–2608, 2017.

[32] R Rahpeima and R Ebrahimi. Numerical investigation of the effect of stack geometrical parameters and thermo-physical properties on performance of a standing wave thermoacoustic refrigerator. *Applied Thermal Engineering*, 149:1203–1214, 2019.

[33] Kai Wang, DM Sun, J Zhang, J Zou, K Wu, LM Qiu, and ZY Huang. Numerical simulation on onset characteristics of traveling-wave thermoacoustic engines based on a time-domain network model. *International Journal of Thermal Sciences*, 94:61–71, 2015.

[34] Yong Wang, Yaling He, Jing Huang, and Qing Li. Implicit–explicit finite-difference lattice boltzmann method with viscid compressible model for gas oscillating patterns in a resonator. *International journal for numerical methods in fluids*, 59(8):853–872, 2009.

[35] Yong Wang, Dong-Ke Sun, Ya-Ling He, and Wen-Quan Tao. Lattice boltzmann study on thermoacoustic onset in a rijke tube. *The European Physical Journal Plus*, 130(1):1–10, 2015.

[36] Feng Shan, Xiasheng Guo, Juan Tu, Jianchun Cheng, and Dong Zhang. Multi-relaxation-time lattice boltzmann modeling of the acoustic field generated by focused transducer. *International Journal of Modern Physics C*, 28(03):1750038, 2017.

[37] Yong Wang, YL He, Qing Li, and GH Tang. Numerical simulations of gas resonant oscillations in a closed tube using lattice boltzmann method. *International journal of heat and mass transfer*, 51(11-12):3082–3090, 2008.

[38] Chenzhen Ji and Dan Zhao. Lattice boltzmann investigation of acoustic damping mechanism and performance of an in-duct circular orifice. *The Journal of the Acoustical Society of America*, 135(6):3243–3251, 2014.

[39] Erik M Salomons, Walter JA Lohman, and Han Zhou. Simulation of sound waves using the lattice boltzmann method for fluid flow: Benchmark cases for outdoor sound propagation. *PloS one*, 11(1):e0147206, 2016.

[40] Arganthaël Berson, Marc Michard, and Philippe Blanc-Benon. Measurement of acoustic velocity in the stack of a thermoacoustic refrigerator using particle image velocimetry. *Heat and Mass Transfer*, 44(8):1015–1023, 2008.

[41] Rui Yang, Yi Wang, Jingqi Tan, Jiaqi Luo, and Tao Jin. Numerical and experimental study of a looped travelling-wave thermoacoustic electric generator for low-grade heat recovery. *International Journal of Energy Research*, 43(11):5735–5746, 2019.

[42] Oumayma Miled, Hacen Dhahri, and Abdallah Mhimid. Numerical investigation of porous stack for a solar-powered thermoacoustic refrigerator. *Advances in Mechanical Engineering*, 12(6):1687814020930843, 2020.

[43] Tetsushi Biwa, Yusuke Tashiro, Masahiro Ishigaki, Yuki Ueda, and Taichi Yazaki. Measurements of acoustic streaming in a looped-tube thermoacoustic engine with a jet pump. *Journal of applied physics*, 101(6):064914, 2007.

[44] Zhaoli Guo and TS Zhao. Lattice boltzmann model for incompressible flows through porous media. *Physical review E*, 66(3):036304, 2002.

[45] Bayssain Amami, Hacen Dhahri, and Abdallah Mhimid. Viscous dissipation effects on heat transfer, energy storage, and entropy generation for fluid flow in a porous channel submitted to a uniform magnetic field. *Journal of Porous Media*, 17(10), 2014.

[46] Qing Liu and Ya-Ling He. Lattice boltzmann simulations of convection heat transfer in porous media. *Physica A: Statistical Mechanics and its Applications*, 465:742–753, 2017.

[47] Jinku Wang, Moran Wang, and Zhixin Li. A lattice boltzmann algorithm for fluid–solid conjugate heat transfer. *International journal of thermal sciences*, 46(3):228–234, 2007.

[48] Mahmoud Jourabian, A Ali Rabienataj Darzi, Davood Toghraie, and Omid ali Akbari. Melting process in porous media around two hot cylinders: Numerical study using the lattice boltzmann method. *Physica A: Statistical Mechanics and its Applications*, 509:316–335, 2018.

[49] Dongyan Gao and Zhenqian Chen. Lattice boltzmann simulation of natural convection dominated melting in a rectangular cavity filled with porous media. *International Journal of Thermal Sciences*, 50(4):493–501, 2011.

[50] GH Tang, WQ Tao, and YL He. Lattice boltzmann method for simulating gas flow in microchannels. *International journal of modern physics C*, 15(02):335–347, 2004.

[51] Ehsan Kamali Ahangar, Mohammad Bagher Ayani, and Javad Abolfazli Esfahani. Simulation of rarefied gas flow in a microchannel with backward facing step by two relaxation times using lattice boltzmann method–slip and transient flow regimes. *International Journal of Mechanical Sciences*, 157:802–815, 2019.

[52] H Shokouhmand, F Jam, and MR Salimpour. Simulation of laminar flow and convective heat transfer in conduits filled with porous media using lattice boltzmann method. *International Communications in Heat and Mass Transfer*, 36(4):378–384, 2009.

[53] Kazuto Kuzuu and Shinya Hasegawa. Effect of non-linear flow behavior on heat transfer in a thermoacoustic engine core. *International Journal of Heat and Mass Transfer*, 108:1591–1601, 2017.

Chapter 5

Conclusion

The main aim of this thesis is to optimize the operating mode and the efficiency of a standing wave thermoacoustic engine by the limitation of thermoacoustic instabilities occurred within the core. The operating efficiency of a thermoacoustic engine can be seriously damaged by due to the existence of nonlinear effects such as minor losses, acoustic and Rayleigh streaming. Thermal lattice Boltzmann method is adopted to investigate the flow of the working fluid and the heat transfer within a standing wave thermoacoustic engine (SWTAE). A two-dimensional standing wave device is patterned based on the Darcy–Brinkmann–Forchheimer model. The system is composed of a straight resonator tube filled in part with a porous core subject of a temperature difference. In the first chapter, an overview of the thermoacoustic field is given. A brief history about the discovery and the critical development of the thermoacoustic field is detailed. The thermoacoustic devices configurations and applications are presented followed by a description of the conversion principle within the various thermoacoustic devices. Finally, a bibliographical synthesis about the general structure and main particularities of standing wave thermoacoustic devices is detailed.

The second chapter depicts the numerical model used for the simulation of the fluid flow and heat transfer within a standing wave thermoacoustic engine. The kinetic theory of the fluid dynamic is examined for the discretization of the lattice Boltzmann method. Then, the extended lattice Boltzmann model for the simulation of complex area as the thermoacoustic porous core is detailed. The appropriate boundary conditions at the various walls of the engine and core limits are developed.

The third chapter of this thesis aims in providing a full investigation about the optimum thermoacoustic core specifications such optimum position and length for better acoustic production. A parametric study were carried out for the minimization of irreversible process within the porous core and at the external walls of the resonator tube. Results found indicates that the acoustic work is strongly linked to the porous core matrix structure. The acoustic velocity is reduced by the minimization of the core permeability where improved frictions are occurred. Accordingly, an important entropy generation is observed caused by the appearing of a vital unstable fluid fluctuation. Maximum entropy generation is observed at the cold region of the core where important heat losses are occurred. It is mainly dependent on the temperature gradient at

the external walls and the TAC boundaries and dominated by viscous frictions irreversibilities at the porous medium. Following up, in the fourth chapter, lattice Boltzmann method is adopted to examine the working mode of a SWTAE and analyze undesirable effects of the natural convection on the heat transfer and acoustic conversion within the porous core. Operating under low-grade heat conditions and for different porous core parameters, the thermodynamic flow behavior and heat transfer within the different components of the engine were investigated. The performance of celcor ($CaCO_3$) shell matrix as thermoacoustic core was principally analysed via thermal lattice Boltzmann method. Such method present a simple way to investigate the working fluid compression-expansion process experienced at low Mach number. The influence of undesirable effects on the heat transfer and engine performance is well investigate demonstrating simultaneously the profitability of shell material as TAC constructive material than actual uses ones. In effect, the performance of $CaCO_3$ material as good thermal-to-acoustic converter is proved due to its low conductivity serving in minimizing the undesirable effects such as end-effect and Rayleigh streaming. It serves in reducing visco-thermal fluctuations and lead to diminish the linear losses.

As a conclusion, the engine operate at conditions closer to them of a reversible device for:

- Lower porous medium permeability leads to minimize the acoustic dissipation by reducing the friction losses and heat transfer nonlinearities;
- Minor heat transfer instabilities are obtained for a $CaCO_3$ porous material. Such material utilization leads to the minimization of heat transfer instabilities and serves in the suppression of the effects of natural convection in Rayleigh streaming and end effects;
- The entropy generation through the thermoacoustic system is mainly influenced by the temperature gradient at the external walls and the TAC boundaries and it is dominated by viscous frictions irreversibilities at the porous medium. In essence, maximum irreversibilities are observed at the cold region where important heat losses are occurred;
- The standing wave thermoacoustic engine can be successfully employed for low grade heat recovery. The $CaCO_3$ material show good performance in converting the heat field to acoustic power and on the suppressing of the nonlinear effects;

Further improves are suggested for future work in the objective to optimize the efficiency and life time of standing wave thermoacoustic devices:

- The performance of employment of environment-friendly magnetic fields deserve to be further investigate,
- Our studies must be certainly completed by experimentation,
- To give better understanding of the thermoacoustic phenomena within the SWTAE, it is projected to extend our present SRT-TLBM model to the compressible Multi-Relaxation method (MRT-LBM),